ACOUSTIC EMISSIONS AND VARIATION OF AC-CONDUCTIVITY IN POROUS SANDSTONE SAMPLES SUBJECTED TO UNIAXIAL LOADING

by

Theodora Koumoudeli

B.Sc., Technological Education Institute of Crete, 2017

Thesis Submitted in Partial Fulfilment of the Requirements for the Degree of Master of Science

in the Department of
Environmental and Natural Resources Engineering

Faculty of Applied Science

TEI OF CRETE

Autumn 2017

Thesis Examination Committee

Dr Vassilios Saltas (supervisor)
Associate Professor, TEI of Crete

Dr Filippos Vallianatos
Professor, TEI of Crete

Dr Zacharias Agioutantis
Professor, University of Kentucky

Acknowledgements

First, I would like to thank my thesis advisor Associate Professor Vassilis Saltas for his excellent support, guidance and encouragement throughout my Master Thesis. The present thesis was conducted in the Laboratory of Geophysics and Seismology (GSL) of the Department of Environmental and Natural Resources Engineering, at the Technological Educational Institute of Crete.

I would also like to thank the Director of the GSL, Professor Filippos Vallianatos who gave me the opportunity to participate in laboratory experiments in the field of rock physics. My thanks are extended to the third member of the Advisory Committee, Professor Zacharias Agioutantis (Department of Mining Engineering, University of Kentucky) for his valuable comments that improved the final version of the thesis.

I would like to thank Dr. Ioannis Fitilis for his support and for providing me essential information for the analysis software of acoustic emissions.

Finally, thanks to my fiancé, Nikos Ligopsihakis, and my parents who without their support I could never completed this Thesis. I would like also to thank my postgraduate classmates in master of Geo-environmental Resources and Risks for the beautiful moments and their support.

Abstract

In the present work, electrical ac-conductivity measurements were carried out simultaneously with AE monitoring in dry and water-saturated sandstone specimens subjected to different types of uniaxial compressive stress, up to ultimate failure. The high porosity of the specimens allows the investigation of the influence of the water concentration to the changes of the electrical conductivity and to the AE activity during compression. A strong correlation of ac-conductivity with AE activity is observed during linear and stepped uniaxial loading, due to the charge transfer caused by micro-cracks generation and propagation in the sandstone. The concentration of the pore fluid (water) determines the sign and the value of the variation of the electrical ac-conductivity.

A strong correlation of the ac-conductivity with the AE activity is observed during different types (linear, stepped, saw-tooth) of uniaxial compression in sandstone specimens of high porosity. These observations are of great importance in investigating precursory phenomena in the meso- and macro-scale, such as the mechanical failure of materials and the occurrence of pre-seismic electric signals.

There is an additional aspect of the changes in the measured ac-conductivity which is related to the different water content of sandstone specimens. The application of the external pressure to the sandstone specimen leads to micro-cracks where the excess of water is passed through and form new conduction paths. The variation of ac-conductivity is either positive or negative depending on the water content. Additionally, a low AE activity is observed in water-saturated specimens since the water acts as a lubricant in the newly formed cracks during the applied load.

Keywords: Acoustic emissions; Sandstone; Porosity; Deformation; Stress-strain; Location of events; ac-conductivity; Improved b-value

Table of Contents

List of Figures

List of Tables

List of Abbreviations

NDT	=	Non-Destructive Testing
AE	=	Acoustic Emission
AET	=	Acoustic Emission Technique
HDD	=	Hit Driven Data
TDD	=	Time Driven Data
TOA	=	Time of Arrival
TD	=	Time Difference
FR	=	Felicity Ratio
PDT	=	Peak Definition Time
HDT	=	Hit Definition Time
HLT	=	Hit Lockout Time
FFT	=	Fast Fourier Transform
DWT	=	Discrete Wavelets
CWT	=	Continuous Wavelet
LVDT	=	Linear Variable Differential Transformer

Chapter 1: Introduction

1.1 General Introduction

Seismology belongs to applied science and is a part of the field of Geophysics, which describes the Earth's structure. Earthquake is a geological phenomenon, but the release of its energy and the propagation process is governed by the laws of Physics. The study of earthquakes based on observations of seismic effects directly by humans, on the other hand, the studies of seismic waves recorded by suitably sensitive instruments in seismological stations. The earthquake source can be explained as a sudden release of strain energy during the movement along a fault. The reason for the movement is the slow accumulation of strain energy due to relative movement of two sides of the fault. Faults can be very small with millimeters slipping to very large with meters slipping.

The development of faults and shear fracture systems for a variety of rock types involves the growth and the interaction of micro-cracks. Acoustic emission (AE), which is produced by rapid micro-crack growth, is associated with brittle fracture phenomenon and has provided a wealth of information regarding the failure process in rock. A variety of terms, including acoustic emission, microseismic activity and micro-earthquake activity are utilized to understand the seismic signals when solids are stressed or deformed (Hardy, 2003). In laboratory scale studies, the acoustic emission technique is successfully used to understand how micro-cracks are produced in a specimen. Acoustic emission technique is a non-destructive testing in which mechanical, electrical or electromagnetic signals are emitted by rocks or materials under pressure (Agioutantis *et al*., 2015). Except of the acoustic emissions, there are various fracto-emission phenomena such as the emission of charged particles, atoms, photons, molecules and more (Saltas *et al*., 2014). The emission of charged particles during the uniaxial loading produced in tests on water saturated rocks compared with dry give higher intensity because of the presence of water around cracks (Lavrov A., 2005).

In this thesis, time-series measurements of ac-conductivity at selected frequencies (0,01Hz, 10kHz and 200kHz) were accomplished in conjunction with acoustic emission (AE) monitoring at three different types of uniaxial compression experiments (linear, stepped and saw-tooth) of dry and water-saturated sandstone specimens of high porosity up to failure.

1.2 Objectives and Scope of the research

The main objectives of this research are to investigate the possible correlations between the AE activity and electrical ac-conductivity variations, during the mechanical loading of porous rock samples. The effect of porosity and the degree of water-saturation of the rock specimens is investigated by using sandstone specimens of high porosity.

1.3 Thesis Outline

In chapter 2 the literature review of acoustic emissions technique and its applications are presented. The fundamentals of acoustic emission technique (AET) are presented in chapter 3. Additional analysis such as porosity, ac-conductivity, deformation and properties of sandstone are referred to chapter 4. The experimental procedure and the software that was used to analyse the AE data are discussed in chapter 5. In chapter 6 the results of uniaxial compression on different sandstone specimens and the correlation of acoustic emission parameters with ac-conductivity measurements are presented. Finally, chapter 7 draws the main conclusions and recommendations for future work.

Chapter 2: Literature Review

2.1 Acoustic Emission Technique

Obert and Duvall, who worked for U.S. Bureau of Mines (USBM) have discovered the acoustic emission technique in 1937, in the framework of a research program on the study of mines' strength in Missouri and Oklahoma. During this research, sonic studies were carried out by means of two transducers, where the one acted as a mechanical signal transmitter and the other transducer acted as a receiver of this signal. After they removed the transmitter, they observed that the receiver continued to record signals from the pillar (Obert *et al.*, 1942).

In 1963, Neville Cook developed a refined testing machine to measure the strain-softening deformation in rocks. He studied the stress-strain behaviour of rocks at the University of Minnesota and he was the first who analysed the cracks influence on the effective moduli. In 1965, Neville Cook performed a series of uniaxial compression experiments on rectangular prisms of homogeneous and heterogeneous hard rocks. The purpose of those experiments was to study the cracks growth within the rock, the rock fracture, the rock heterogeneity, the micro-seismic activity and finally the stress-strain curve (Cook, 1965). At the same period (1963), Richard Goodman monitored the acoustic activity of rock specimens during cyclic compression tests and he observed that during the loading portion of a cycle no acoustic emission activity occurred until the stress level exceeded the stress in previous cycles. This behaviour is known as Kaiser Effect (Goodman, 1963) and was firstly observed by the German Joseph Kaiser in metals.

In recent years, the acoustic emission technique is used mostly for concrete structures such as concrete buildings and bridges. Colombo *et al*. (2005) studied the safety of concrete bridges using beams which were designed to have the same behaviour with the concrete bridge beams. In their study, the Relaxation Ratio was proposed which is expressed in terms of energy. The Relaxation Ratio is defined as the average energy during unloading phase divided by the average energy during the loading phase. A Relaxation Ratio value which is greater than one, indicates a serious damage, while a value less than one, indicates a healthier condition of the bridge (Colombo *et al*., 2005).

2.2 Precursory Phenomena

The technique of AE has direct application in seismology with the final aim to predict earthquakes by analysing aspects related to the pre-failure damage evolution, fault nucleation and crack growth in brittle rocks. In the last 50 years, several investigations have been carried out by the use of the AE technique to address problems related to earthquake processes. In seismology, the relation which describes a scaling between earthquake size and number, characterized by the *b*-value, is the Gutenberg-Richter law (Gutenberg and Richter, 1956):

$$\log_{10} N = a - bM \qquad (2.1)$$

where *N* is the number of events having magnitude *M* or greater and *a, b* are constants.

In 1962, Mogi determined that the same law is also valid for AE in rock samples under stress (Mogi, 1962). After his finding, a series of experiments were carried out in order to investigate precursory changes in *b*-value that could have resulted from stress change and therefore could be used to predict earthquakes. In 1968, Christopher H. Scholz concluded that the *b*-value decreases linearly with differential stress (Scholz, 1968a).

In order to detect the arrival times and amplitudes of AE elastic waves radiated by rapid cracking in solids, Byerlee and Lockner in 1977 developed a six-channel system which consisted of piezoelectric sensors. It is important to mention that the source location could be determined by that system (Byerlee and Lockner, 1977). Additionally, in experiments under uniaxial conditions a gap before the main event was observed which is treated as an analogue of the gap before an earthquake (Kusunose *et al*., 1982a; 1982b).

As it was mentioned previously, a linear correlation between the *b*-value and stress exists. In addition, the primary *b*-value depends on the size of the rock grains, i.e., a larger grain size leads to a lower *b*-value (Lei X., 2006). Furthermore, Lei (2011) performed a series of tests with Berea sandstone under triaxial compression and he observed that the drainage conditions affect the mode of deformation in porous rocks. The well-established dilatancy-hardening effect can be greatly suppressed by the flow of dilatancy-driven fluid, if there are permeable channels connecting the dilatancy region with the fluid sources. Fast diffusion of pore pressure leads to a significant reduction in rock strength and stabilization

of the dynamic rupture process. Good drainage conditions have the potential to enlarge the nucleation dimension and extend nucleation duration (Lei X. *et al*., 2011).

2.3 Conductivity variation during mechanical loading

Freund *et al*. (2004) carried out extensive experimental work in order to investigate the physical mechanisms that are responsible for the emission of electrical signals prior to the generation of a seismic event. They determined that the electrical conductivity of various igneous rocks (quartz-bearing granite and quartz-free anorthosite) changes upon mechanical stress (refer to Fig. 2.1) and they proposed that the responsible charge carriers are positive holes, i.e. defect electrons on the oxygen anion sub-lattice.

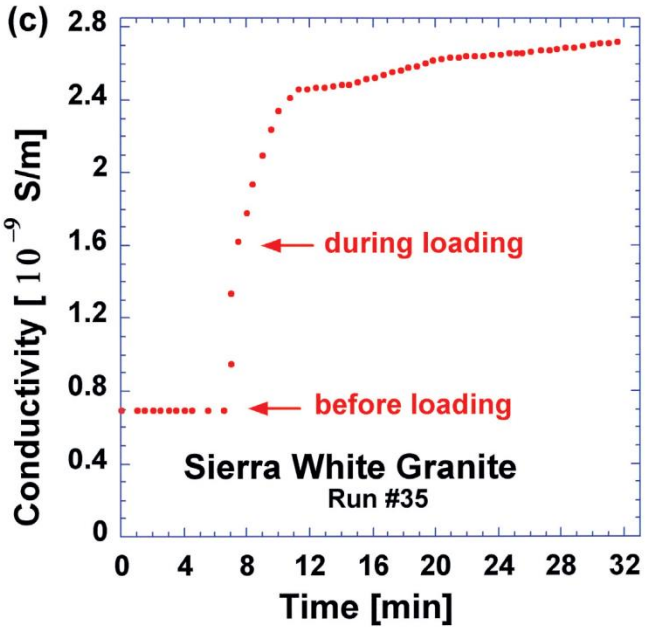

Figure 2.1: Conductivity variation during the mechanical loading of Sierra white granite (from Freund et al., 2004).

Complex ac-conductivity measurements have been carried out by Stavrakas *et al.* (2012) in marble specimens, in order to study the influence of mechanical stress on the electric-dielectric properties of this kind of geomaterials. In their laboratory experiments, dry and water-saturated marble specimens were subjected to progressive uniaxial loading up to failure and afterwards, conductivity measurements were carried out in relaxed specimens as a function of frequency. The increase in conductivity was attributed to the water inside the newly generated micro-cracks formed due to the applied load.

Complex impedance measurements in conjunction with AE monitoring have been carried out by Saltas *et al*. (2014) in dry limestone specimens, subjected to uniaxial compressive stress. Specifically, they measured the electrical properties over a wide frequency range (10^{-2} Hz – 1 MHz) as a function of the applied stress, in order to investigate the contributions of grains interior and grain boundaries to the overall measured electrical conductivity. A strong correlation of ac-conductivity and the cumulative number of events has been found, as it is demonstrated in Fig. 2.2.

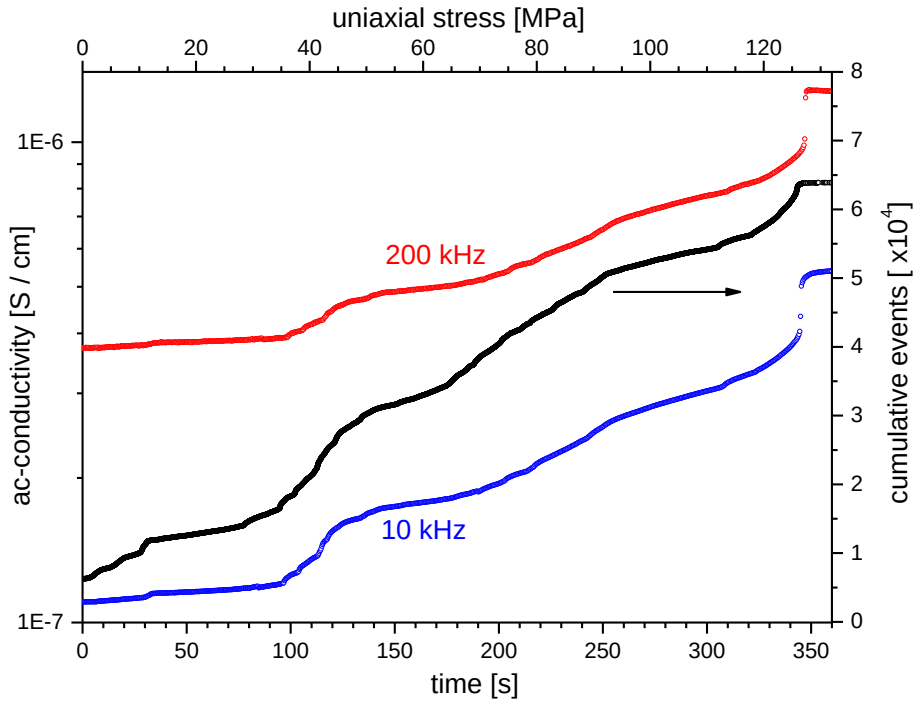

Figure 2.2: Correlation of ac-conductivity at different frequencies (10 kHz, 200 kHz) and cumulative number of events during the uniaxial loading of a dry limestone specimen (modified from Saltas et al., 2014).

Recently, Qi and Feng (2017) conducted electrical resistivity and AE measurements in cemented coal gangue backfill (CGB) specimens during their uniaxial loading, at different curing times. Some representative results are shown in Fig. 2.3. In their study, they determined quadratic relationships between the applied stress and the measured electrical resistivity at different stages of the curing procedure.

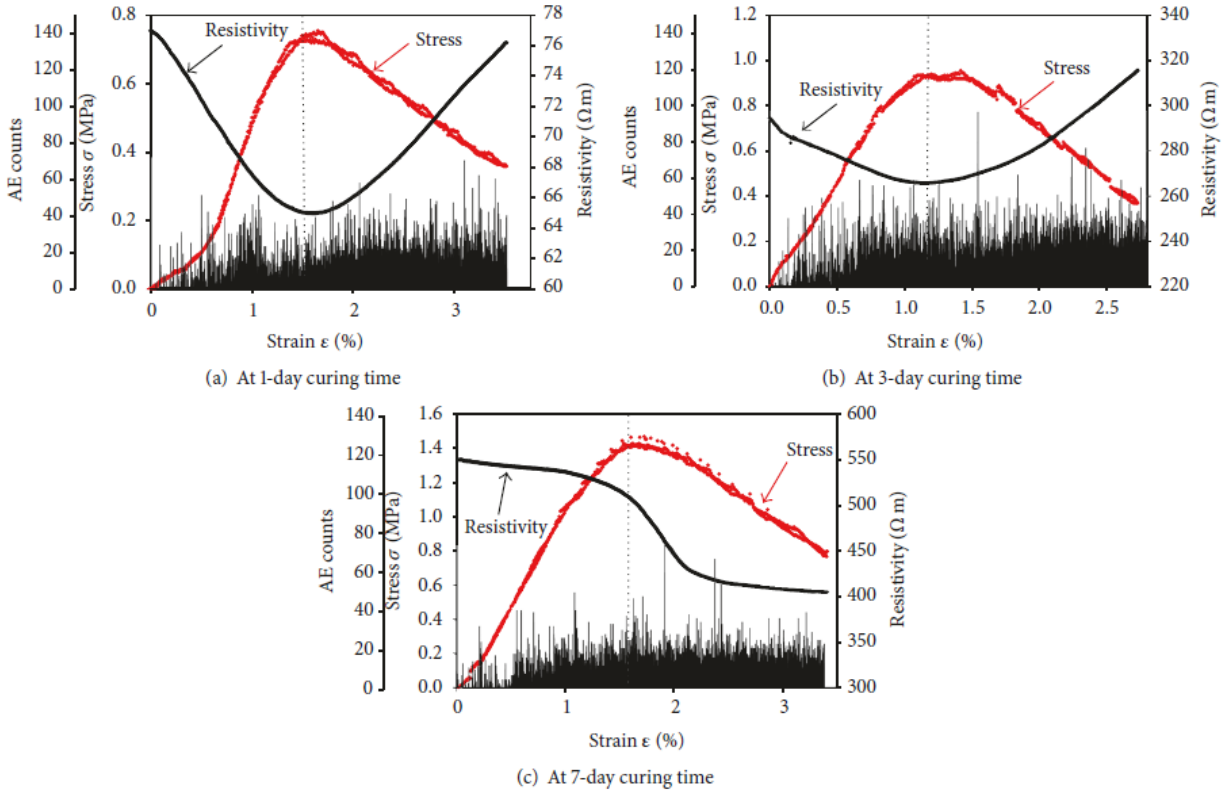

Figure 2.3: Correlation graphs of AE activity, resistivity and stress-strain, during the uniaxial loading experiments in CGB specimens at different curing times (from Qi and Feng, 2017).

Chapter 3: Principles of Acoustic Emissions

3.1 Introduction

In this chapter, we will discuss the Acoustic Emission Technique (AET) which is one of the most widespread non-destructive testing techniques in the industry. According to ASTM (American Society for Testing and Materials), Acoustic Emission is defined as "*the class of phenomena whereby transient elastic waves are generated by the rapid release of energy from localized sources within a material*". The source of these elastic waves may originate from dislocations, movements between the material grains, initiation and propagation of micro-cracking into the material during mechanical stress, or phase change due to thermal stress (Hardy, 2003).

The main objective of this work is the application of acoustic emission technique during the mechanical loading (linear, stepped and saw-tooth) of porous rocks until their final fracture, in order to investigate the evolution of the AE parameters and their correlation with the loading parameters and the simultaneous recordings of ac-conductivity.

3.2 Acoustic Emissions (AE) and Applications

As mentioned in the introduction, the Acoustic Emission Technique (AET) is based on a mechanical stimulus which acts on a material. The applied stress causes a local plastic deformation i.e., micro-cracks on specific points of the material. These micro-cracks create the AE, i.e., an elastic wave that travels away from the initial position and moves through the body, until it reaches the sensor that is mounted on the surface of the solid material. Figure 3.1 illustrates the basic parts of AET which are the AE instrument, the sensors, the specimen subjected to loading and the testing machine. Forces are exerted to the specimen from the testing machine, resulting to creation of localized sources that produce transient elastic waves recorded by the sensors. These waves are classified as transient since there is an origination which is the point source and a termination which is the boundary of the specimen surface. Sensors convert the elastic waves into electrical signals which are transferred to the AE instrument.

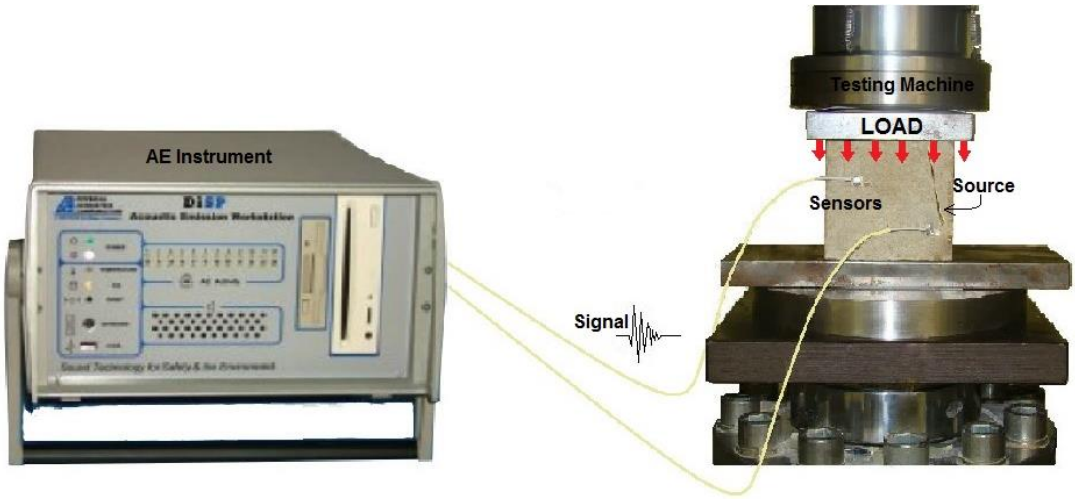

Figure 3.1: Overview of Acoustic Emission Technology

The applications of AET are useful both in engineering applications, such as testing of pressure vessels, different geometric tanks, aircrafts, piping systems, bridges and other constructions for the detection of faults or leakage, as well as in laboratory tests for the inspection of materials related to the plastic deformation mechanisms, such as erosion or fracture. The AET is the only method of non-destructive testing that can check in short time period large structures in their entirety, without requiring surface scan by a sensor. The difference between the AET and other non-destructive techniques is that AE detects the activity inside the material, while the other techniques examine the internal structure of the materials (Hardy and Shen, 1992). Additionally, AET needs the placement of sensors on the surface of structure or specimen being examined. In contrast, the other methods have to access the whole structure which often needs to be examined in laboratory conditions.

3.3 Types of Acoustic Signals

The transient elastic waves that produced from the source within the material under test are propagated through it and are detected by the receiving transducers which are located on the surface of the material. The signal which is recorded by the sensors conveys all the information from the source, the propagation medium and the characteristics of the detection sensor. These signals are illustrated as waveforms and divided into transient (or burst) and continuous type, depending on their source. The transient (or burst) type signals originate from individual emission events and continuous type signals are generated from mechanical noise or produced by time-overlapping

signals. Figure 3.2 illustrates an example of these two types of signals i.e. (a) a waveform of repetitive recordings and (b) a waveform of individual recording.

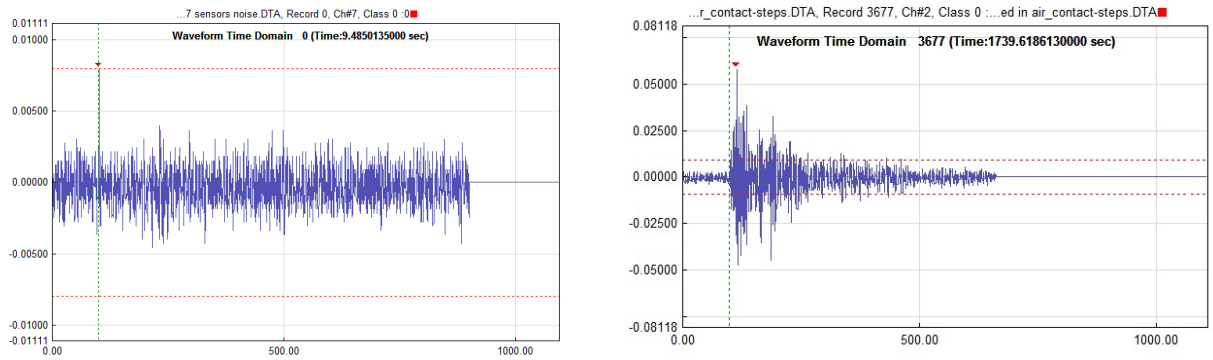

(a) (b)

Figure 3.2: Acoustic emissions waveforms of (a) continuous type signal and (b) burst type signal.

3.4 AE Parameter Analysis

In AET the detected waveform by the sensors conveys a lot of important information that helps in the comprehension of the process that is followed for the signals creation in a region. According to specific waveform parameters, such as the amplitude, risetime, counts, frequency, and duration, the flaws can be easily classified into two different types, as will be mentioned bellow (Hisham and Elfergani, 2013). Figure 3.3 shows a typical waveform with the basic information included in an AE signal. The hit based features and their definition are included in Table 3.1.

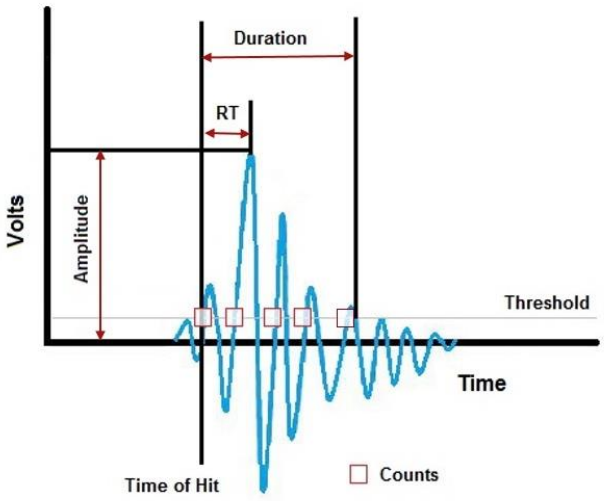

Figure 3.3: Commonly measured parameters of a waveform.

Table 3.1: Acoustic Emission parameters and their definitions (Physical Acoustics Corporation, 2007; Grosse et al., 2008).

Acoustic Emission Parameters	Parameter Definitions
Absolute Energy (AbE)	The released energy of AE hit in attoJoule (10^{-18} Joule). Range: 0.931 zJ – 26.1 nJ
Amplitude	The maximum voltage of detected signal during a hit, expressed in decibels (dB) scale. The amplitude is closely related to the magnitude of the source event (Grosse *et al.*, 2008) and is estimated in dB from the following expression: $dB = 20\log\left(\frac{V_{max}}{1\mu Volt}\right) - preamplifier\ gain\ in\ dB$
Average Frequency	The average frequency is derived from other AE parameters such as Counts and Duration. The Average Frequency is the number of Counts divided by the Duration.
ASL (Average Signal Level)	The measured of the continuously varying and averaged amplitude of the AE signal. The difference of ASL and RMS is that the RMS is measured in Volts whereas the ASL in dB. Range: 0-100 dB
Counts	The number of times the signal exceeds the threshold. Also known as "ring down counts" or "threshold crossing counts".
Counts to Peak	The number of times the signal crosses the threshold, until the largest voltage or the peak of the amplitude.
Duration	The time that the signal triggered (the first threshold crossing) until the last upper threshold crossing. Duration is expressed in microseconds (μs). Range: 0-1000 msec
Energy	The integral of the absolute value of voltage over the duration of the AE hit. This parameter gives information about the strength of the source event.

Event	A local material change giving rise to acoustic emission.
Hit	The process of detecting and measuring an AE signal on a channel.
Average Frequency	The average frequency of the waveform is calculated from the first threshold crossing to the maximum amplitude. It is calculated from the following expression: $f_{ave} = \frac{AE\ counts\ to\ peak}{Risetime}$
Reverberation Frequency	The average frequency determined after the peak of the AE waveform. It is calculated from the following expression: $f_{rev} = \frac{AE\ counts - counts\ to\ peak}{duration - rise\ time}$
Rise Time (RT)	The time (in μs) between the first count or the first threshold crossing and the peak of the amplitude.
Rise Angle (RA)	The ratio of Rise Time (RT) to Amplitude of a waveform (in μs/V). It is calculated from the following expression: $RA = (Rise\ Time)/Amplitude$
RMS (Root mean square)	The instantaneous measure of voltage (in V) of AE signal. Range: 0-6 Volts
Signal Strength	The voltage integral of a detected AE signal throughout the total waveform. Also known as "MARSE" or "Relative Energy".
Time of hit	The time at which the signal triggered and has been detected by the system.
Threshold	The minimum voltage value that has been set for noise elimination, in order the system to detect the AE hit. Range: 14-99 dB

It is important to mention that for the obtained AE signals two approaches exist. The recorded data that depends on the set value of the threshold are classified as Hit Driven Data (HDD), namely amplitude, duration, signal strength, etc., whereas those that are independent of this parameter are categorized as Time Driven Data (TDD), such as threshold, absolute energy, average signal level and root mean square. Another important characterisation is the fracture type which can easily be observed mostly on concrete specimens. It is understandable that the amplitude of an AE waveform shows the scale of the event and respectively the emitted energy indicates the crack opening displacement (Aggelis *et al.*, 2011). Except from these two parameters, the Rise Angle, and the Average Frequency play a key role in recognition of cracking mode. As shown in Figure 3.4, if the Rise Angle is high and the Average frequency is low, then the event is classified as the shear cracking type while the inverse describes a tensile event.

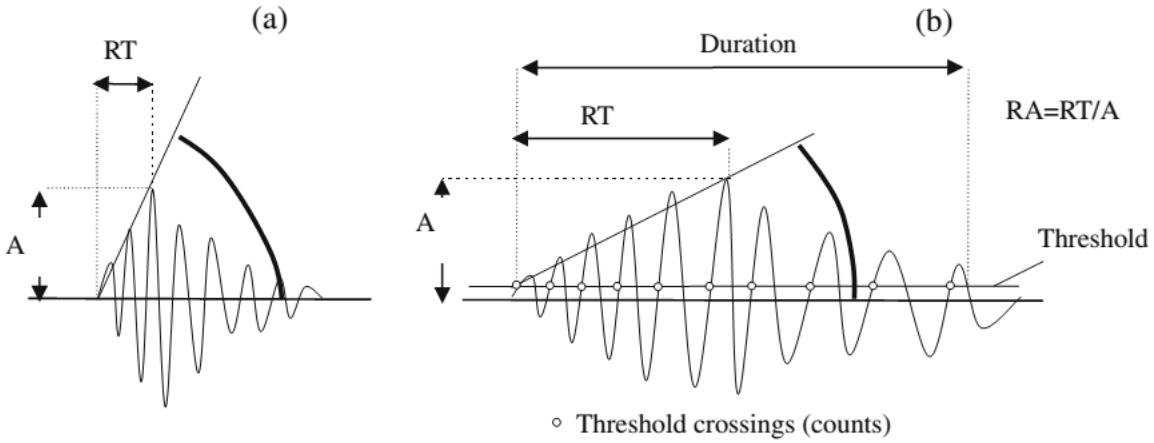

Figure 3.4: Typical waveform of (a) tensile and (b) shear event. (Soulioti et al., 2009).

Finally, it is useful to mention the effect of the applied load on a material to the observed AE activity. Obert and Duvall (1945) from the U.S. Bureau of Mines, conducted experiments of uniaxial compression on several types of rocks and showed that the rate of AE increases proportional to the applied load. An important study has been reported by Mogi (1962) who had proved that there are four zones which show the different behaviour of specimens during their uniaxial compaction and after Mogi's work, Boyce *et al*. (1981) completed this work (Asaoka *et al*., 1997). The four zones during the fracture of specimen are illustrated in Figure 3.5. The zone A-B represent the closing of cracks, B-C corresponds to the linear elastic deformation, C-D is related to the stable fracture propagation and D-E where the AE activity increases rapidly corresponds to the unstable fracture propagation.

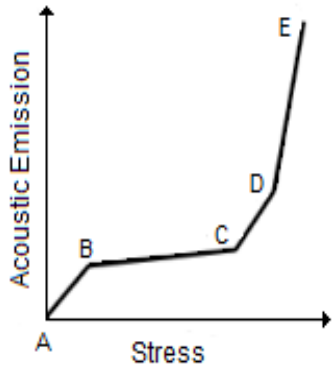

Figure 3.5: Stress versus Acoustic Emission activity for the fracture of a brittle rock under uniaxial compression (Boyce et al., 1981).

3.5 Waves Propagation

When the tectonic stresses exerted on the rocks inside the Earth load them beyond their breaking point, the rocks are disrupted and are displaced violently across a surface (fault) by emitting seismic waves. These waves during their passing from the various layers of the Earth are reflected, refracted, scattered and reaching recording stations, they have been enriched with new phases. Thus, the recordings of seismic waves are complex in form and consist of a sequence of seismic phases which are recognized by the change in the amplitude and often of their period. The duration of the various phases ranges from a few minutes for small and close earthquakes, up to few hours for large and distant earthquakes.

The velocity of seismic waves, which are mechanical waves, depends on the density and the elastic constants of the propagation medium. For seismic waves, it is easy to make the following assumptions:

- The seismic waves propagate inside the rocks which have perfectly elastic properties i.e., the deformation is a linear function of stress (Hooke's law).
- In rocks, the elastic properties are the same in all directions (isotropic material).
- The relative displacements of materials points are infinitesimal.

There are two main categories of seismic waves:

- Body waves
- Surface waves

3.5.1 Body Waves

Body waves are spherical elastic waves generated at the time of rock rupture and propagate in all directions. In this category, belong the longitudinal and transverse waves. Longitudinal waves are also known as primary waves (P-waves) because these are the first waves that arrive at the recording station. The particles in the solid vibrate along the direction of propagation of the wave energy (Figure 3.6).

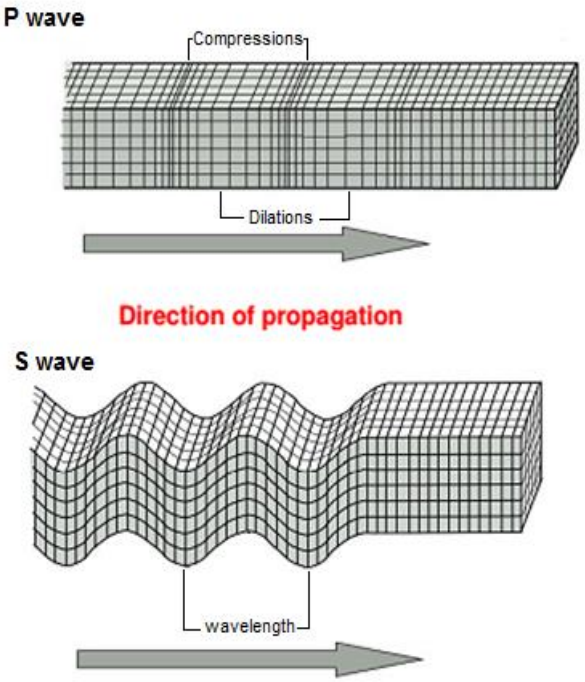

Figure 3.6: P and S waves in a finite medium.
(http://kiska.giseis.alaska.edu/input/west/guides/amato_faulting/wave_types.jpg)

The transverse waves, which are the second waves arriving at the recording stations, are known as secondary waves (S-waves). The material particles under the action of shear stress (τ) oscillate in vertical planes in the propagation direction, similar to the electromagnetic waves. Generally, for an isotropic elastic medium, the propagation velocities of P- and S-waves are given by the following relationships:

$$U_p = \sqrt{\frac{\lambda+2\mu}{\rho}}\,,\; U_s = \sqrt{\frac{\mu}{\rho}} \qquad (3.1)$$

where ρ is the density of the material and λ, μ are the Lamé constants. These velocities are affected by various factors such as the temperature, pressure, composition of the material and the mechanical condition. These are the main factors which may cause the

closing of micro-cracks and gaps, and increase elasticity, causing an increase in the elastic wave propagation velocity in the rocks.

3.5.2 Surface Waves

Surface waves in contrast to body P and S waves are not generated in the focus of the earthquake source (hypocenter). The surface waves are secondary waves originating from the superposition, under appropriate conditions, of the P and S waves in the Earth's free surface, or on a lower velocity layer than that of the surrounding area. They are recorded in the stations after the arrival of the P and S waves.

In addition, the surface waves are not propagated in all directions inside the Earth but transfer the greater energy proportion of shallow earthquakes (h <40km), causing greater destruction than the corresponding primary body P and S waves. However, their amplitude (*A*) decreases abruptly with depth, according to the following exponential relationship:

$$A \propto \exp(-\frac{qh}{\lambda}) \qquad (3.2)$$

where *λ* is the wavelength, *h* is the depth and *q* is a constant which depends on the propagation medium. This means that as the depth of the earthquake focus increases, the amplitude of surface waves becomes smaller and insignificant as compared to the amplitude of P and S waves. Therefore, in deep earthquakes we do not observed surface waves.

There are two basic types of surface waves (Figure 3.7):

- Love waves, which are horizontally polarized waves (SH) and
- Rayleigh waves, where the motion of matter particles is elliptical and reverse to the direction of propagation while they have a vertical polarization (SV).

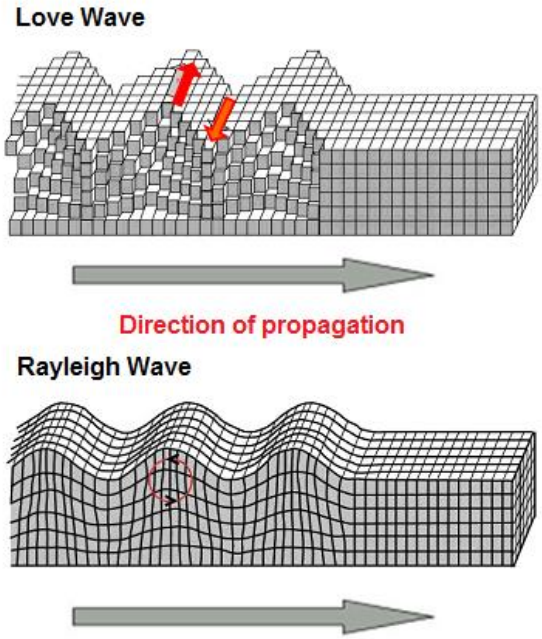

Figure 3.7: Love and Rayleigh waves.
(http://kiska.giseis.alaska.edu/input/west/guides/amato_faulting/wave_types.jpg)

In analogy to the seismic waves which are propagated inside the Earth, the acoustic emissions in a finite medium, such as a rock specimen or a geometrical structure (vessel, pipe, etc.), exhibit similar behaviour. However, due to the limited size of the specimens, other types of elastic waves (Lamb and Head waves) can be observed in semi-infinite or bounded media.

3.6 Location of Acoustic Emission Sources

The information for the active damage of an area can be related to AE source location using two or more sensors placed properly on the surface of the material under investigation. The most important method is the time of arrival (TOA) which is the travel time of an acoustic wave emitted from a transmitter to the receiver. During the recording of AE hits by each sensor, the location of an event source can be determined if we know the wave velocity inside the specific material and the difference in arrival time of each hit between the sensors. The latter is measured by dedicated computer software.

Systems that measure the TOA can exactly locate the signals in linear location (1D), two-dimensional source location (2D or planar location) and three-dimensional source location (3D). The differences of these techniques are the number of the required

sensors and the geometrical properties of the material under test. In the following sections we will explain these techniques in more details by giving appropriate examples.

3.6.1 Linear Source Location

In general, the linear location technique is used in structures which have one dimension significantly larger than the others. In this case, a minimum number of two sensors is required, in order to locate the sources of AE events. There are several methods but the most important method in linear location technique is the calculation of the time difference (TD). For better comprehension of the TD method let assume that two sensors are placed on the edges of a rectangular structure, as shown in Figure 3.8, which are mentioned by CH_1 for sensor 1 and CH_2 for sensor 2. The SL indicates the source location, T_1 and T_2 are the TOA to sensor 1 and sensor 2 respectively, D is the distance between the two sensors, D_1 is the axial distance of sensor 1 to AE source and *V* is the wave velocity of the material. The following relation is used to measure the distance from the source location to the nearest sensor (Tawhidul *et al*., 2014).

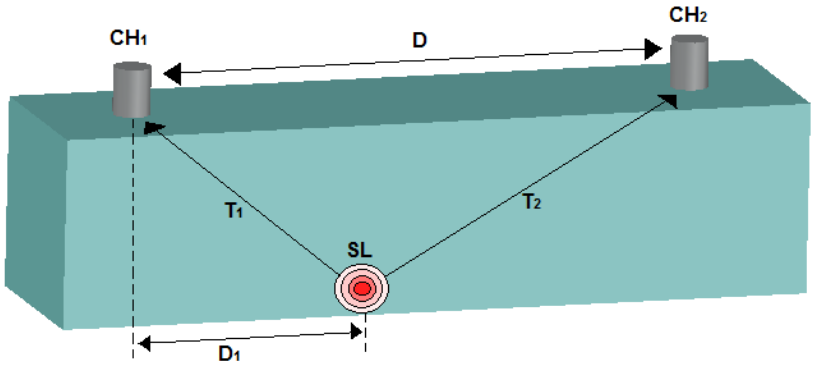

Figure 3.8: Linear source location technique on a rectangular structure.

$$D_1 = \frac{1}{2}(D - \Delta T \cdot V) \tag{3.3}$$

where ΔT is the time difference between sensor 1 and sensor 2.

3.6.2 Two-Dimensional Source Location

The technique of two-dimensional source location is used to the most applications on planar surfaces or specimens where one of its dimensions is small and the minimum number of required sensors is three. Figure 3.9 considers three sensors (S_1, S_2 and S_3) placed at different distances on a planar structure. The source produce an elastic wave which propagates in every direction, as shown in Figure 3.9, and the sensors detect this wave in different distances. The location of the source will be located at the intersection of three circles with centres the locations of the sensors and radii equal to the distances of the wave which were recorded by each sensor.

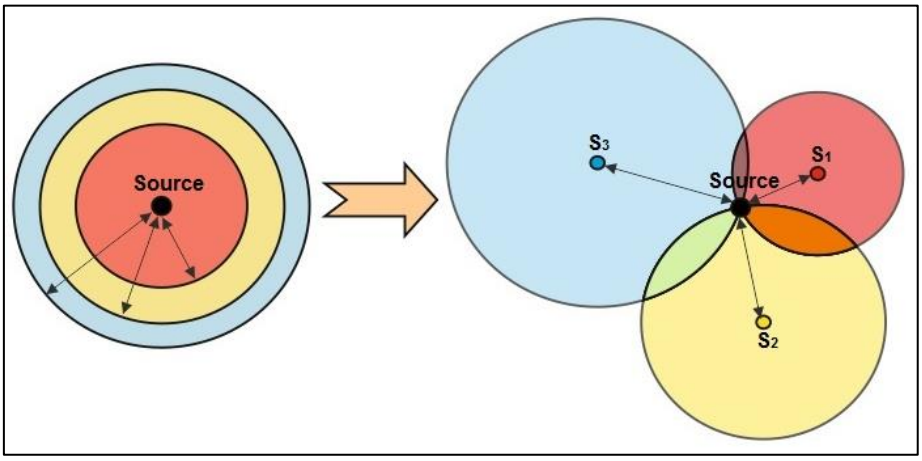

Figure 3.9:Two-dimensional source location on a planar.

3.6.3 Three-Dimensional Source Location

To determine a three-dimensional source location of an event, it is important to detect the emitted signal at least from four sensors. This technique needs three coordinates to calculate the source location and for this reason the sensors must be placed in different positions. For example, if a coordinate is the same for all sensors this will lead to wrong calculations for three-dimensional source location. An example of a 3D location of AE events during the uniaxial loading of a rock specimen is shown in Figure 3.10.

The source location of AE events is derived by multiple regression analysis through the minimization of the quantity χ^2, defined as:

$$\chi^2 = \sum_i (\Delta t_{i,obs} - \Delta t_{i,calc})^2 \qquad (3.4)$$

where $\Delta t_{i,obs}$ is the time difference of the arrival times of the hits detected by the 1st and the ith sensor and $\Delta t_{i,calc}$ the calculated time difference which is given by:

$$\Delta t_{i,calc} = \frac{\sqrt{(x_i - x_s)^2 + (y_i - y_s)^2} - \sqrt{(x_1 - x_s)^2 + (y_1 - y_s)^2}}{v} \qquad (3.5)$$

where $(x_i, y_i)(x_1, y_1)$ are the coordinates of the ith and 1st sensors, (x_s, y_s) the unknown coordinates of the source and v the wave propagation velocity in the material (Agioutantis *et al.*, 2016).

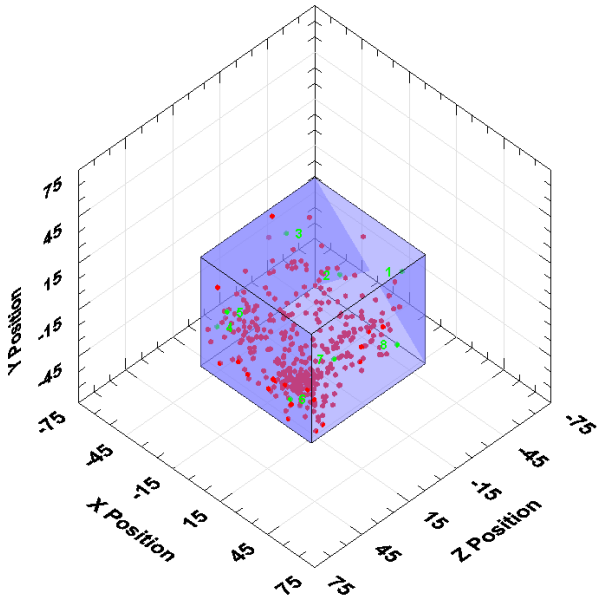

Figure 3.10: Three-dimensional source location on a cubic rock specimen subjected to uniaxial loading.

3.7 Methods of Monitoring Acoustic Emissions

The acoustic emissions that produced due to deformation or failure of a solid material, propagate as elastic stress waves through the material. These waves travel from the acoustic emission source to the material boundaries. A transducer which converts the elastic wave that reaches to the material boundary to an electrical signal is used for monitoring the AE activity. By using the appropriate equipment and software, we can proceed further to the analysis of the AE recordings. To monitor the AE activity, the following equipment is necessary:

- transducer,

- preamplifier,
- bandpass filter,
- electronic equipment and software.

It is important to mention that, for monitoring the AE, the appropriate transducer should be selected. Depending on the application, the selected transducer must be able to monitor the frequency band of the acoustic emissions. In laboratory experiments, the frequencies of the AE waveforms can be in the range of 10^3 to 10^6 Hz, i.e. up to the range of ultrasounds. Subsequently, the required equipment include preamplifiers, band-pass filters, and a recording method of waveforms that are generated. The preamplifiers are used to amplify the received weak signals from sensors, while the band-pass filter is required to filter the external low and high-frequency signals, which are considered as noise. Finally, the recorded waveforms can be analysed with dedicated software.

3.8 Advantages and disadvantages of Acoustic Emissions

In order to have a complete overview of the AET, the most important advantages and disadvantages are summarized to the following table.

Table 3.2: Advantages and disadvantages of the AET.

A/A	Advantages	Disadvantages
1	Determination of crack growth position	On specific structures, the AE signals are developed during the load, when the structure reaches to the yield point
2	Determination of cracks categorization by waveforms analysis	Difficult to distinguish between the real acoustic emission signals and noise from the environment during the measurement
3	Monitoring the whole structure	On specific structures, the amplitude of AE signals is small and this makes difficulty to their detection
4	Real-time monitoring	Difficult to estimate the location of AE in non-homogeneous structures because of different propagation velocities
5	Monitoring structures that are overlapping with insulating material	In long-term tests, the counter may become overloaded and data be lost

3.9 Kaiser and Felicity Effect

According to the German researcher Joseph Kaiser (1953), the materials retain a “memory” of previously applied stresses (Hardy, 2003). Stress memory is one of the most important characteristic of natural heterogeneous materials. The Kaiser phenomenon is the absence of AE activity in a material subjected to mechanical loading, until to overcome the previous maximum load. The Kaiser effect is illustrated in Figure 3.11, which shows the cumulative AE hits versus the applied load. The path AB shows the AE activity that is recorded during the loading and the path BCB when the load is removed and reapplied. In the latter case, we observe that although the load is applied from C to B, there are no AE events until the load at point B exceeds its previous value and AE increases rapidly, up to the point D. The path DE corresponds to the removed load, while at point F the applied load is high enough to produce events before the previous maximum load (point D) is reached. This effect is known as Felicity effect and is the conjugate of the Kaiser effect.

The quality of the Kaiser effect under saw-tooth uniaxial conditions is usually quite high over a wide range of stresses from about 30% to about 80% of the strength (Lavrov *et al*., 2002; Lavrov, 2003; 2005). It is expressed by the Felicity ratio (FR) which is defined as:

$$FR = \frac{P_F}{P_D} \tag{3.6}$$

where P_F is the stress at point F where AE activity starts to be recorded and P_D corresponds to the previous maximum load (point D). In other words, FR can be defined as the ratio of the load at which significant emissions starts before the previous maximum load. The lower of the unit is this ratio, the greater of the failure to the material. So, when the ratio tends to zero, the material is completely damaged.

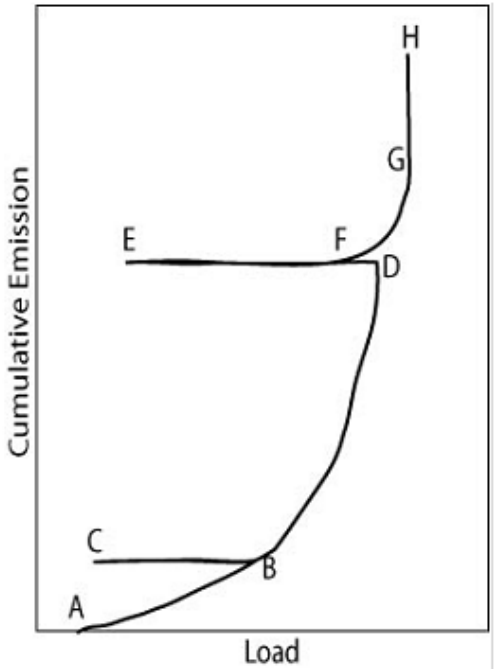

Figure 3.11: Schematic representation of Kaiser and Felicity effect (Physical Acoustics Corporation, 2007 and Grosse et al., 2008)

3.10 Amplitude Distribution

In seismology, there is a significant parameter which is originated from the magnitude distribution of data and is known as b-value. The b-value is defined as "the log-linear slope of the frequency – magnitude distribution of the seismic events" (Stergiopoulos *et al*., 2012). The relationship of Gutenberg – Richter substantiates a statistical relationship between the earthquakes magnitude and their repetition time:

$$\log N = a - bM \tag{3.7}$$

where N is the number of earthquakes greater than or equal to magnitude M, α is the number of earthquakes with zero magnitude (constant) and b is the b-value (constant close to 1). Several works have shown that b-value can be used to identify fracture which is useful in seismology. In the case of AET, the above relationship has been modified as follows:

$$\log N = a - b(\frac{A_{dB}}{20}) \tag{3.8}$$

where A_{dB} is the peak amplitude of the AE events in decibels and N is the number of AE hits with amplitude greater than the predefined threshold (Stergiopoulos *et al*., 2012). It is important to mention that a high b-value indicates the appearance of micro-cracks (AE hits or events), whereas low b-value shows the presence of macro-cracks. Micro-cracks release AEs with low amplitude and macro-cracks with high amplitude. The b-value analysis is applied to a certain range of events, for example 50 events for each group and if the lag of events is 5 than 50, e.g. 1 to 50 event the next range is 6 to 56 event than 51 to 100 event, contributes a better time resolution of the b-value changes during the experiment.

Besides the seismic b-value, Shiotani *et al.* (1994) introduced the concept of improved b-value (Ib-value) which is suitable for AET on any kind of materials such as concrete and rock. The range of AE amplitude in improved b-value is determined by specific statistical values which are the mean value (μ) of the magnitude distribution of one range of events and the standard deviation (σ) of the magnitude distribution of the same range of events. The Ib-value is defined as:

$$I_b = \frac{\log_{10} N(w_1) - \log_{10} N(w_2)}{\sigma(\alpha_1 + \alpha_2)} \tag{3.9}$$

where α_1 and α_2 are constants, w_1 and $w_2$represent the lower and upper amplitude respectively and N is the accumulated number of events with amplitude over w_1 and w_2, which is given by:

$$N(w_1) = \int_{\mu-\alpha_2\sigma}^{\infty} n(\alpha)d\alpha = N(\mu - \alpha_2\sigma) \tag{3.10}$$

$$N(w_2) = \int_{\mu+\alpha_1\sigma}^{\infty} n(\alpha)d\alpha = N(\mu + \alpha_1\sigma) \tag{3.11}$$

In Eqs (3.10) and (3.11), $n(\alpha)$ is a number of AE at $d\alpha$ and the interval of amplitude analysed would be $\sigma(\alpha_1 + \alpha_2)$. According to Shiotani (1994), Ib-value can be used to evaluate the processes of fracture in rock, soil and concrete. It is also very important to note that Ib-value is calculated on the basis of decibel units and if it is compared with seismic b-value then the Ib-value must be multiplied by 20.

Chapter 4: Physical Properties of Rocks

4.1 Sandstone

The sedimentary rocks are formed by deposition or cementation of the materials that are dissolved in a fluid medium (water or air) and the subsequent bonding of the materials that were deposited. The process of solidification of the sediment takes millions of years and is called diagenesis. The categorizing of diagenesis is done according to process (crystallization, replacement and compaction), to the time of this process (early, late, etc.) or to the path of fluid migration (upwards or downwards).

The three categories of sedimentary rocks are clastic rocks, chemical sediments and organic sediments. The clastic rocks are formed from the weathering of other rocks and classified according to the average grain size of rock particles (Table 4.1). However, the chemical sediments are formed by chemical processes mostly from solutions precipitation and the organic sediments by organic processes. Sandstone is a clastic sedimentary rock composed of sand grains (primarily quartz sand) held together by adhesive substances and rock grains. Sandstone is porous and has the ability to filter and store large amounts of liquid and for this reason, it is commonly associated with the presence of water and oil reservoirs. Mining, processing and use of sandstone as construction material may result in silicosis and diseases in respiratory system.

Table 4.1: Classification of clastic rocks according to grain size (Boggs, 2009).

Type		Grain Size	Rock
Gravels	Boulder	>256mm	Conglomerate
	Cobble	64-256mm	
	Pebble	4-64mm	
Sands	Coarse	0.5-2mm	Sandstone
	Medium	0.25-0.5mm	
	Fine	0.06-0.25mm	

The basic stages of sedimentary rocks formation are the following:

1) Weathering-Erosion which are the physical, chemical and biological processes on pre-existing rocks leading to their destruction.
2) Transportation of materials occurred from weathering, by wind and water of rivers and seas.
3) Deposition of materials found in suspension or dissolution. The deposition is done in successive layers.
4) Diagenesis is the procedure that a loose sediment is converted to solid rock.

4.2 Rock properties

As it mentioned previously the sandstone is a porous medium and that is the underlying reason for selecting this rock in this thesis. The pore space properties are matter of importance to understand the interaction between fluid and rock and to describe the pore volume and flow behaviour of reservoirs.

4.2.1 Porosity

Porosity is an important rock parameter because describes the potential storage volume and contributes information for physical rock properties. The relationship 4.1 shows that porosity (Φ) is defined as the fraction of pore volume (V_{pore}) to the total rock volume (V_{bulk}) and is expressed either as a fraction or in percent. The pore volume is determined as the rock volume without the volume of solid particles (V_{solid}).

$$\Phi = \frac{V_{pore}}{V_{bulk}} = \frac{V_{bulk} - V_{solid}}{V_{bulk}} \qquad (4.1)$$

The porosity can be divided into two types the primary and the secondary porosity. Primary porosity is the main porosity of rock that formed during the deposition of rock grains such as the sandstones that their porosity is determined by the diagenesis process according to originally deposition. Secondary porosity can result from the chemical leaching process or the cracks that produced on the rock internal. It is important to refer the classification of porosity according to reservoir description which are total and effective porosity. Total porosity is the fraction of bulk volume which includes the total pore space or

disconnected porosity while effective porosity is the fraction of bulk volume which includes the interconnected or effective porosity that allows the fluid flow.

The most important factors that affect the porosity of a rock is the size of the grains in the interior of the rock and the compression exerted on the rock. If small particles are mixed with larger then porosity will be reduced on the contrary if there is uniformity in the size of the grains, then the porosity is larger. In addition, the porosity decreases because of compaction that is a result of the pressure exerted due to overburden sediments. The process of compaction provokes to reduce the pore space and this means that porosity is lower in deeper layers than the superficial. Eventually the porosity after the compaction process is calculated by (Athy, 1930):

$$\Phi_z = \Phi_0 \cdot \exp(-b \cdot z) \qquad (4.2)$$

where Φ_z is the porosity of rock in depth, Φ_0 is the porosity at reference depth (z=0), b is a parameter characterizing the sediment compressibility and z is the actual depth.

In this study, the samples were oven-dried for 24 hours at 105°C and afterwards the dry weights were measured. Then the samples were placed in a chamber with water until were saturated completely and weights were measured. The porosity of sandstone was calculated according to equation 4.1 and the result was ~7%.

Additionally, porosity is also affected by grain packing. In Figure 4.1 different grain packing configurations are presented using spherical grains and the maximum porosity is calculated in percent for each one separately.

In the present work, the apparent porosity *P* (expressed in percent) was determined by the evacuation method, according to the following relation:

$$P = \frac{W - D}{W - S} \mathrm{x}100 \qquad (4.3)$$

where *W* is the weight of the saturated specimen, *D* is the dry weight and *S* is the weight of the suspended specimen inside the immersion liquid (water).

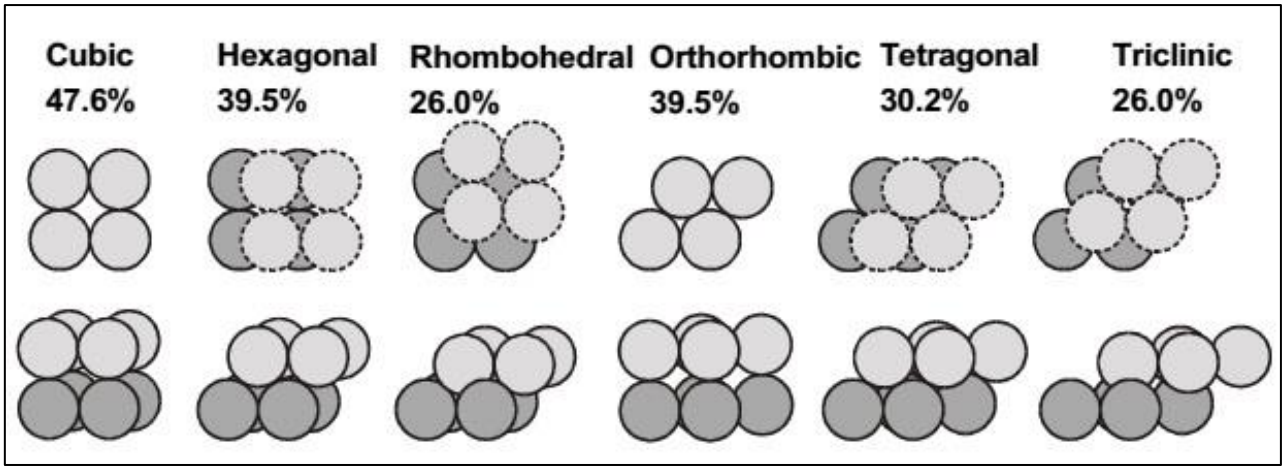

Figure 4.1: Grain packing and porosity (Glover, 2000).

4.2.2 Strength

The strength of a rock depends mainly on its components, the connection of grains in the rock, the grain size, any pre-existing low cohesion surfaces (cracks and veins), the porosity and the content of water. In addition, rock strength depends on a number of external factors such as the type of external loads (uniaxial, multiaxial, etc.), the path of the loading stress (linear, cycling, stepped, etc.) and the physical and chemical conditions such as temperature, humidity, etc. There are five different ways to load a material: a) compression in which the two opposite sides of a material specimen tend to be pushed together, b) tension in which two opposite sides of a specimen tend to be pulled apart resulting in elongation, c) shear in which two opposite sides of a specimen is pushed in different directions, d) bending in which one side of the material is compressed and the other is stretched and e) torsion in which loading causes twisting of a specimen.

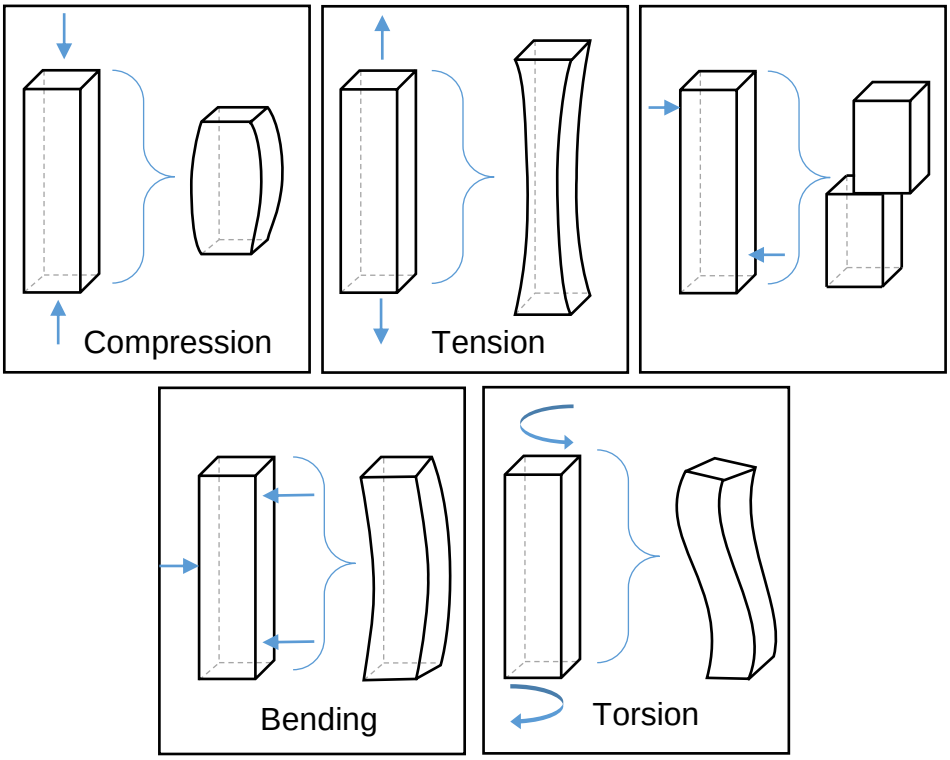

Figure 4.2: Fundamentals types of loading.

4.3 Stress-Strain curve

Stress (σ) is defined as a system of internal forces of a material that is formed as a consequence of the reaction to an external force which acts on it and modifies its shape or volume, while strain (ε) is the measure of the material deformation. There are different types of stresses that depend on how the force is exerted on the surface of the material (uniaxial compression, confined compression or triaxial or polyaxial compression). In this thesis, specimens will be loaded in uniaxial compression which means that the lateral surface of each specimen is free of traction (Jaeger *et al*., 2007).

The load that is applied to a material causes deformations which are distinguished in transient or elastic region where the materials are completely reverted to their initial state after unloading and permanent or plastic where the deformations remain after unloading. It is commonly accepted that materials behave differently during loading; those that present insignificant deformations before failure are called brittle materials. In contrast, materials that present significant deformations during loading are called ductile materials. Figure 4.3 depicts typical stress-strain curve for brittle and ductile materials; it is obvious that brittle materials present little or no plastic deformation in contrast to ductile materials.

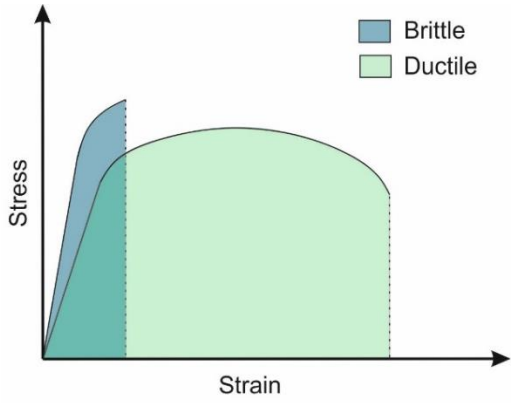

Figure 4.3: Stress-strain curve for brittle and ductile materials.

A typical stress-strain curve for a rock under uniaxial compression (Figure 4.4) is divided into four regions which explain the behaviour of the rock during loading. The first region (A) typically corresponds to pore closure, while region B is linear and typically corresponds to a linear relationship between axial stress and axial strain. If the specimen is subjected to uniaxial compression, the changes such as the closing of pores and discontinuities are not permanent in these regions because the rock typically exhibits an elastic behaviour. Region C is a non-linear curve and the slope of this region decreases (Jaeger *et al.*, 2007). It is interesting to note that in this region the stress ends at the highest point of this curve and the rock deformation is irreversible. The peak of the stress-strain curve corresponds to the ultimate strength of the material. This region includes the plastic region for ductile materials. The last stage (D) corresponds to the post failure part of the stress strain curve. This region is difficult to observe on experiments because the failure that starts from the maximum strength progresses quickly. It can only be observed is tests are performed in displacement control rather than load control.

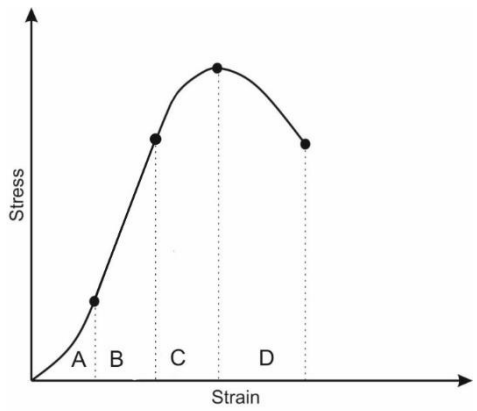

Figure 4.4: Stress-strain curve for rock under compressive load.

4.4 Description of uniaxial testing

The uniaxial compression test is a simple way of loading where the sample is subjected to compressive stress along a single axis and results in the reduction of the length or height of the sample (Figure 4.5). According to ISRM (International Society for Rock Mechanics) and USBM (US Bureau of Mines) the diameter of the cylindrical sample should be at least 10 times the maximum grain size of the specimen (Hudson *et al.,* 1993). The compressive strength (σ) could be defined as the maximum applied load (F) divided by the original specimen area (A_o):

$$\sigma = \frac{F}{A_o} \tag{4.4}$$

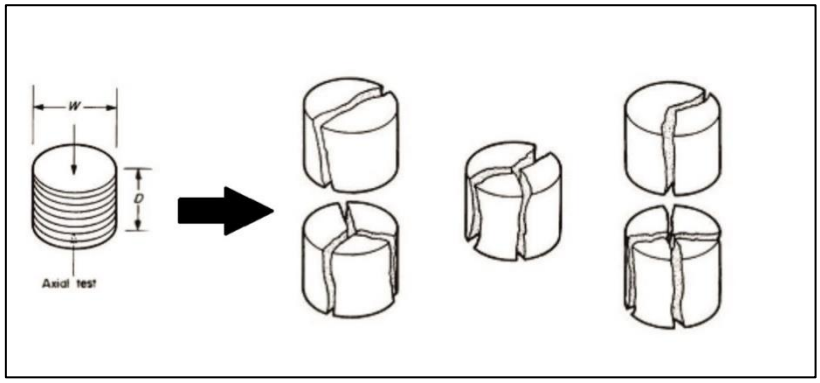

Figure 4.5: Uniaxial compression test and different types of failure of cylindrical specimens (Hudson J.A. et al., 1993).

4.5 AC-conductivity

The conductivity of a specimen was measured using two cylindrical electrodes which were disposed parallel to the two opposite sides of the specimen. An alternating voltage (AC) of 0.01Hz, 10kHz, and 200kHz was exerted between the electrodes with the specimen playing the role of the resistance between the two conductors. The alternating voltage was selected for avoiding the electrolysis of the fluid located in the specimen voids, which in this case is water. A conductivity meter which was connected to electrodes was used to measure the current conducting through the sample. The measured conductivity (G) is given in units of Siemens per centimeter (S/cm) which is equal to Ω^{-1}/cm, namely it is the inverse of the measuring unit of resistance and is defined as:

$$\mathrm{G}=\frac{1}{R}=\frac{I}{V} \tag{4.5}$$

where R is the resistor (ohm), I is the current (Ampere) and V the voltage (Volts).

Chapter 5: Instrumentation and Experimental Procedure

5.1 Introduction

In order to investigate the mechanical and electrical behaviour of sandstone samples under uniaxial compression, a number of experiments were conducted in the laboratory, by combining the AET in conjunction with electrical conductivity measurements. Different types of uniaxial loading were carried out such as linear, stepped and saw-tooth loading, while three different geometries of sandstone samples were used. Three cubic specimens were subjected in linear uniaxial compression, two prismatic specimens in linear and stepped loading and finally six cylindrical specimens in all kinds of uniaxial compression.

5.2 Description of experimental setup

The experiments were carried out by means of specific equipment which will be described in detail below. An array of piezoelectric transducers was attached to the surface of the sandstone specimens with hot silicone glue which was used as a coupling and bonding material. The sensors were in turn connected to preamplifiers and then to the data acquisition system. Figure 5.1 illustrates a simple schematic setup for recording acoustic emissions. The numbers are referred to the instrumentation that was used in the laboratory experiments.

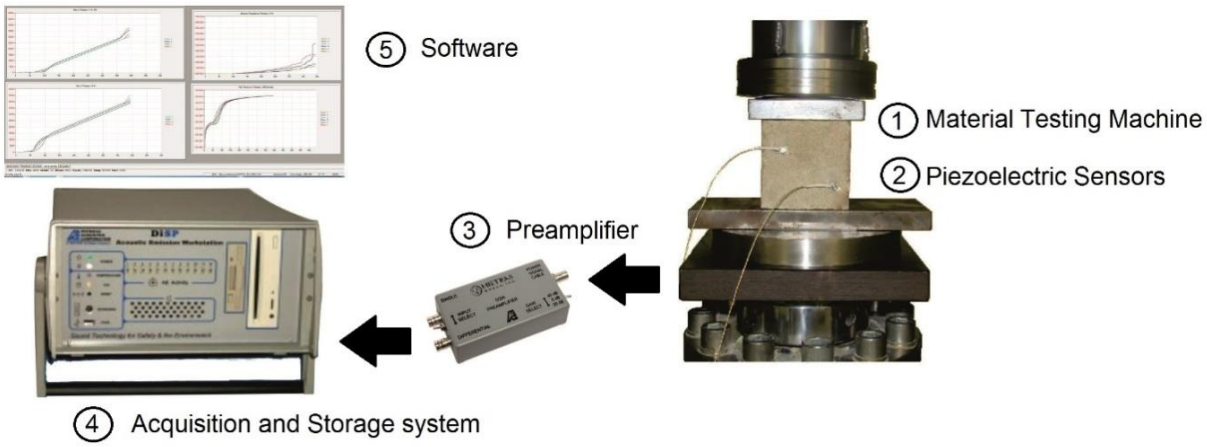

Figure 5.1: Schematic illustration of acoustic emission setup.

5.2.1 Material Testing Machine

In order to conduct the uniaxial compression tests on the Tyliss sandstone samples, two different testing machines were used. The first one is the MTS 815 system (Stavrakas *et al.*, 2004) and the second one is the ALPHA3-3000 system (Form+Test). The main specifications of the load machines are given in Table 5.1. The systems consist of the loading frame, the upper and lower loading plates, the intermediate loading plates and the spherical head base bearing. Load cell, which is located below the bearing plate, can measure independently the applied load. By using strain gauge sensors adapted on the surface of samples, the deformation of the specimens in axial and lateral directions can be also be accurately measured.

Figure 5.2: The uniaxial load testing machine (Form+Test ALPHA3-3000, 3000kNt), equipped with programmable digital control unit (AS C20 N).

Table 5.1: Specifications of MTS 815 and ALPHA3-3000 systems.

	MTS 815	ALPHA3-3000
Maximum Load (kN)	1600	3000
Maximum Force (kN)	1050	39700 kN/m^2
Weight (kg)	2359	1810

5.2.2 Piezoelectric Sensors

The AE activity during compression tests was recorded by using piezoelectric sensors (PICO HF-1.2, 200 kHz – 1MHz, Mistras Group, SA) which convert the mechanical energy of the emitted elastic waves to electrical signals (transducers). In the performed experiments, an array of pico sensors has been used, where each one receives an independent signal from the acoustic source, in order to be used for the location of the point source. For this reason, the minimum number of transducers required is four, while 4-8 piezoelectric sensors were used in the experiments. Figure (5.3) depicts the transducer that was used in the present experiments. The specific characteristics of the piezoelectric sensor HF-1.2 are shown in Table 5.2.

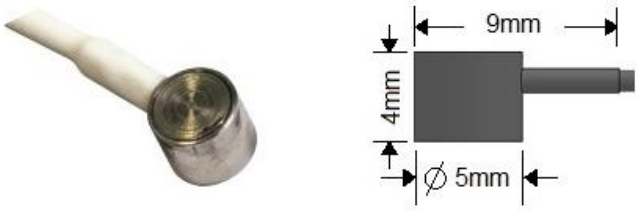

Figure 5.3: Pico sensor and its dimensions.

Table 5.2: Transducer Specification (Physical Acoustics Corporation, 2007).

Parameter	Value
Peak Sensitivity, Ref V/μbar	-72 dB
Operating Frequency Range	500 – 1850 kHz
Resonant Frequency, Ref V/(m/s)	600 kHz
Directionality	+/- 1.5 dB
Temperature Range	-65 to 177 °C
Shock Limit	500 g
Completely enclosed crystal for RFI/EMI immunity	
Case Material	Stainless Steel
Face Material	Ceramic
Seal	Epoxy

5.2.3 Preamplifiers

One preamplifier was attached each piezoelectric sensor. Their use is to amplify the detected signals and reduce noise and electromagnetic interference. Specifically, preamplifiers increase the quality of the signal so that it can reach the main unit through the connecting cables. The preamplifiers used are 0/2/4 which are supplied with 0/20/40 dB gain and the selection of the range is carried with a switch located on the amplifier (Figure 5.4).

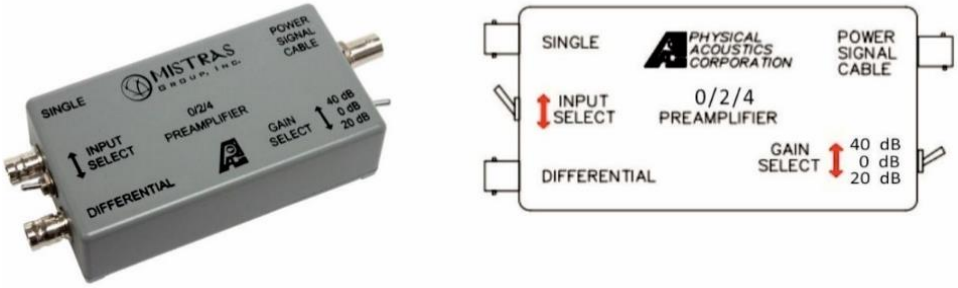

Figure 5.4: Preamplifier 0/2/4 (Physical Acoustics Corporation, 2007).

5.2.4 Acquisition and Storage System

The data acquisition system that was used is the DiSP (Digital Spartan) multichannel system by Physical Acoustics Corporation equipped with 4 PCI-2 cards. Each PCI-2 card has two channels for collection of high sampling acoustic emission data (sampling rate: 40 Msamples per s). This data acquisition system is a portable AE system, equipped with a handle for making easier the transport and an integral keyboard, making it ideal for both laboratory and field work.

Figure 5.5: Digital Spartan multichannel system (Physical Acoustics Corporation, 2007).

5.2.5 Recording and Analysis Software

The software used for data acquisition is AEwin package (PAC) whereas for the analysis and presentation of the data the NOESIS software was used. Subsequently, there will be a short presentation of these programs with their basic properties and basic settings that were performed in the experiments.

- ***AEwin Software***

The AEwin software is used for the real-time monitoring of the AE parameters and the recorded waveforms. Different kinds of graphs can be displayed on the screen, including 2-D or 3-D graphs, histograms, waveforms, point plots and others with colouring options. Graphs with location of events such as 2D Planar Location and 3D Location can be also displayed, which simulate structures of specific geometry with real dimensions, the exact location of sensors and the location of AE events in real time. In the location setup, it is important to select the type of location (i.e., 3D location, 2D Planar, etc.) and determine the velocity of the elastic waves for the specific kind of material. The placement of the sensors and the dimensions of specimen are imported from the location view settings. In the present work, the 3D location type was used for cubic and prismatic specimens and the 2D planar location for cylindrical specimens. Using this software is easy to Replay a recording data file of an experiment for additional analysis purposes. A specific AEwin layout as defined by the user is illustrated in figure 5.6.

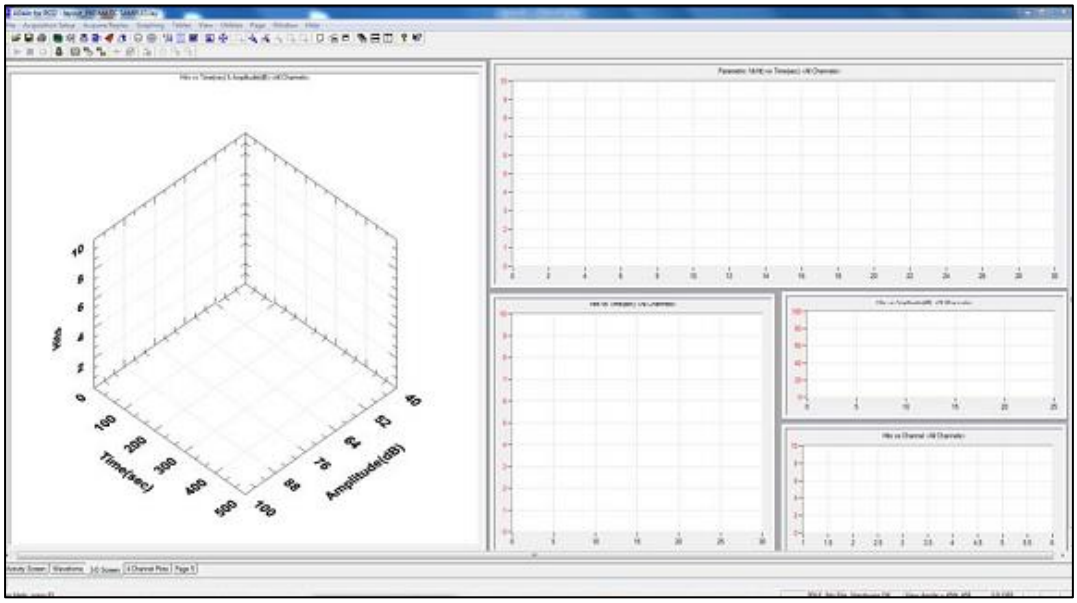

Figure 5.6: AEwin layout defined by the user.

The basic settings are implemented through the “AE Hardware Setup” of PCI-2 card to perform the experiments. More specifically, in the “AE Channel Setup” page we can specify the selection of the used channels and process their settings (Figure 5.7).

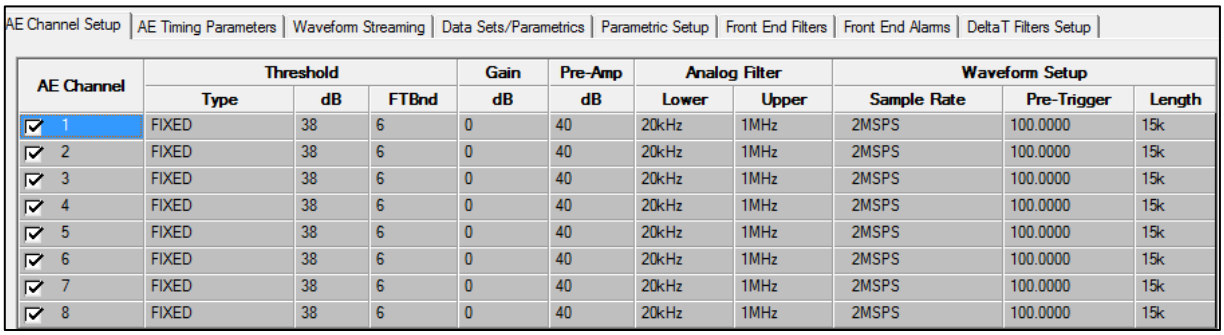

AE Channel Setup | AE Timing Parameters | Waveform Streaming | Data Sets/Parametrics | Parametric Setup | Front End Filters | Front End Alarms | DeltaT Filters Setup

AE Channel	Threshold			Gain	Pre-Amp	Analog Filter		Waveform Setup		
	Type	dB	FTBnd	dB	dB	Lower	Upper	Sample Rate	Pre-Trigger	Length
1	FIXED	38	6	0	40	20kHz	1MHz	2MSPS	100.0000	15k
2	FIXED	38	6	0	40	20kHz	1MHz	2MSPS	100.0000	15k
3	FIXED	38	6	0	40	20kHz	1MHz	2MSPS	100.0000	15k
4	FIXED	38	6	0	40	20kHz	1MHz	2MSPS	100.0000	15k
5	FIXED	38	6	0	40	20kHz	1MHz	2MSPS	100.0000	15k
6	FIXED	38	6	0	40	20kHz	1MHz	2MSPS	100.0000	15k
7	FIXED	38	6	0	40	20kHz	1MHz	2MSPS	100.0000	15k
8	FIXED	38	6	0	40	20kHz	1MHz	2MSPS	100.0000	15k

Figure 5.7: Option settings in AE Channel Setup page.

In “AE Timing Parameters” page the Peak Definition Time (PDT), the Hit Definition Time (HDT) and the Hit Lockout Time (HLT) may be specified. The values of 50μsec, 200μsec and 300μsec for PDT, HDT and HLT respectively, are usually the recommended values for non-metals specimens according to Physical Acoustics Corporation (Figure 5.8). The page “Data Sets/Parametrics” shows all the AE parameters (the desired parameters can be selected). Finally, from “Parametric Setup” page the user can calibrate the parametric inputs which are used to record analog signals from other sensors (load cell, strain gauges, etc.).

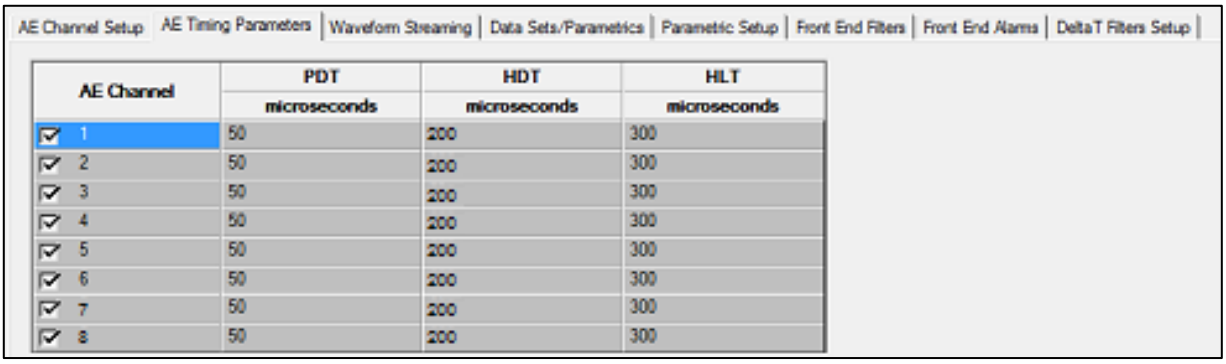

AE Channel Setup | AE Timing Parameters | Waveform Streaming | Data Sets/Parametrics | Parametric Setup | Front End Filters | Front End Alarms | DeltaT Filters Setup

AE Channel	PDT	HDT	HLT
	microseconds	microseconds	microseconds
1	50	200	300
2	50	200	300
3	50	200	300
4	50	200	300
5	50	200	300
6	50	200	300
7	50	200	300
8	50	200	300

Figure 5.8: Option settings in AE Timing Parameters page.

- ***NOESIS Software***

NOESIS is software designed for the analysis of AE data and offers functions to the experienced pattern recognition analyst (Mistras, 2013). Data are loaded in NOESIS software as *.dta files while, except the AE parameters, there is also the ability to load the

recorded waveforms of each corresponding hit. According to the available functions, it is possible to present in different ways the correlations between the AE parameters (Figure 5.9) and derive easily some conclusions for the experiments results. Additionally, this software offers tools for spectral analysis of each recorded waveform (FFT, DWT, CWT, Power Spectrum, etc.). It is important to mention that the user can load into the current data set more data files or parametric files created in any software in txt form. The files can be imported as HDD, TDD or both and the results, that are either graphs or waveforms, can be exported as text or image files.

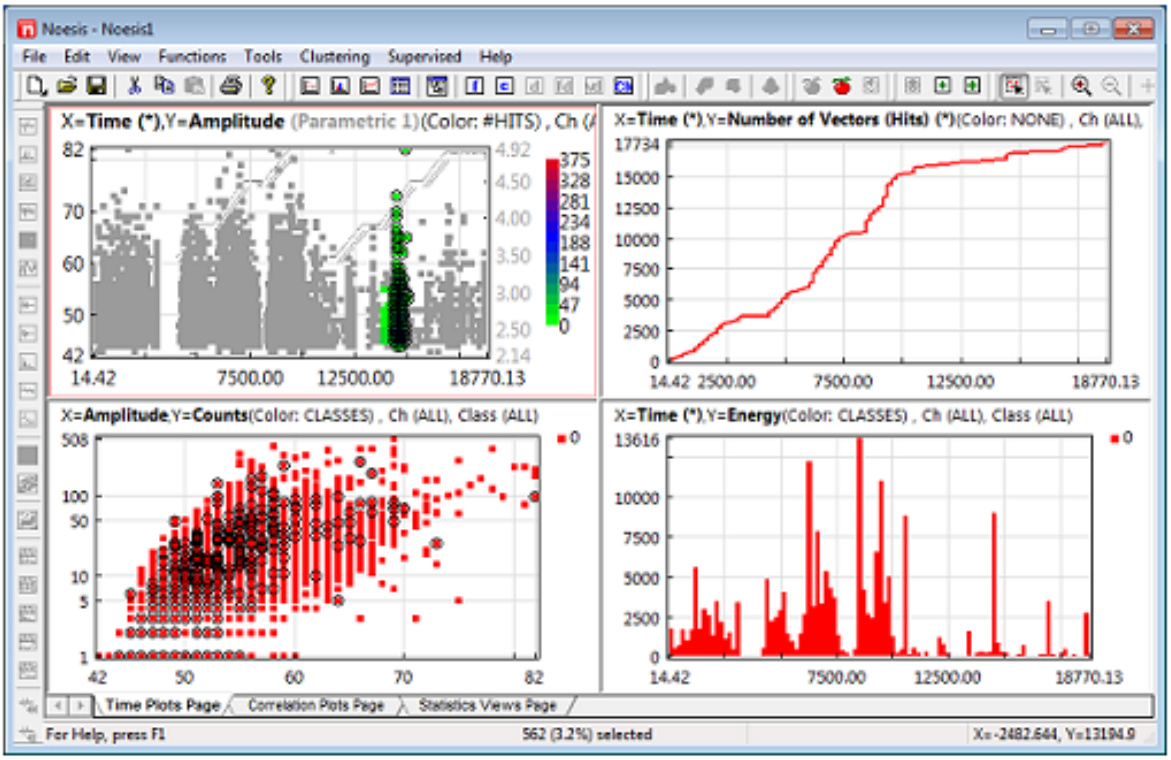

Figure 5.9: Typical Noesis screen where each view is a separate graph (Mistras, 2013).

5.2.6 Ac-conductivity measurements

Electrical conductivity measurements were carried out simultaneously with AE recordings by means of a separate unit which is dedicated for dielectric and electrical conductivity measurements in solid or liquid samples. Specifically, time-series of ac-conductivity were recorded with a high-resolution broadband spectrometer (Novocontrol Alpha-N Analyzer) which allows measurements over a wide frequency range of the applied ac electric field (10^{-2} – 10^{6} Hz). Proper electromagnetic shielding consisting of a Faraday cage with copper sheets was implemented to the whole apparatus, in order to diminish noise problems which are usually observed at low frequencies (50 Hz and higher

harmonics). A schematic representation of the experimental setup is illustrated in Figure 5.10.

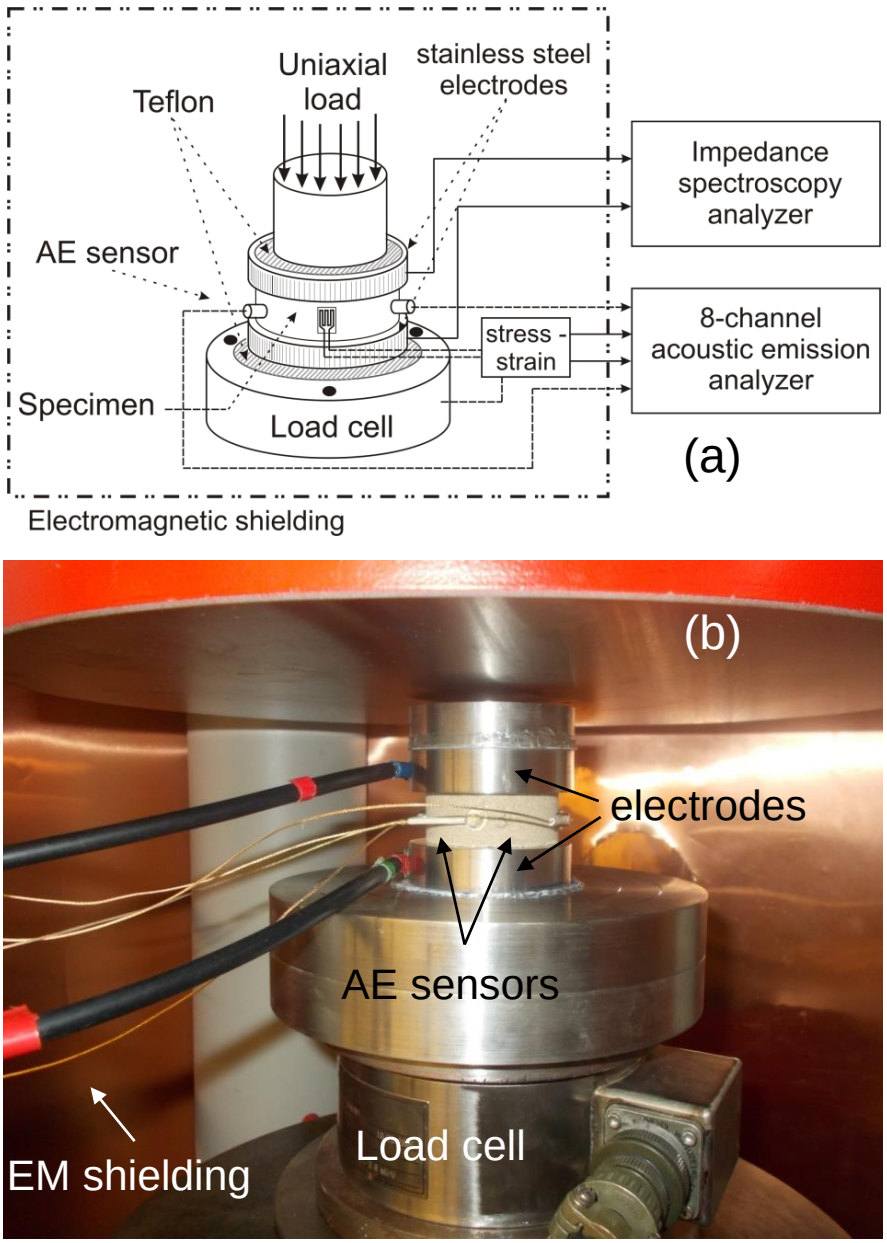

Figure 5.10: (a) Schematic representation of the experimental setup used for the simultaneous measurements of electrical conductivity and acoustic emissions during the uniaxial loading of sandstone samples (b) A cylindrical sandstone specimen inside the test apparatus.

5.3 Preparation Experiments of Cubic Specimens

5.3.1 Samples Preparation

Cubic samples of sandstone were subjected to uniaxial linear loading under displacement control. Eight piezoelectric sensors were initially placed on the lateral surfaces of the specimens. The specimens are sandstone “Tyliss” of cubic shape and dimensions 7x7x7cm, approximately. This material of high porosity is suitable for studying the effect of the water content to the fracture process and to possible correlations of AE activity with the variation of electrical conductivity. The exact dimensions of the three cubic specimens that were used are shown in Table 5.3. The specimens Cu1 and Cu2 were dried in an oven (Heraeus) at 105°C for 24 hours and afterwards they were remained in room conditions, in order to absorb water vapours from air. Specimen Cu3 was placed in a water chamber for one day to ensure full saturation with water.

In these three cubic specimens, only AE activity was recorded without performing ac-conductivity measurements. Conductivity measurements using the capacitor method require suitable specimen geometry, i.e. low height/diameter ratios which are not available in this case. However, with these preliminary measurements on the cubic specimens, we can investigate the mechanical properties as well as any possible influence of the water content to the measured AE activity.

Table 5.3: Dimensions of cubic samples.

Specimen	Dimension x (mm)	Dimension y (mm)	Dimension z (mm)
Cu1	70.3	70.2	72.5
Cu2	69.3	70.1	69.9
Cu3	69.4	70.3	70.2

5.3.2 Placement of sensors

Piezoelectric sensors were placed on the lateral surfaces of the specimens, two on each side. The non-symmetrical positions of the sensors are shown in Table 5.4. Strain gauges were placed on the specimens Cu1 (side B) and Cu3 (side A) for measuring the axial and transverse deformation.

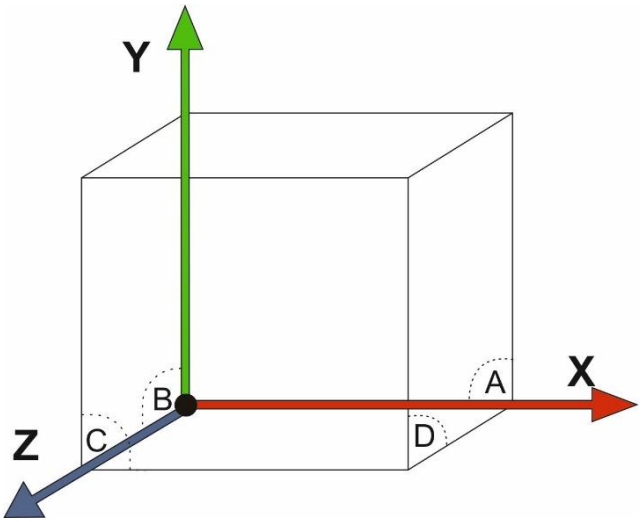

Figure 5.11: The coordinate system and sides of the cubic samples (A, B, C, D).

Table 5.4: Positions of sensors on samples surfaces.

sensor	Coordinate x (mm)			Coordinate y (mm)			Coordinate z (mm)			Side of Sample
	Cu1	Cu2	Cu3	Cu1	Cu2	Cu3	Cu1	Cu2	Cu3	
1	55.5	55.5	55.5	49	49	49	0	0	0	A
2	16	16	16	19	19	20	0	0	0	
3	0	0	0	47	47	47	18	18	18	B
4	0	0	0	18	18	20	62	59	59	
5	17	17	17	47	47	47	72.5	69.9	70.2	C
6	57	57	57	19	19	21	72.5	69.9	70.2	
7	70.3	69.3	69.4	44	44	44	58	58	58	D
8	70.3	69.3	69.4	25	25	25	18	18	18	

5.3.3 Samples loading

The testing machine MTS 815 was used for performing the linear uniaxial compression experiments on the 3 cubic sandstone specimens. Each specimen was placed on the centre of the load platform and a plate with thickness 15 mm was placed on the top and bottom of it. The specimens were loaded at a controlled loading rate (in displacement control) until they reached the failure point. The loading rate for specimen Cu1 was 0.005 mm/sec and for specimens Cu2, Cu3 was 0.0035 mm/sec. Figure 5.12 shows the specimens Cu1 and Cu3 placed on the test machine, before the test.

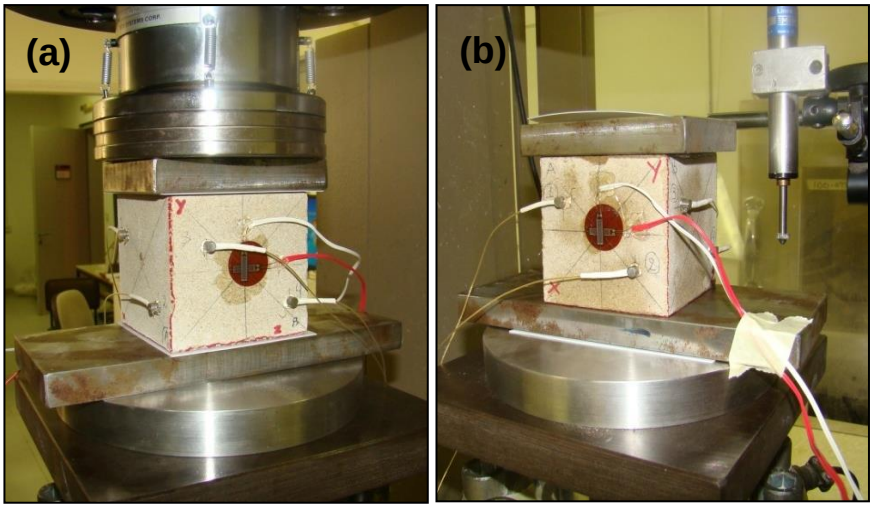

Figure 5.12: (a) The exposed to ambient moisture and (b) the water-saturated cubic specimens, before the compression tests.

5.4 Preparation Experiments of Prismatic Specimens

5.4.1 Samples Preparation

Two prismatic specimens (P1 and P2) with dimensions 3x7x7cm (see Table 5.5) were subjected to stepped and linear loading. Prior to the compression tests, both prismatic specimens were dried in an oven (Heraeus) at 105°C for 24 hours and then left in air for sufficiently long time to saturate in ambient humidity.

Table 5.5: Dimensions of prismatic samples.

Specimen	Dimension x (mm)	Dimension y (mm)	Dimension z (mm)
P1	32	70.1	70.2
P2	34.6	70.1	70.75

5.4.2 Placement of sensors

The placement procedure of the eight sensors is the same as previously with coordinates according to axes X, Y and Z, as shown in Table 5.6. It is important to mention the use of two stainless-steel electrodes for the measurement of the ac-conductivity at low (10 kHz) and high (200 kHz) frequencies. The electrodes were placed on the centre of sides B and D of the two specimens and the strain gauge on side A of specimen P2.

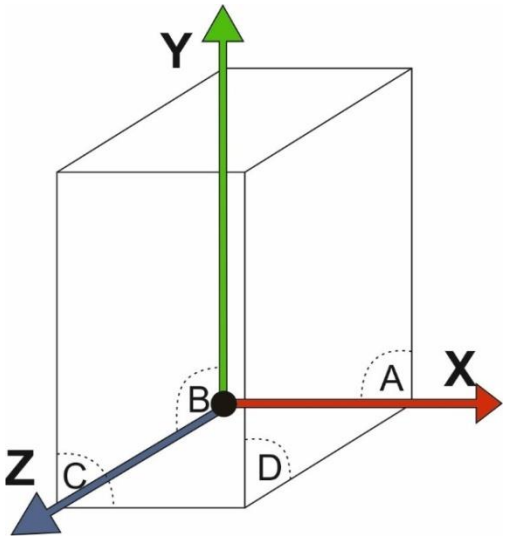

Figure 5.13: The coordinate system and sides of the prismatic samples (A, B, C, D).

Table 5.6: Locations of sensors on samples surfaces.

sensor	Coordinate x (mm)		Coordinate y (mm)		Coordinate z (mm)		Side of Sample
	P1	P2	P1	P2	P1	P2	
1	23	23	53	53	0	0	A
2	19	9	23	17	0	0	
3	0	0	60.5	60.5	10.5	10.5	B
4	0	0	21.3	21.3	60.5	60.5	
5	19.7	19.7	53.4	53.4	70.2	70.75	C
6	16.2	16.2	19.8	19.8	70.2	70.75	
7	32	34.6	52.8	52.8	60.5	60.5	D
8	32	34.6	11.8	11.8	16.8	16.8	

5.4.3 Samples Loading

In order to conduct the experiments of linear and stepped loading, the testing machine ALPHA3-3000 was used. Specimen P1 was subjected to linear loading, starting from 0 kN up to the ultimate failure at 130 kN, with steps of 10 kN. In linear uniaxial compression of the specimen P2 (loading rate, 0.3 kN/s in load control), the final rupture was achieved at 170kN. Figure 5.14 illustrates the specimen P1 inside the testing apparatus before the compression test takes place.

Figure 5.14: The prismatic sample inside the testing machine before the compression test.

5.5 Preparation of Cylindrical Sandstone specimens

5.5.1 Samples Preparation

Six specimens of cylindrical shape were subjected to three types of uniaxial loading, namely linear, stepped and saw-tooth. The dimensions of the cylindrical sandstone specimens, the type of loading and the degree of saturation are shown in Table 5.7. Specimens C1-C3 remained in ambient conditions for sufficiently long time (3-4 days) in order to be saturated with humid air. Specimens C4-C6 were saturated with water under vacuum conditions.

All the specimens were covered with transparent thin membrane to prevent any loss of water content in long-term experiments (refer to Fig. 5.15), as in the case of step loading. This intervention was deemed necessary because a small water loss in the water-saturated sandstone specimens may cause a large reduction in the measured electrical conductivity.

Table 5.7: Dimensions of cylindrical samples, type of loading and degree of saturation.

Specimen	Height, *h* (mm)	Diameter, *D* (mm)	Load	Saturation
C1	18.6	49	Step	in air
C2	20.9	49	linear	in air
C3	18.5	49	saw-tooth	in air
C4	18	49	linear	with water
C5	18.65	49	saw-tooth	with water
C6	19	49	step	with water

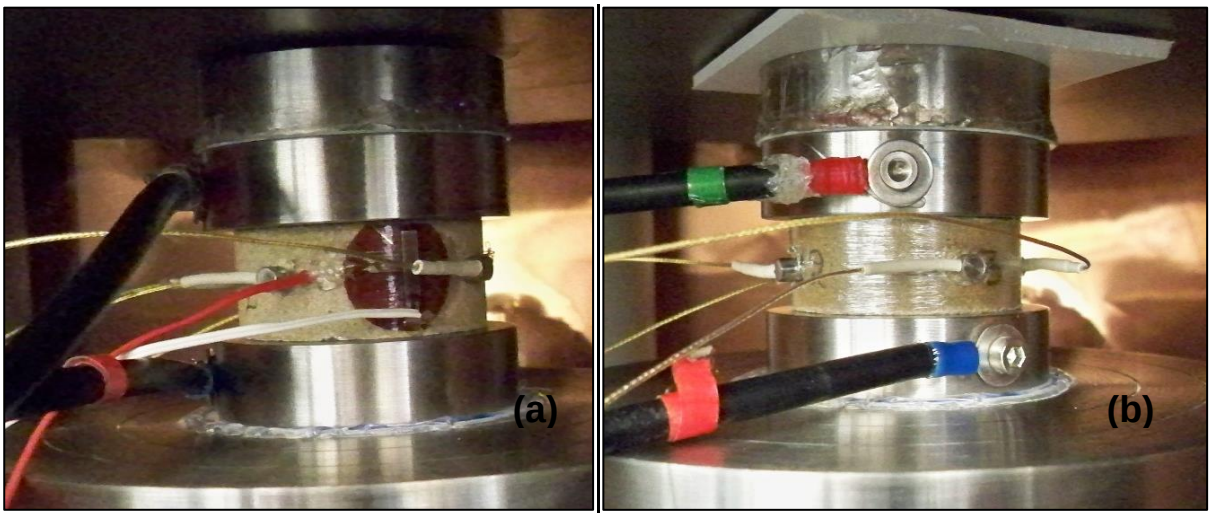

Figure 5.15: (a) The cylindrical sandstone specimen exposed to ambient moisture and (b) the water-saturated cylindrical specimen inside the testing machine.

5.5.2 Placement of sensors

Due to the relative small size of the cylindrical specimens, the piezoelectric transducers attached to the samples were limited to four. Their positions on the circumference of the specimens are illustrated in Figure 5.16, according to an X-Y coordinate system. The vertical position of the sensors, h^* was in the middle of the height of the specimens, $h^* = h/2$.

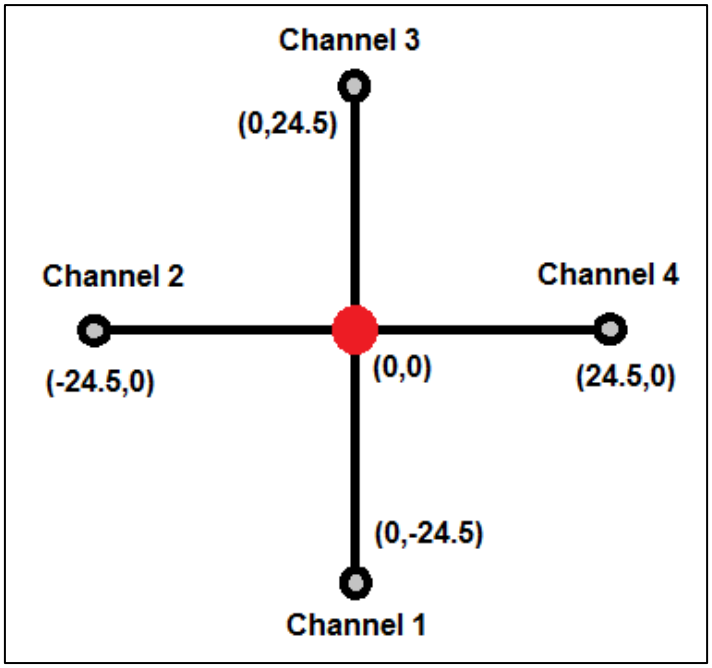

Figure 5.16: 2D planar location of piezoelectric sensors on cylindrical specimen.

5.5.3 Samples Loading

The ALPHA3-3000 testing machine was used to perform the uniaxial loading experiments in the 6 cylindrical sandstone specimens. Uniaxial loading was applied to the cylindrical specimens through the thick stainless steel electrodes (refer to Figure 5.15) that were used for measuring the electrical conductivity of the specimens. Thin Teflon plates were placed between the electrodes and the load platens to ensure electrical insulation of the specimens during the uniaxial loading tests and the measurement of the electrical conductivity (refer to Figure 5.15).

Chapter 6: Experimental Results and Discussion

6.1 Prismatic specimens

6.1.1 Analysis of AE parameters and ac-conductivity measurements

Two prismatic sandstone specimens, namely P1 and P2, were subjected to step and linear loading correspondingly, with simultaneous measurement of the AE activity and the ac-conductivity, in a direction perpendicular to the applied stress (refer to Fig. 5.14). In both experiments, the specimens were partially saturated with water vapours, by remaining in ambient humidity for sufficient long time to reach equilibrium.

Preliminary conductivity measurements in dried sandstone samples showed that the ac-conductivity is strongly affected from the adsorption of air humidity in the highly porous matrix of specimens. Thus, it would be impossible to investigate any variation of ac-conductivity due to the formation and propagation of cracks in specimens subjected to compressional loading, unless the specimens were in equilibrium with the humid environment.

The time evolution of the AE parameters for specimen P1, namely amplitude, hit rate, cumulative hits and risetime, are shown in Fig. 6.1(a-d). Starting from 5 kN which was the applied force of the initial contact between the loading platen and the prismatic specimen, the load was increasing by ~10 kN in each step which last for around 1000 s. This time interval was necessary for the specimen to relax after the application of each load step and measure afterwards the corresponding conductivity without any substantial AE activity. This relaxation is better indicated in Fig. 6.1(b) where the hit rate follows an abrupt decrease after the initial application of each load step.

It should be mentioned that, in step loading experiments, the ac-conductivity was measured over a wide frequency range (10^{-2} – 10^{6} Hz) in each step by means of complex impedance spectroscopy (Saltas *et al*., 2014). However, in the present study, only conductivity data at selected frequencies (0.01 and 1Hz, 10 and 200 kHz) have been considered for their correlation with the AE data. The choice of the measured frequencies

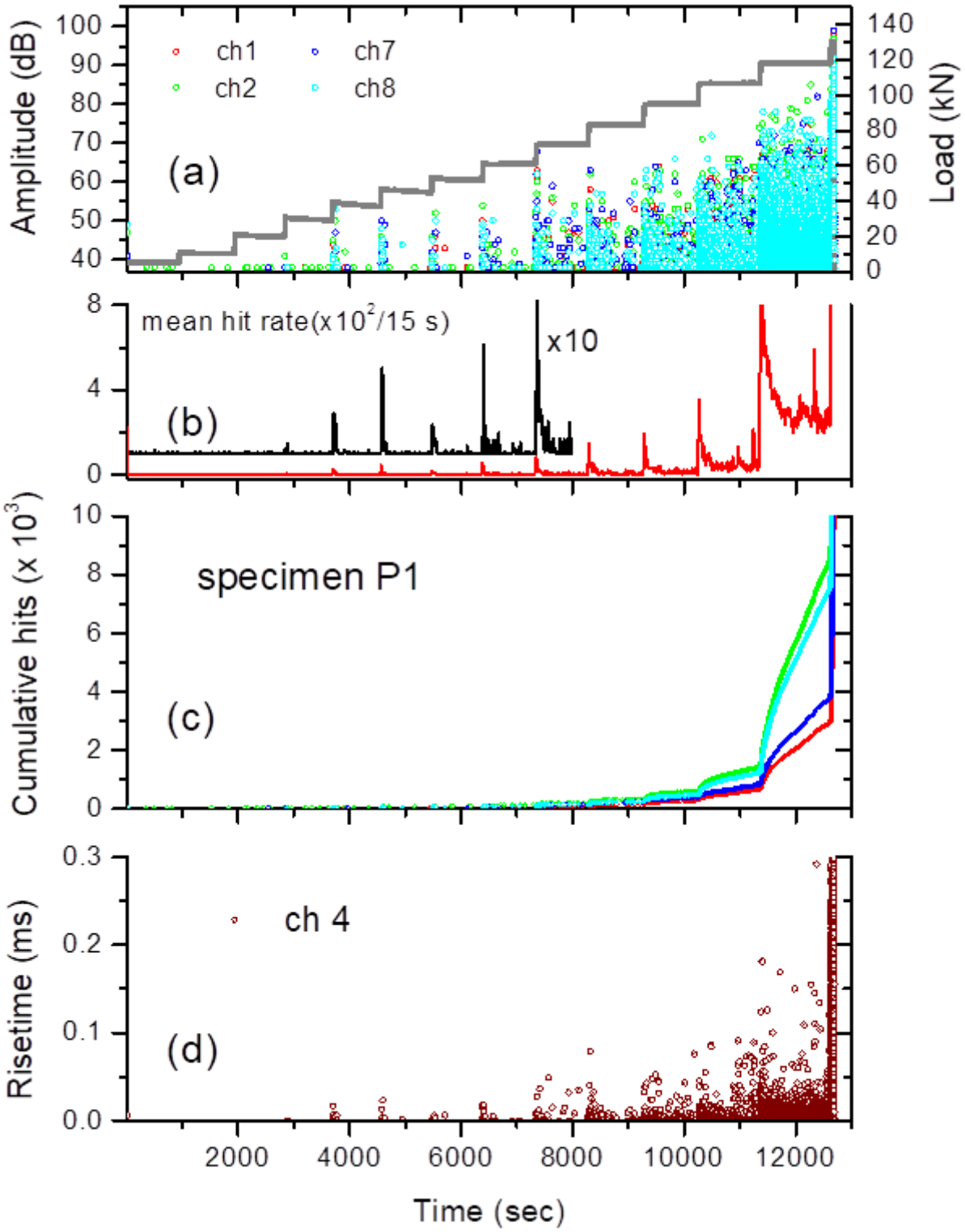

Figure 6.1: Time evolution of AE parameters during the uniaxial compression of the sandstone specimen P1. (a) The amplitudes of selected channels (1, 2, 7 and 8) and the applied load, (b) the mean hit rate of all channels, (c) the cumulative hits of channels 1, 2, 7 and 8 and (d) the risetime of channel 4. The final rupture of the specimen occurs at t=12600 s, as indicated from the corresponding drop of the load. Note that in (b), the mean hit rate is also shown magnified by a factor of 10, until the time 8000 s.

was based on the conductivity spectra which exhibited strong dispersion in the low frequency region.

During the sequential loading of the specimen P1, acoustic emissions of low amplitudes (<55 dB) are recorded from the first steps, up to 60 kN which corresponds to about half of the failure load. From 70 kN to 100 kN, AE activity of higher hit rate and higher amplitudes (<70 dB) is recorded, while during the two final loading steps (110 and 120 kN) a continuous high hit rate of high amplitudes forebodes the failure of the specimen. The majority of the hits are recorded during these two last loading steps, as it is evident from the cumulative distribution of hits [Fig. 6.1(c)]. The attempt to increase further the load to 130 kN led to the ultimate rupture of the specimen.

An important AE parameter is the risetime which is able to discriminate different fracture modes, i.e. tensile, shear or mixed mode cracking (Aggelis, 2011; Aggelis *et al*., 2013). The time evolution of RT of hits recorded in channel 4 during the sequential compression of specimen P1 is depicted in Fig. 6.1(d). Low values of RT (~50 μs) are observed for load up to 70 kN, while afterwards RT increases, reaching values of ~200 μs, before the ultimate failure of the specimen. The situation is quite similar for the other channels, as it is shown in Fig. 6.2. During the last two steps (110 and 120 kN), RT almost doubles with respect to the previous stage of load (60 – 100 kN), while during the final failure of the specimen, RT increases to high values reaching the upper limit of the setup value (10 ms). These large values correspond to continuous acoustic emission due to successive micro-cracks and/or friction between generated fragments.

The values of ac-conductivity in each loading step of specimen P1 are shown at two distinct frequencies (0.01 and 1 Hz) in Fig. 6.3. The measured conductivity at 0.01 Hz can be actually considered as the dc-conductivity of sandstone. Dc-conductivity of dried sandstone has been measured to be about 2-3 orders of magnitude lower (10^{-9} S/cm) than that measured in specimen P1 which was saturated in air humidity. During the applied step loading, conductivity in both measured frequencies decreases in each step, up to the load of 30 or 50 kN, at 1 Hz and 0.01 Hz, respectively. After the load of 30 kN, the measured conductivity at 1Hz decreases slightly, while the conductivity at 0.01 Hz (after 50 kN)

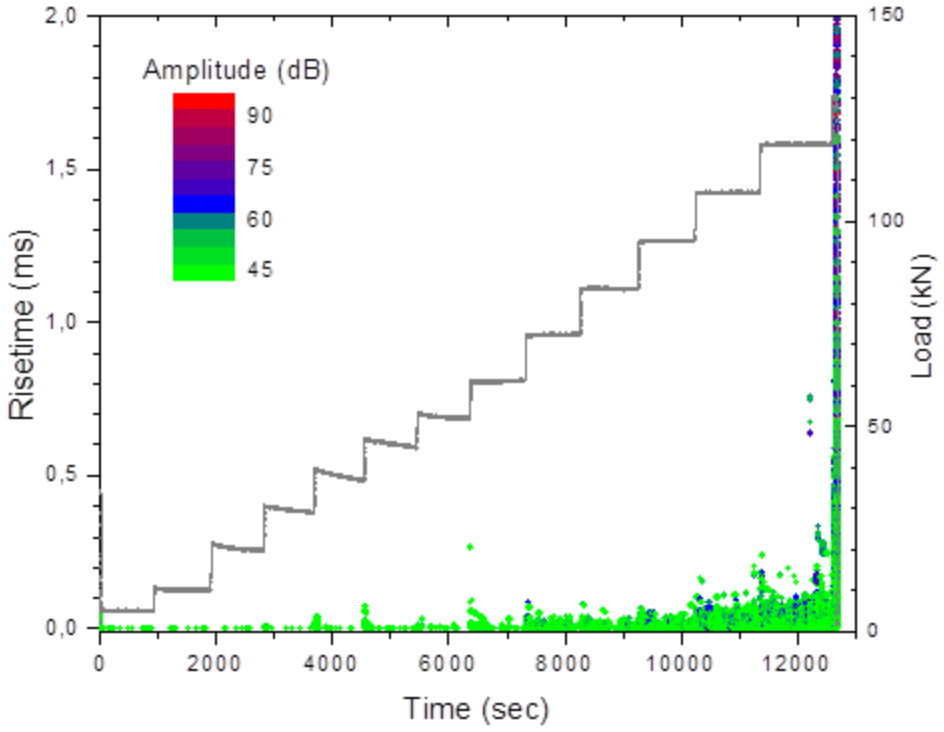

Figure 6.2: Time-series of the risetime of recorded hits from all channels during the uniaxial compression of the sandstone sample P1. The applied load is also shown.

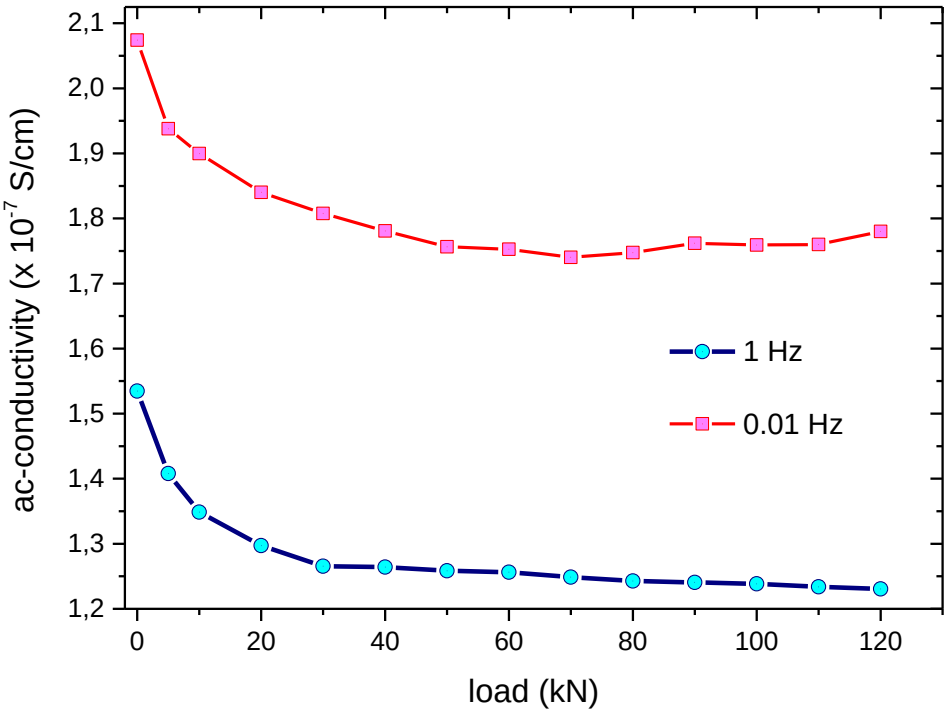

Figure 6.3: Ac-conductivity as a function of frequency during the stepped uniaxial compression of the sandstone sample P1. The inset demonstrates the ac-conductivity as a function of the applied load.

exhibits rather small fluctuations. In both cases, there is no clear indication in the conductivity values of the failure of the sandstone specimen that appears by increasing the load.

A parameter that has not been extensively exploited in studying fracture processes in brittle materials by means of acoustic emissions is the inter-event time, which is defined as the time difference between two successive events. The inter-event times of the recorded hits in channel 2, during the sequential loading of specimen P1 is shown in Fig. 6.4, as a function of the successive hits. The situation is similar for the rest of the channels. By visual inspection, it is obvious that the majority of the hits that are related to the generation of micro-cracks is observed during the last two loading steps. Interestingly, the inter-event times range from hundreds of seconds at the initial loading steps,

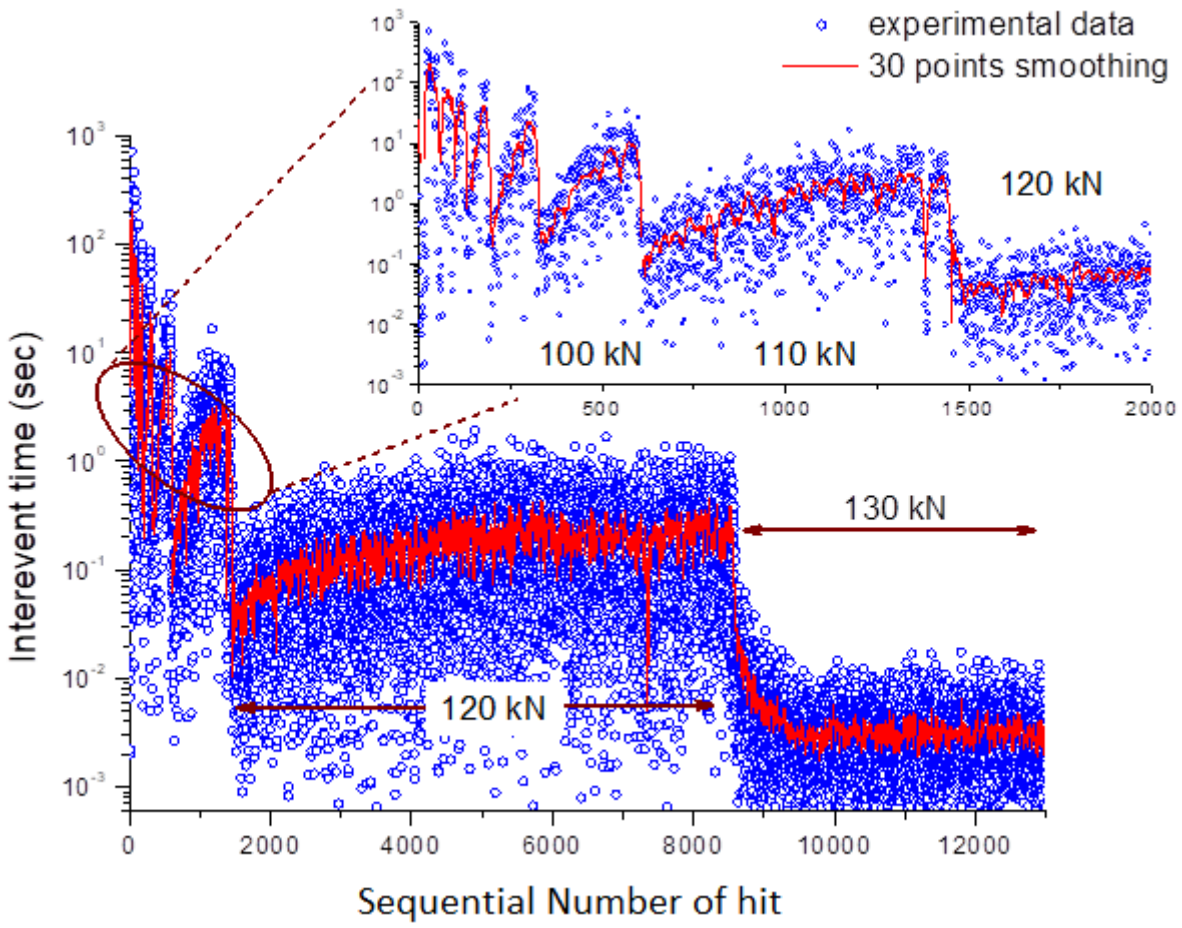

Figure 6.4: Inter-event times of recorded hits in channel 2 of the sandstone sample P1, during the step loading, up to the ultimate failure. Note the logarithmic scale in y-axis.

down to a few ms during the failure stage. At the start of each loading step where the load is applied, we observe a rapid decrease of inter-event times more than an order of magnitude, due to the generation of micro-cracks inside the sandstone specimen. Subsequently, during the loading step, the hit rate gradually decreases (refer to Fig. 6.1(b)) and thus, the inter-event time increases and tend to stabilize at a certain value, until the next loading step. However, this value is always lower in each successive loading step. This observation could be served as an indication of the upcoming failure of a brittle material subjected to repeated mechanical stress.

The 2nd prismatic specimen (P2) was subjected to linear loading with a loading rate of 300 N/s, up to fracture. The AE parameters, i.e., amplitude, mean hit rate, cumulative hits and RT are shown in Fig. 6.5. The duration of the loading experiment was approximately 510 s. From the initial stage of loading, acoustic emissions of low amplitudes are observed (< 50 dB), while after the time t=400 s and for a duration of about 100 s, events with constantly increasing amplitudes are recorded. The accelerated hit rate that is recorded afterwards is evidence of the upcoming failure of the sandstone specimen. In this time range, RT increases continuously with values reaching the setup limit [refer to Fig 6.5(d)]. As regard the cumulative distribution of the hits, the behaviour is quite similar for all the recording channels, as it is shown in Fig. 6.5(c).

The measured ac-conductivity of specimen P2 at two selected frequencies (10 kHz and 200 kHz) is depicted in Fig. 6.6. We observe that the shape of the curve is similar in both cases, although the absolute value of ac-conductivity at 200 kHz is about double than that measured at 10 kHz. The abrupt decrease of conductivity before 560 s is associated with the final rupture of the specimen. The correlation of ac-conductivity at 10 kHz with an AE parameter (RT) and the strain of the specimen P2 is shown in Fig. 6.7. At the initial stage of the loading, the non-linear behaviour of strain with time is attributed to the closure of micro-pores inside the porous sandstone specimen. Subsequently, ac-conductivity varies almost linear with time, up to the moment (~380 s) which corresponds to ~70 % of the fracturing load. The departure from linearity of ac-conductivity starts inside the elastic response of the sandstone specimen (~85 %), as it is indicated from the corresponding strain variation (see the strain curve in Fig. 6.7).

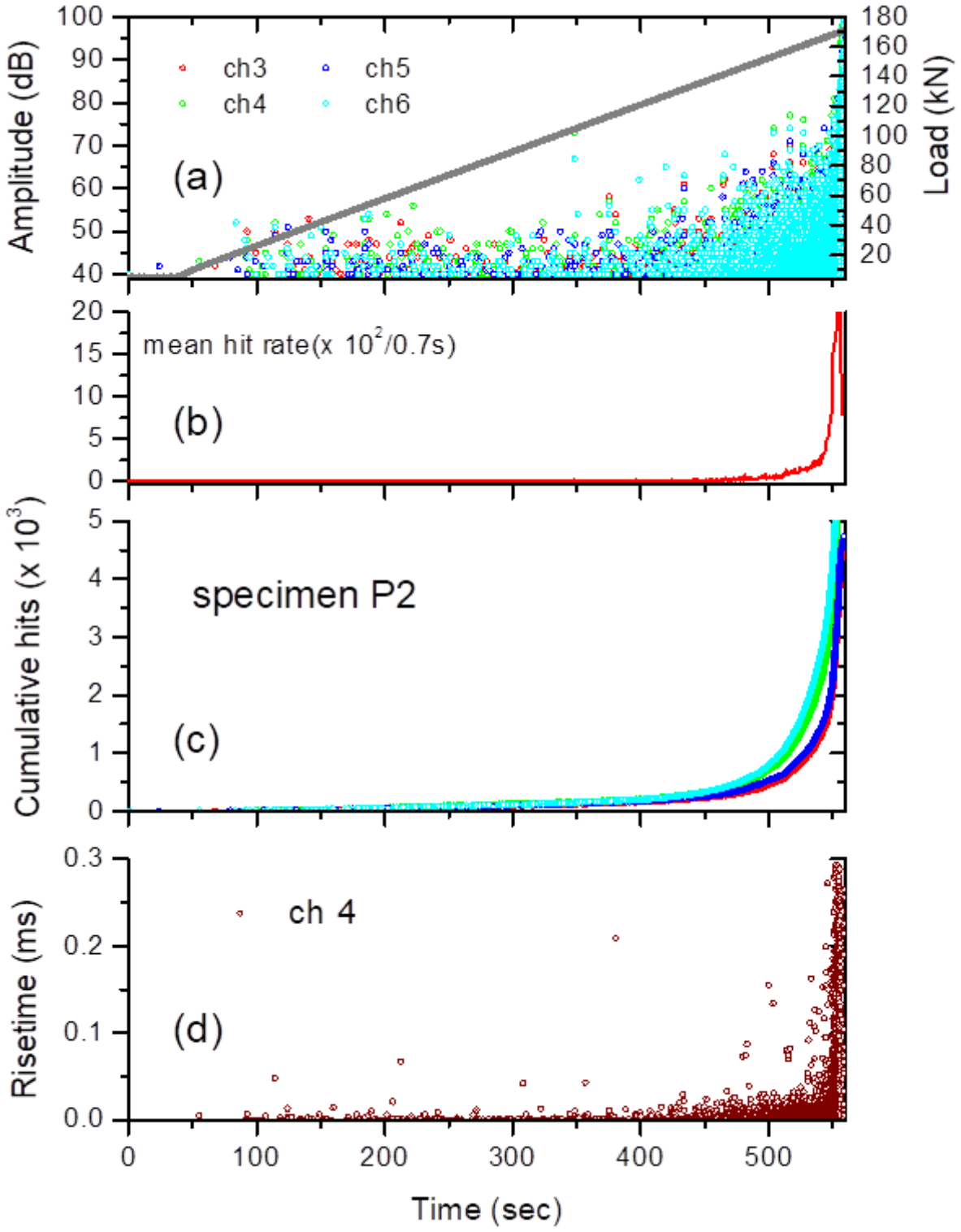

Figure 6.5: Time evolution of AE parameters during the uniaxial compression of the sandstone sample P2. (a) The amplitudes of selected channels (3, 4, 5 and 6) and the applied load, (b) the mean hit rate of all channels, (c) the cumulative hits of channels 3, 4, 5 and 6 and (d) the risetime of channel 4. The final rupture of the specimen occurs at t=560 s, as indicated from the corresponding drop of the load.

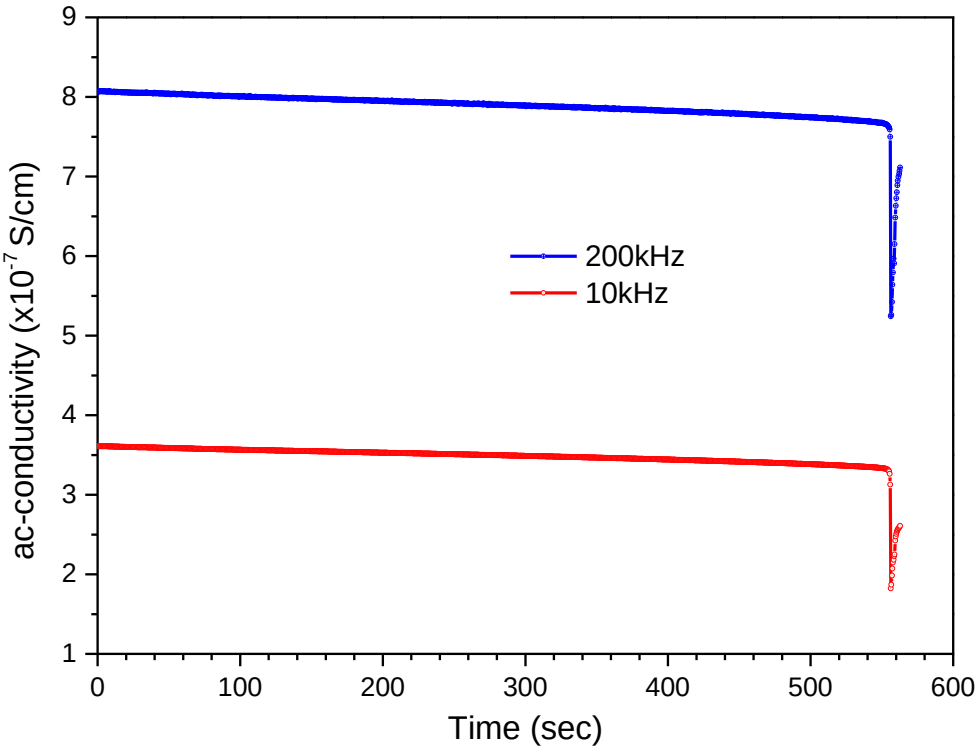

Figure 6.6: Time-series of ac-conductivity at 10 kHz and 200 kHz of the sandstone specimen P2. The final rupture of the specimen occurs at t=560 s according to the rapid decrease of the measured conductivity.

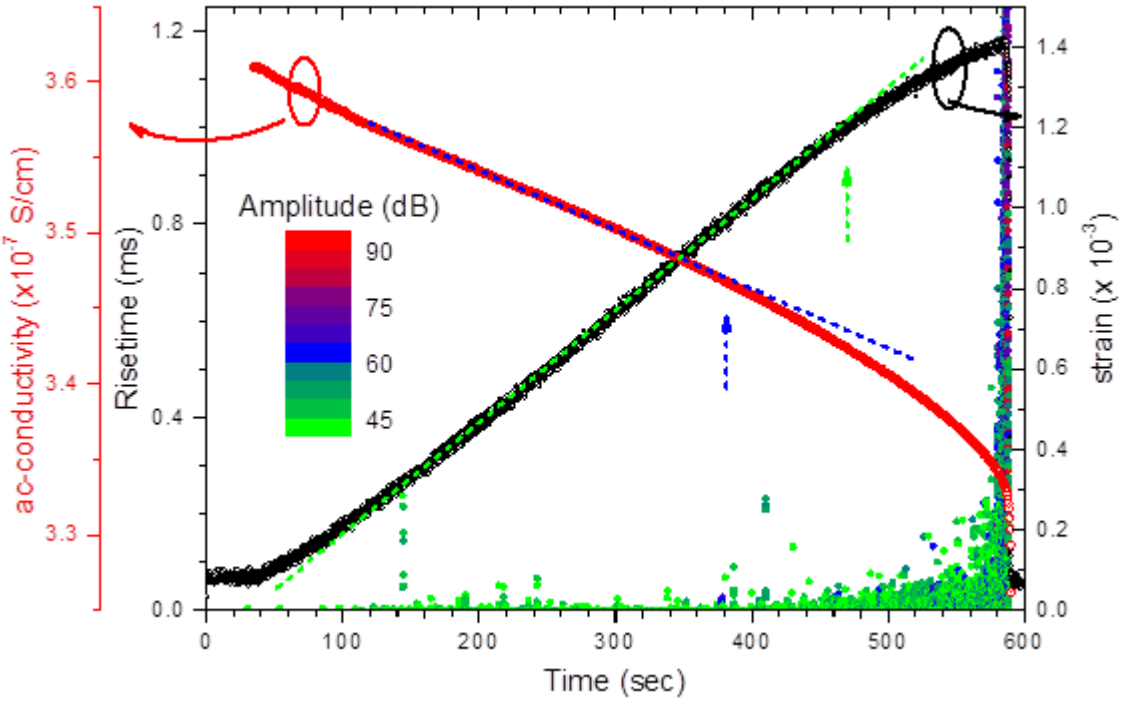

Figure 6.7: Time-series of risetime of recorded hits, deformation and ac-conductivity at 10 kHz during the uniaxial compression of the sandstone specimen P2.

The inter-event times as a function of the successive hits, during the linear uniaxial loading of specimen P2 are presented in Fig. 6.8. The variation of inter-event times covers more than 4 orders of magnitude (ms up to 10 s) with a very broad scattering. A 30-point smoothing of data reveals three distinct regions. The first region corresponds to the longer duration of the experiment (t~500 s) where only a small fraction of hits are recorded [~500 hits, refer to Fig. 6.5(c)] and the inter-event time decreases to ~0.1 s. During the subsequent accelerated generation of micro-cracks, inter-event time decreases further but seems to be stabilized before the fracture of the specimen. However, a sudden increase of inter-event time is observed for a few hundred of hits just before the failure. Due to the high hit rate that is observed at the failure point (indicated by the blue arrow in Fig. 6.8), inter-event time takes a certain value (10^{-2} s) that is limited from the settings of the experimental setup.

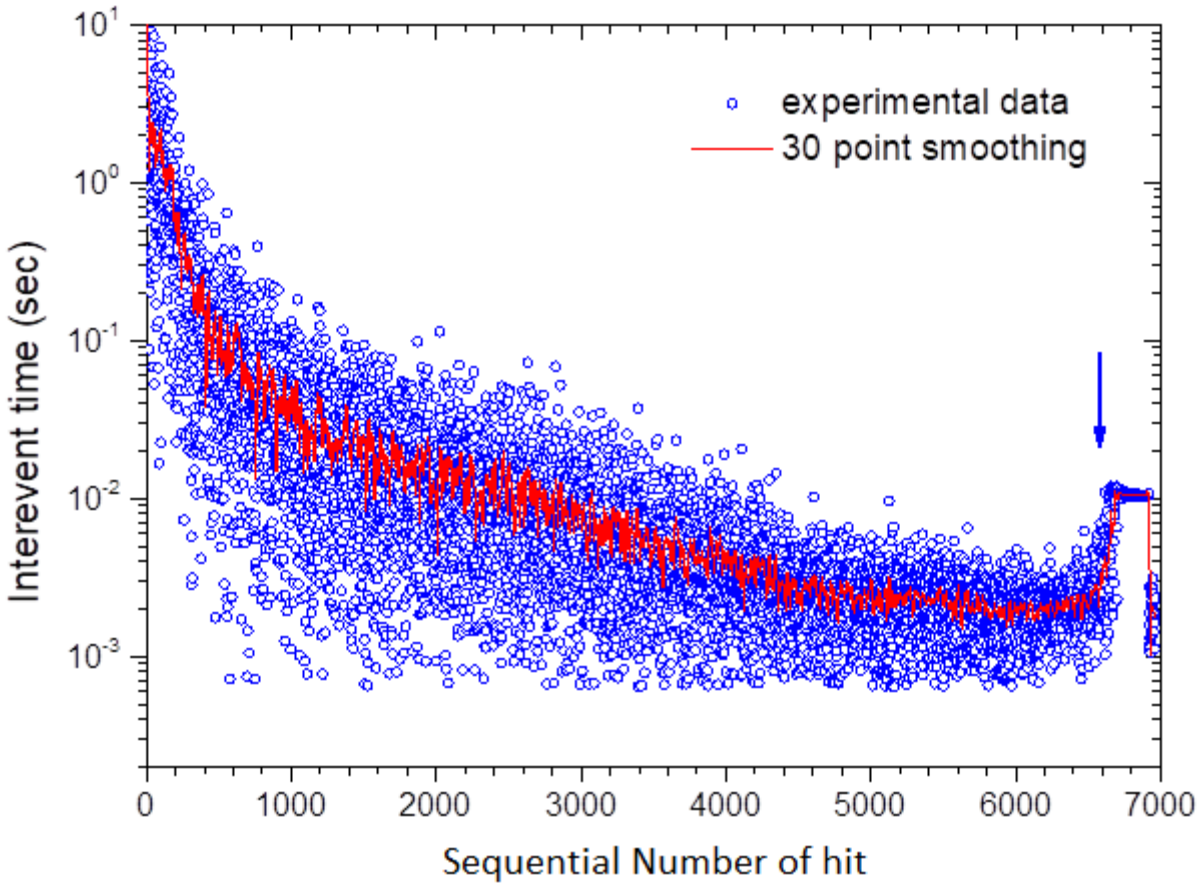

Figure 6.8: Inter-event times of recorded hits in channel 6 during the uniaxial loading of the sandstone specimen P2. The red line represents the smoothing of the data. The fracture of the specimen is indicated with the blue arrow.

6.1.2 Location of events

The velocity of the acoustic waves in the prismatic sandstone specimens was determined using 2 acoustic sensors in pulse-receive mode, placed in opposite positions on the side surfaces of the specimen. The estimated wave velocity was found to be (3300 ± 20) m/s. This value was used for calculating the 3D location of the AE events, during the uniaxial loading of the prismatic and cubic sandstone specimens.

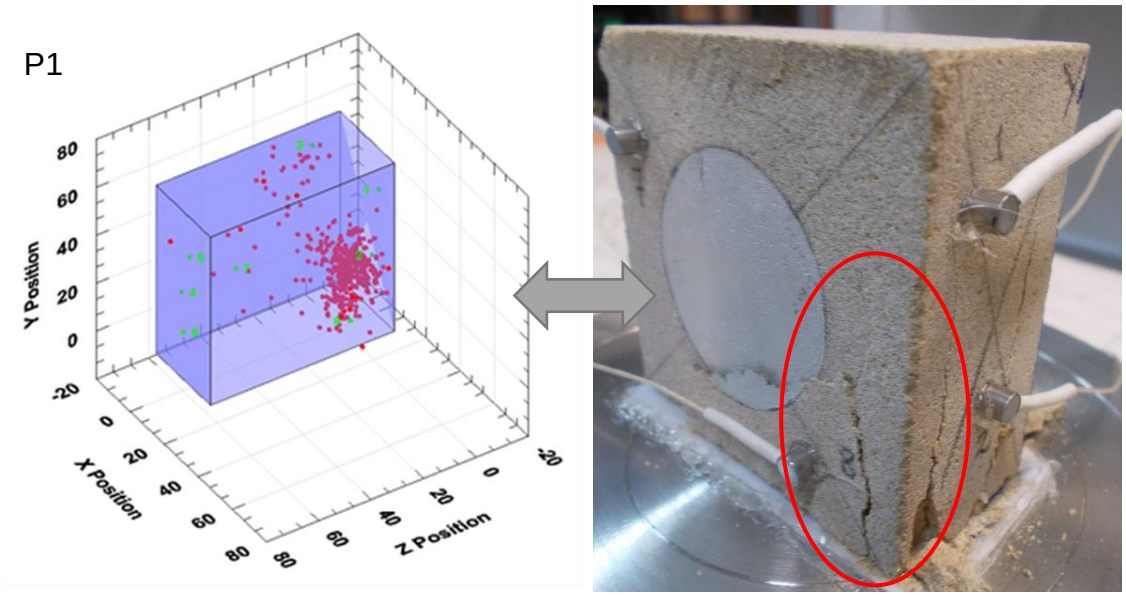

(a)

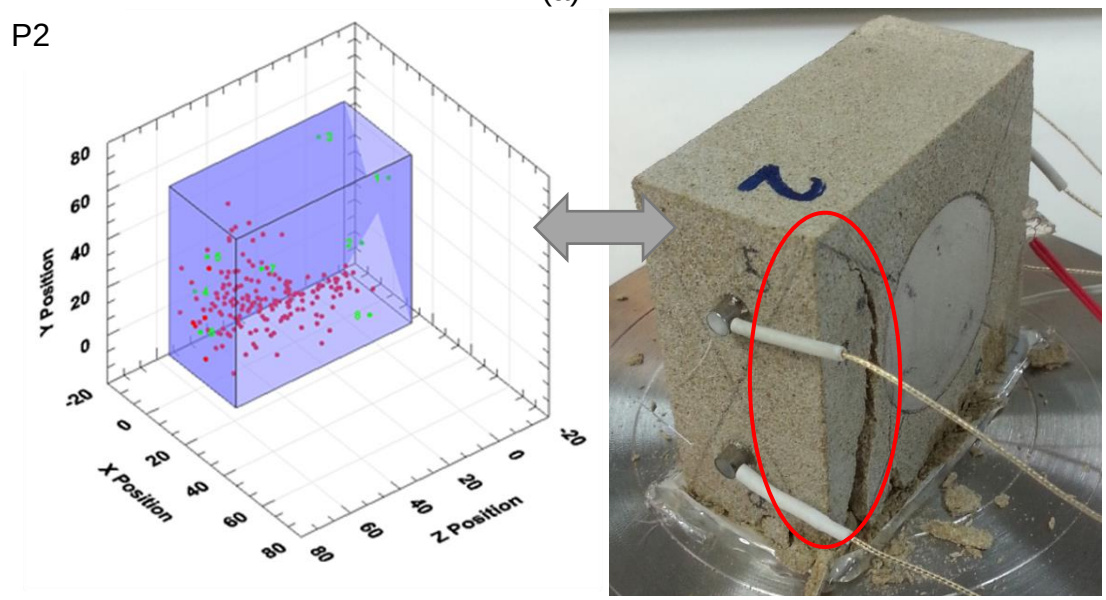

(b)

Figure 6.9: 3D location of events where amplitude filters have been applied and the corresponding photos, after the loading of specimens (a) P1 and (b) P2. The number of events are 1271 and 468 for specimen P1 and P2, respectively.

The 3D location of events for the two prismatic specimens (P1 and P2), are presented in Fig. 6.9. In order to exclude events of low amplitudes which might be resulted to inaccurate locations, an amplitude filter was used during the location procedure which rejected the events with amplitude <60 dB for sample P1 and the events with amplitude <55 dB for sample P2. These settings were useful to observe the regions with the most significant cracks. The results of location are in good agreement with the view of the fractured specimens, as it is shown in Fig. 6.9.

6.2 Cylindrical specimens

6.2.1 Analysis of AE parameters and ac-conductivity measurements

In the case of the uniaxial loading of the cylindrical sandstone specimens, only 4 sensors were used to detect the AE activity, due to the limited available surface area of the specimens (refer to Fig. 5.15). Six specimens were saturated with water or with water vapours in ambient conditions and were subjected to three different types of loading, i.e. stepped-like, linear and saw-tooth.

The time evolution of the AE parameters during the stepped-like uniaxial loading of specimen C1 (exposed to ambient moisture) is depicted in Figs. 6.10 and 6.11. The failure load is 140 kN (18.6 MPa). Unlike the prismatic specimens, considerable AE activity of high amplitudes (≤ 80 dB) is observed from the initial loading step up to 80 kN [Fig. 6.10(a)]. From the next loading step to the load of 120 kN, the hit rate increases in each step without observing however hits of different characteristics, i.e. higher amplitudes or risetimes [refer to Figs. 6.10(c) and 6.11]. During the loading step of 130 kN, the specimen suffers considerable damage as it is evident from the continuously increasing number of recorded hits [refer to Fig. 6.10(c)]. At this loading step, the risetime also increases, as it is indicated in Figs. 6.10(d) and 6.11. During the application of the next loading step (140 kN) the acoustic emissions are increasing at an accelerated rate and the specimen finally collapse.

The ac-conductivity values at two distinct frequencies (0.01 and 1 Hz) in each loading step of specimen C1 are shown in Fig. 6.12. Apart from the initial drop of the conductivity values, the two curves exhibit rather different behaviour after 80 kN,

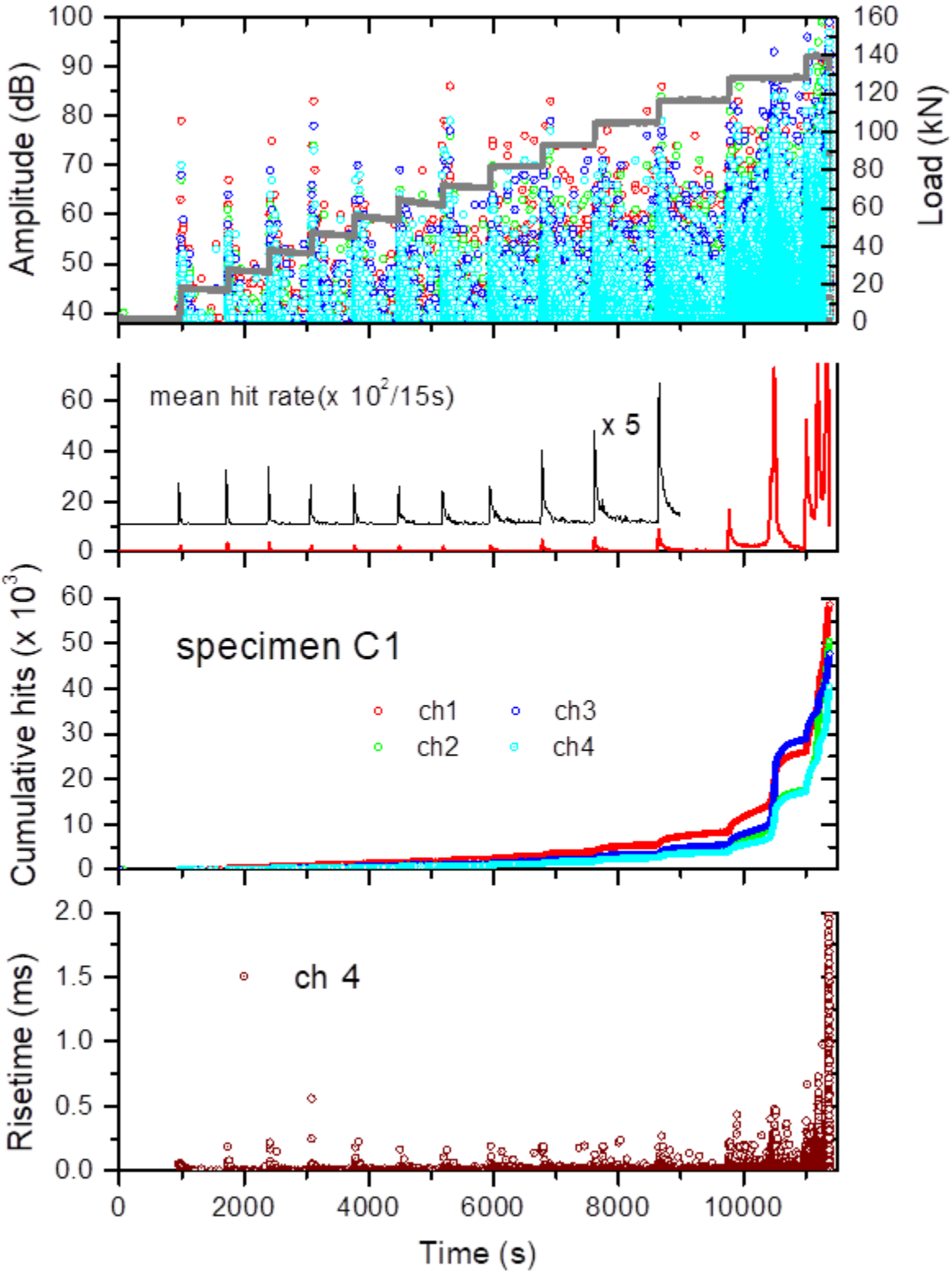

Figure 6.10: Time evolution of AE parameters during the uniaxial compression of the sandstone specimen C1. (a) The amplitudes of all channels (1, 2, 3 and 4) and the applied load, (b) the mean hit rate of all channels, (c) the cumulative hits of all channels and (d) the risetime of channel 4. The final rupture of the specimen occurs at t=11300 s, as indicated from the corresponding drop of the load.

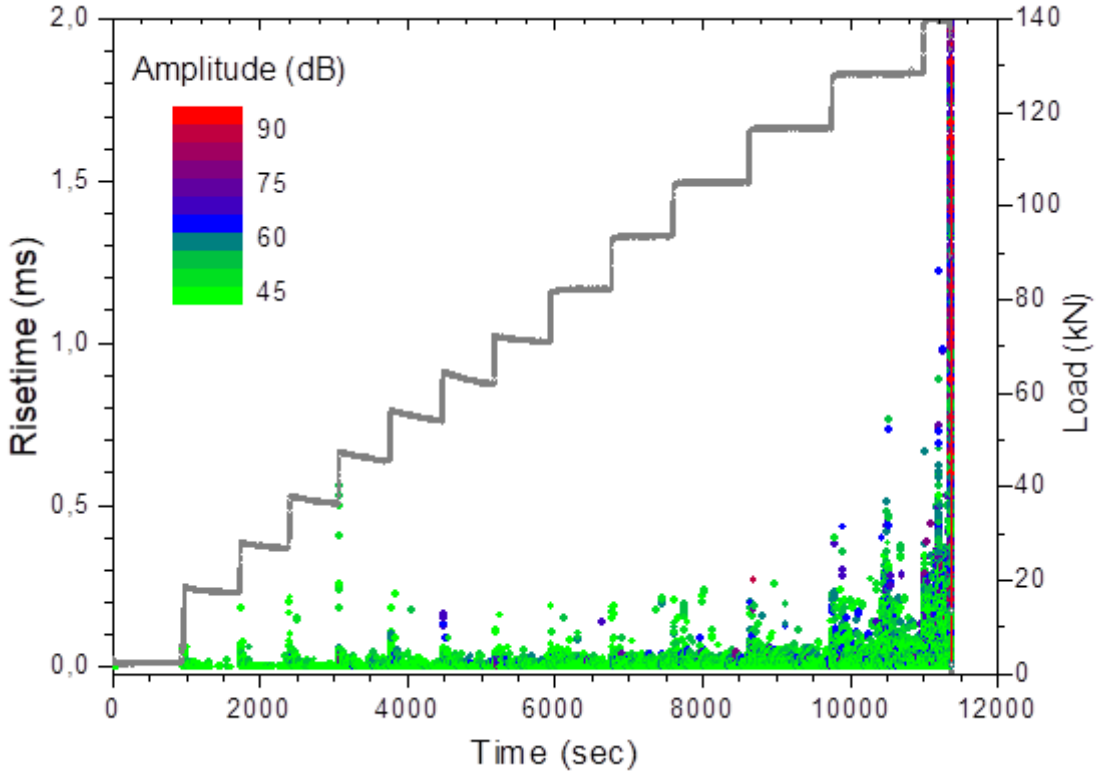

Figure 6.11: Time-series of risetime of recorded hits and applied load during the uniaxial compression of the sandstone sample C1.

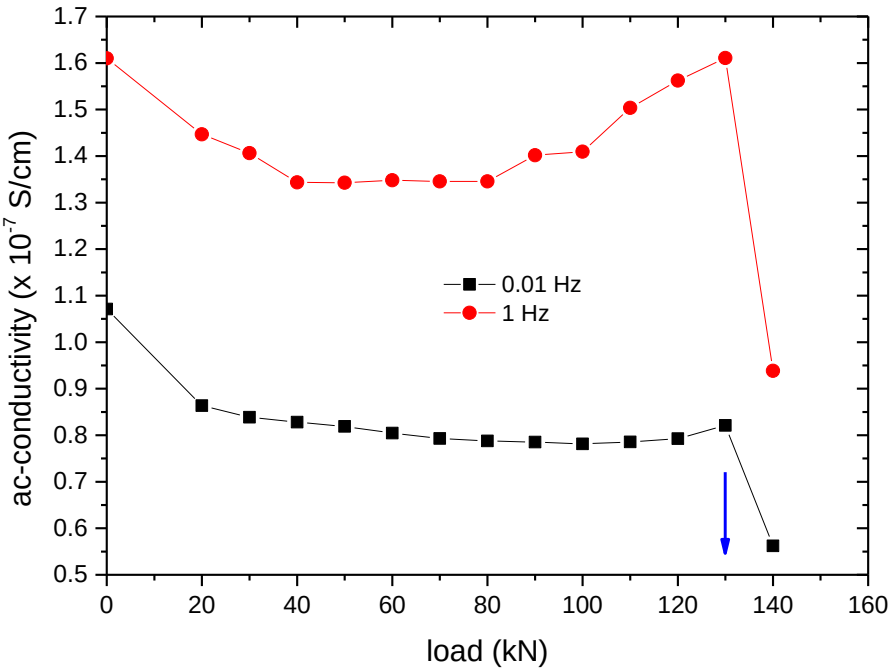

Figure 6.12: Ac-conductivity at two selected frequencies during the stepped uniaxial compression of the sandstone specimen C1.

where according to the aforementioned observations, the AE activity increases considerably. Ac-conductivity at 1 Hz increases again after 80 kN, reaching the initial value (~1.6x10^{-7} S/cm) at the final stage of rupture, i.e. at 130 kN. On the contrary, dc-conductivity (0.01Hz) after the load of 80 kN remains almost constant, up to the final rupture. This different behaviour is attributed to the spectral characteristics of the measured ac-conductivity.

The inter-event times during the uniaxial compression of specimen C1 are depicted in Fig. 6.13. The values of inter-event time exhibit wide dispersion covering almost 5 orders of magnitude. At each loading step, inter-event time decreases sharply at the time of loading and then, increases smoothly until the next loading step, reaching however a value smaller than that of the previous step. As in the case of the prismatic specimen P1, the majority of the hits are observed at the final steps of loading but in the present case, we do not observe a significant decrease of inter-event time values, indicative of the upcoming failure.

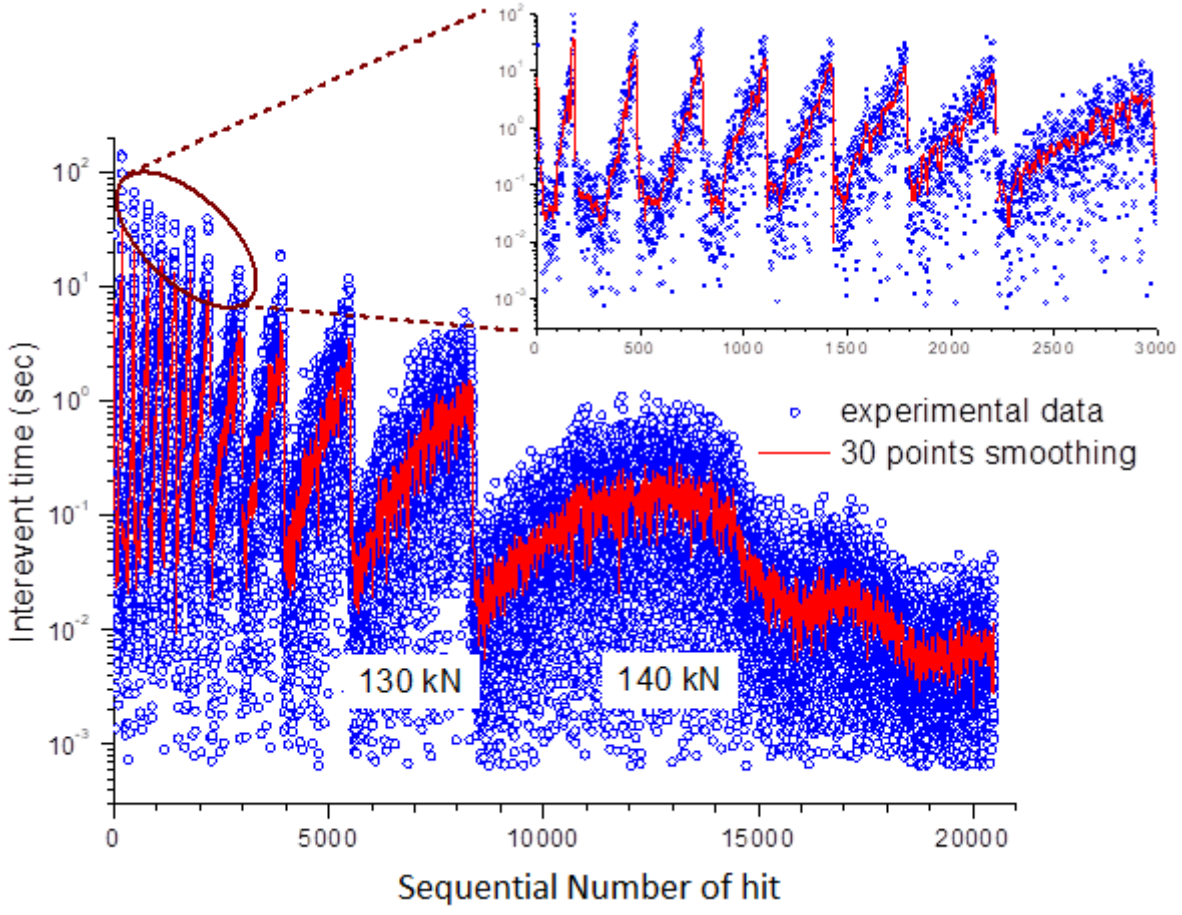

Figure 6.13: Inter-event times of recorded hits in channel 2 of the cylindrical sandstone specimen C1.

The time evolution of AE parameters and ac-conductivity measurements during the uniaxial linear loading of specimen C2 is depicted in Figs. 6.14 – 6.17. The loading rate was the same with the prismatic specimen, i.e. 300 N/s. The total duration of the experiment was approximately 300 s. We observe that the specimen collapses to the force of 100 kN. However, significant damage of the specimen occurs at lower stress (80 kN or 13.3 MPa), as it is evident from the evolution of the mean hit rate and the risetime [refer to Fig. 6.14(b), (d)]. Hits of a low rate but of high amplitudes are observed from the initial stage of loading for duration of ~100 s. Subsequently, the hit rate rises smoothly up to the time of 240 s where it increases sharply, due to the upcoming fracture at the time of ~260 s. However, as the stress is further applied to the specimen, the AE activity is further recorded, up to the time of 330 s, where the specimen finally collapsed. The prolonged application of the pressure in the sample is due to its low height, which can lead to extensive damage in certain areas and to the final collapse at a later time. This has also led in some experiments to the detachment of some AE sensors from the surface of the sample prior to the ultimate failure and thus to the misleading detection of AE events. Thus, the post-peak region [refer to Fig. 6.14(b)] should not be taken into consideration for the proper evaluation of the AE parameters.

Ac-conductivity in both measured frequencies (Fig. 6.15) decreases slowly with increasing linear loading. Both time-series on the two measured frequencies exhibit the same characteristics. After the initial failure of the specimen at 80 kN (Fig. 6.16), conductivity decreases further. However, since the main planes of cracks of the specimens are parallel to the applied load, the specimen may lose its consistency but many conduction paths remain unchanged in that direction. As a result, the conductivity decreases but not as much as would be expected if the shear surface was along the specimen.

The correlation of ac-conductivity and a representative AE parameter (risetime) is shown in Fig. 6.16. We clearly observe that significant changes in conductivity are related to the deformation of the specimen which is reflected in the recordings of acoustic emission parameters.

Finally, with regard to the inter-event times recorded in channel 3 (refer to Fig. 6.17) during the linear loading of specimen C2, we observe fluctuations of more than

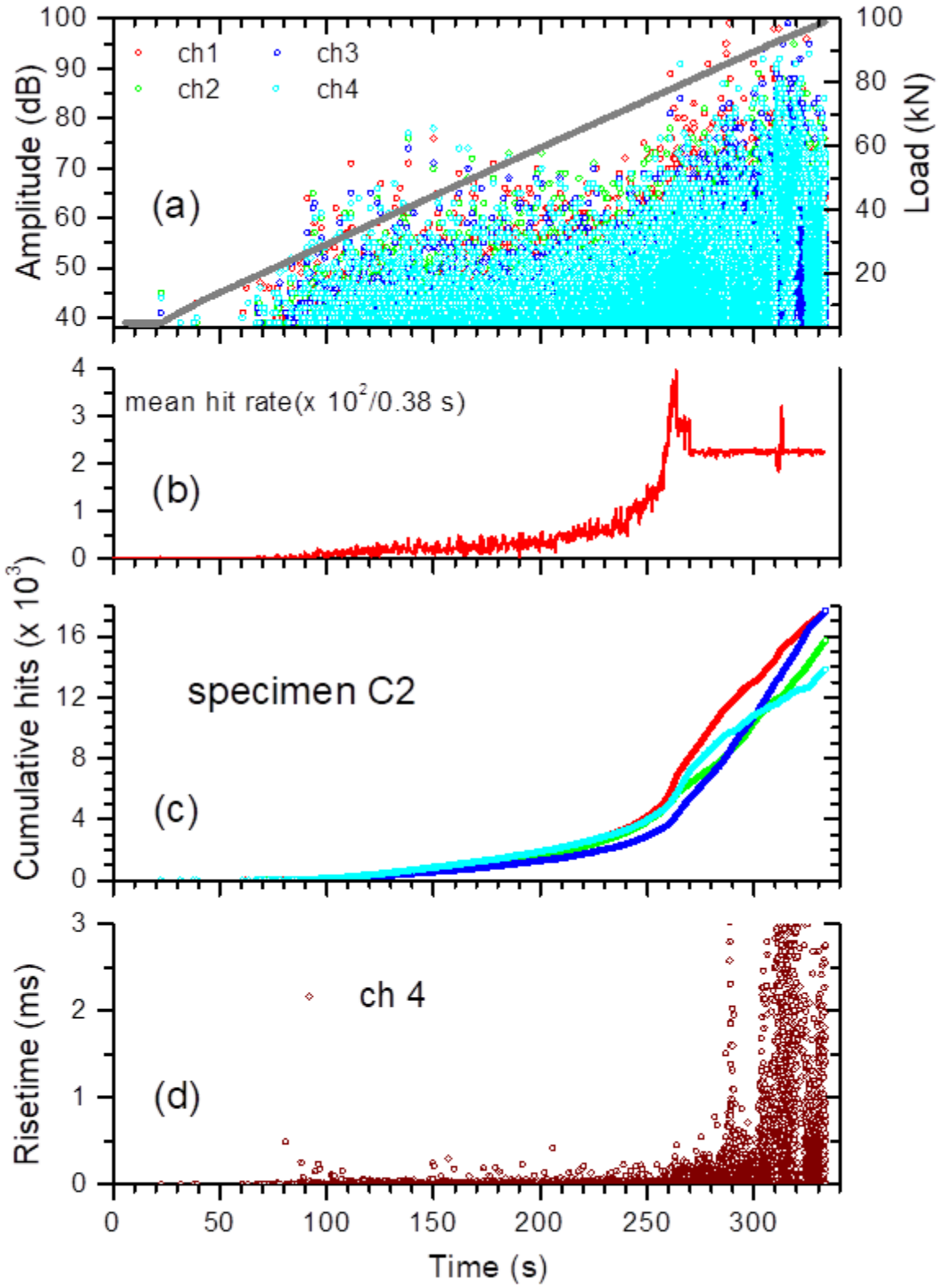

Figure 6.14: Time evolution of AE parameters during the uniaxial compression of the sandstone sample C2. (a) The amplitudes of all channels (1, 2, 3 and 4) and the applied load, (b) the mean hit rate of all channels, (c) the cumulative hits of all channels and (d) the risetime of channel 4. The final rupture of the specimen occurs at t=330 s, as indicated from the corresponding drop of the load.

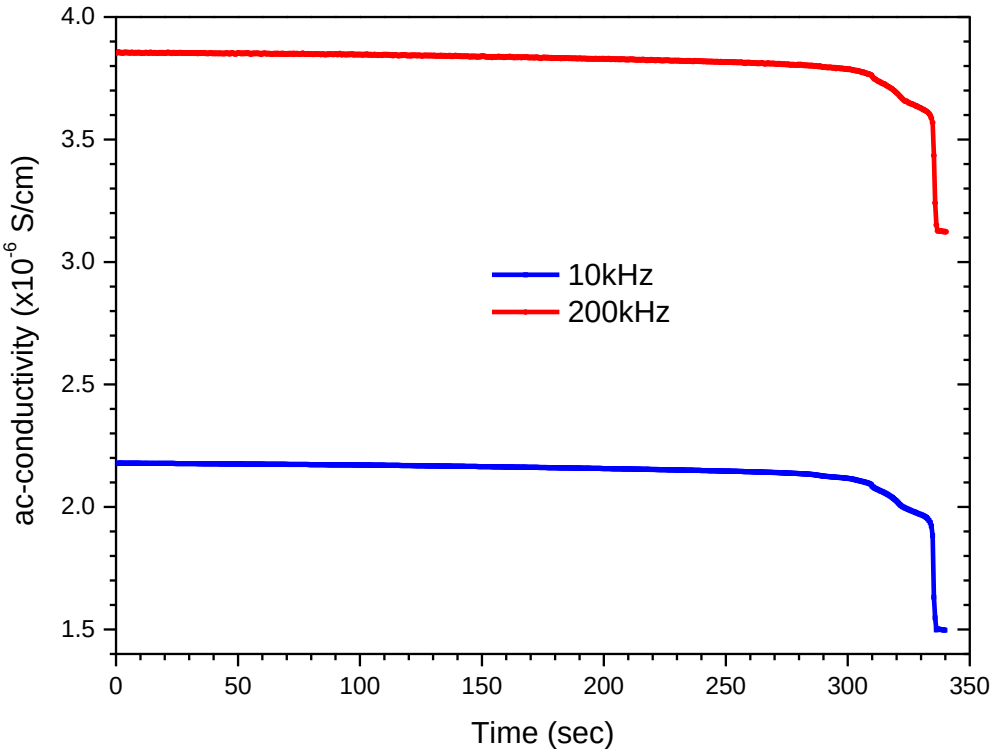

Figure 6.15: Time-series of ac-conductivity at 10 kHz and 200 kHz of the sandstone specimen C2. The final rupture of the specimen occurs at t=330 s.

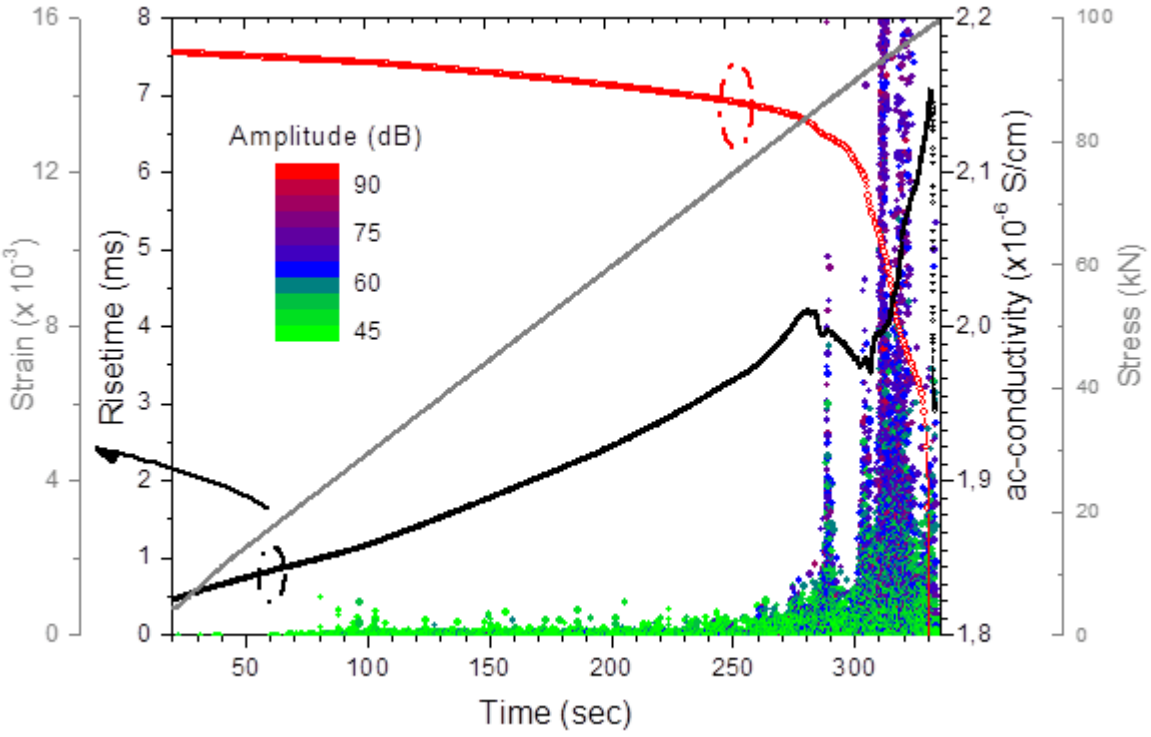

Figure 6.16: Time-series of risetime of the recorded hits in all channels and the ac-conductivity at 10kHz, during the uniaxial compression of the sandstone specimen C2. The applied stress and the induced strain are also shown.

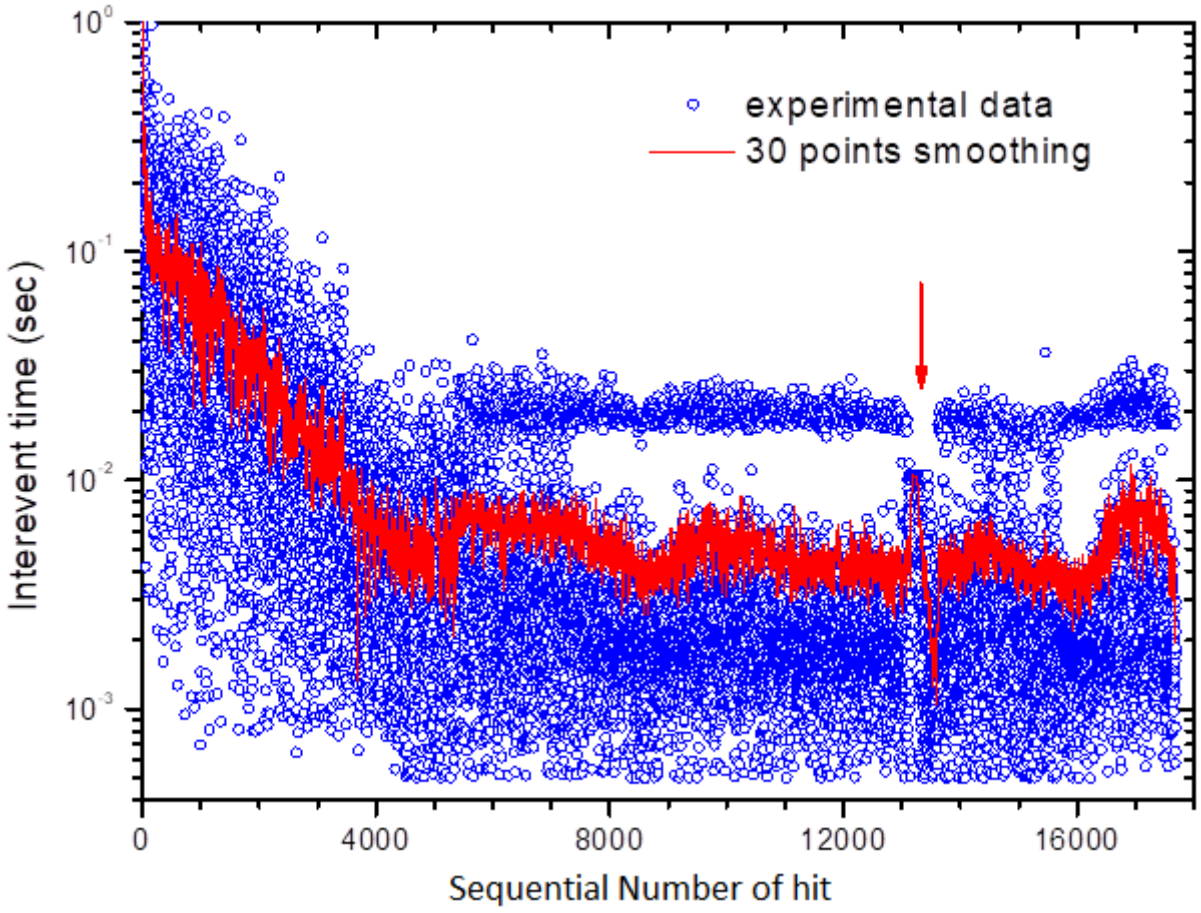

Figure 6.17: Inter-event times of recorded hits in channel 3 of the sandstone specimen C2. The red arrow indicates the initial failure of the specimen that occurred at ~260 s.

3 orders of magnitude. A continuous decrease of inter-event times is observed during the first 5000 hits (refer to Fig. 6.17). This number of hits corresponds to the time just before the initial failure of the specimen, i.e. at ~260 s. After that time, inter-event times retain an almost constant value (~5 ms) until the ultimate failure of the specimen.

The last type of experiment on a sandstone specimen exposed to ambient moisture was conducted under cyclic (saw-tooth) loading, in order to investigate the sensitivity of conductivity measurements to fluctuations of load. The loading-unloading rate in each cycle remained the same with that in the linear loading experiments, i.e. 0.3 kN/s. The evolution of the AE parameters and the measured time-series of ac-conductivity during the uniaxial loading of specimen C3 are shown in Figs. 6.18 – 6.21. The AE parameters, i.e. the amplitudes of the recorded hits, the mean hit rate, the

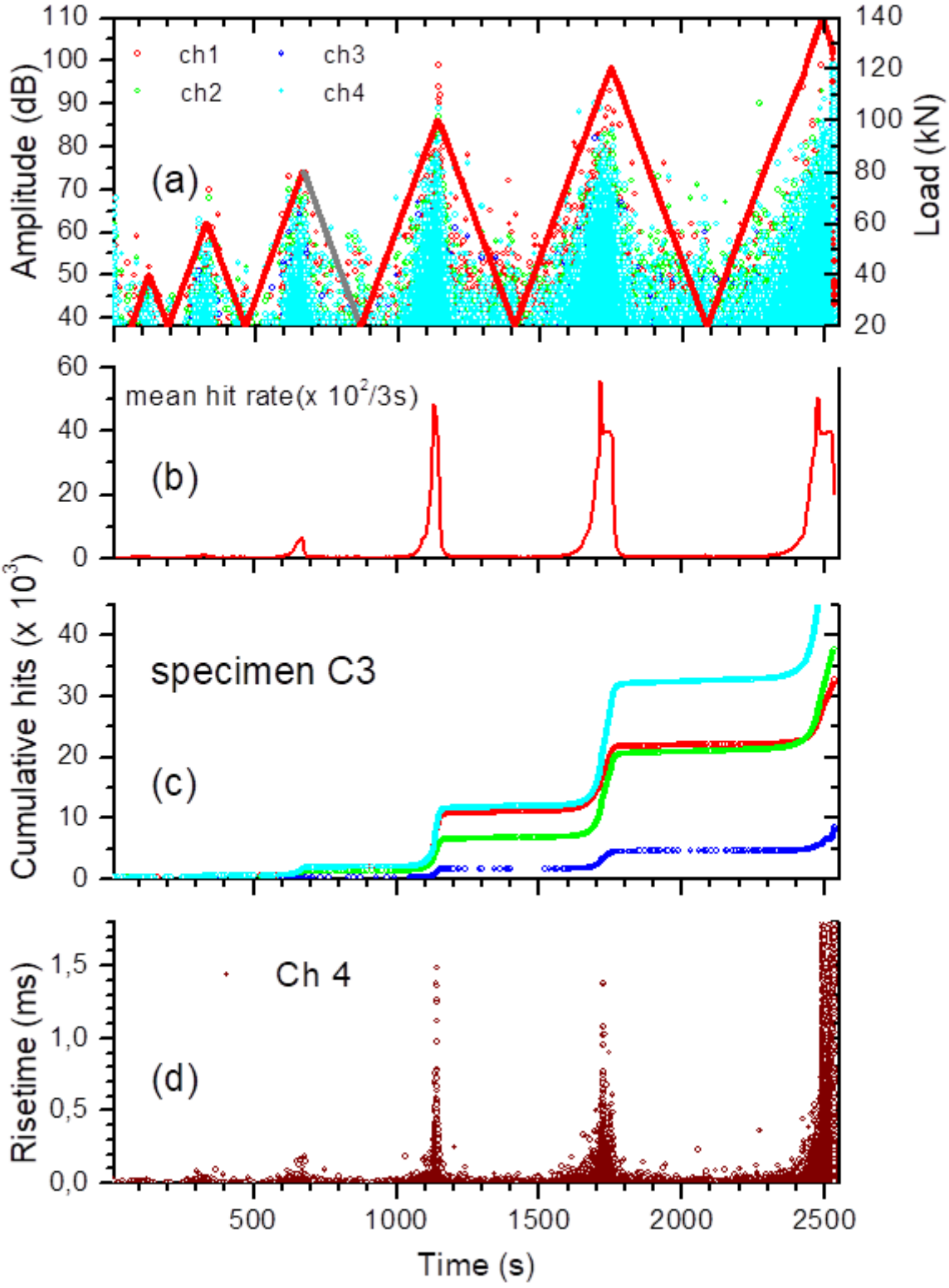

Figure 6.18: Time evolution of AE parameters during the uniaxial compression of the sandstone specimen C3. (a) The amplitudes of all channels (1, 2, 3 and 4) and the applied load, (b) the mean hit rate of all channels, (c) the cumulative hits of all channels and (d) the risetime of channel 4. The final rupture of the specimen occurs at t=2500 s, as indicated from the corresponding drop of the load.

cumulative hits and the risetime during the loading part of each cycle exhibit similar characteristics with that during the linear loading of specimen C2 (refer to Fig. 6.14). Specifically, a high hit rate is recorded during the 4th loading cycle where the stress peak reaches 100 kN. The ultimate failure occurs during the unloading of the 6th cycle, where the load increased to 140 kN. A small AE activity is also observed during the unloading parts of the sequential cycles. At the peak stress of each cycle, hits with maximum amplitudes and high values of risetime are recorded. The inter-event time in each cyclic loading decreases rapidly with the increment of the stress, followed by a slow relaxation to its initial value (refer to Fig. 6.21). In the cycles of considerable AE activity (4th to 6th cycle), inter-event times span to 3-4 orders of magnitude.

A strong correlation of the AE activity and the measured ac-conductivity is clearly observed in Figs. 6.19 and 6.20. Ac-conductivity in both measured frequencies (10 kHz and 200 kHz) exhibit the same characteristics during the cyclic loading. Up to the peak stress of 100 kN, conductivity increases smoothly exhibiting small fluctuations which are related to the first 3 loading-unloading loops of the specimen.

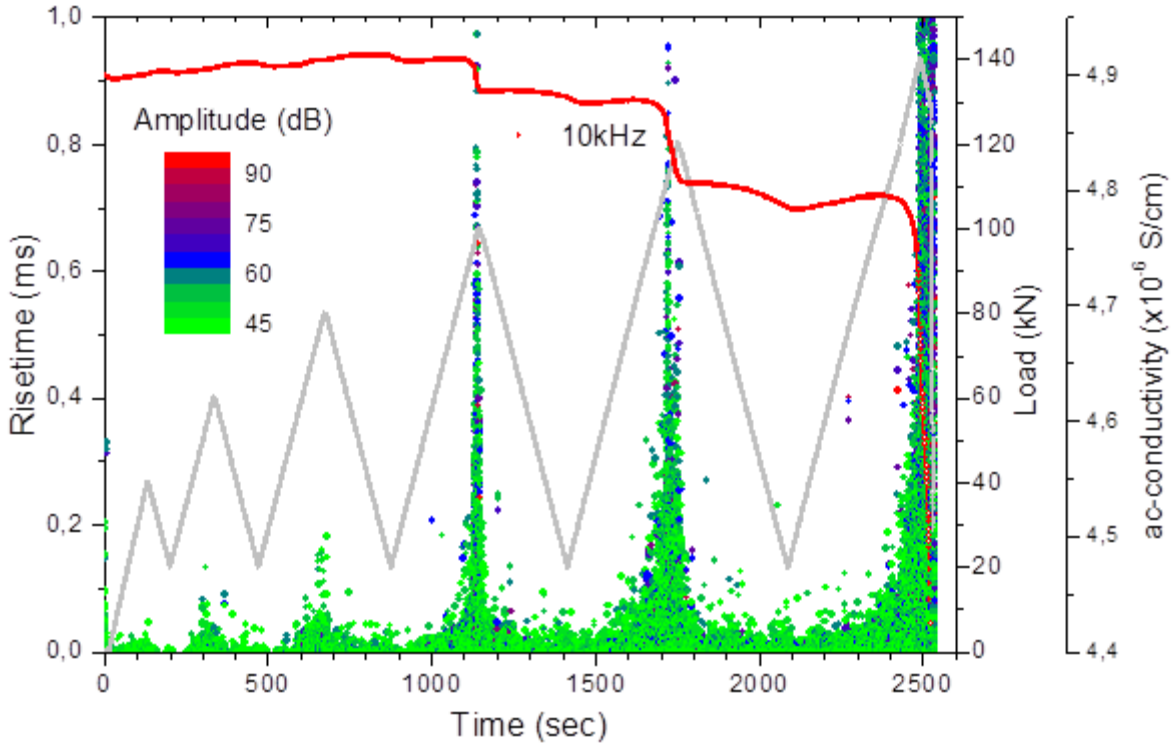

Figure 6.19: Time-series of the risetime of recorded hits, ac-conductivity at 10 kHz and the applied cyclic load, during the uniaxial compression of the sandstone sample C3.

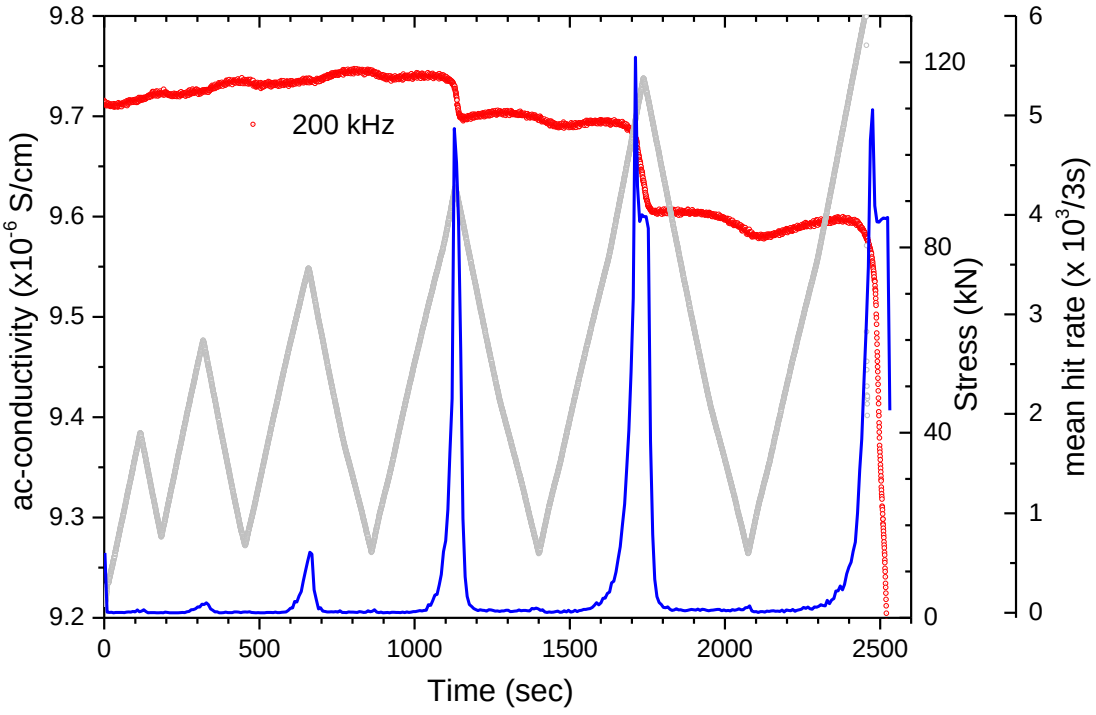

Figure 6.20: Time-series of ac-conductivity at 200 kHz of the sandstone sample C3 in conjunction with the hit rate and the cyclic loading. The final rupture of the specimen occurs at t=2500 s according to the rapid increase of curve.

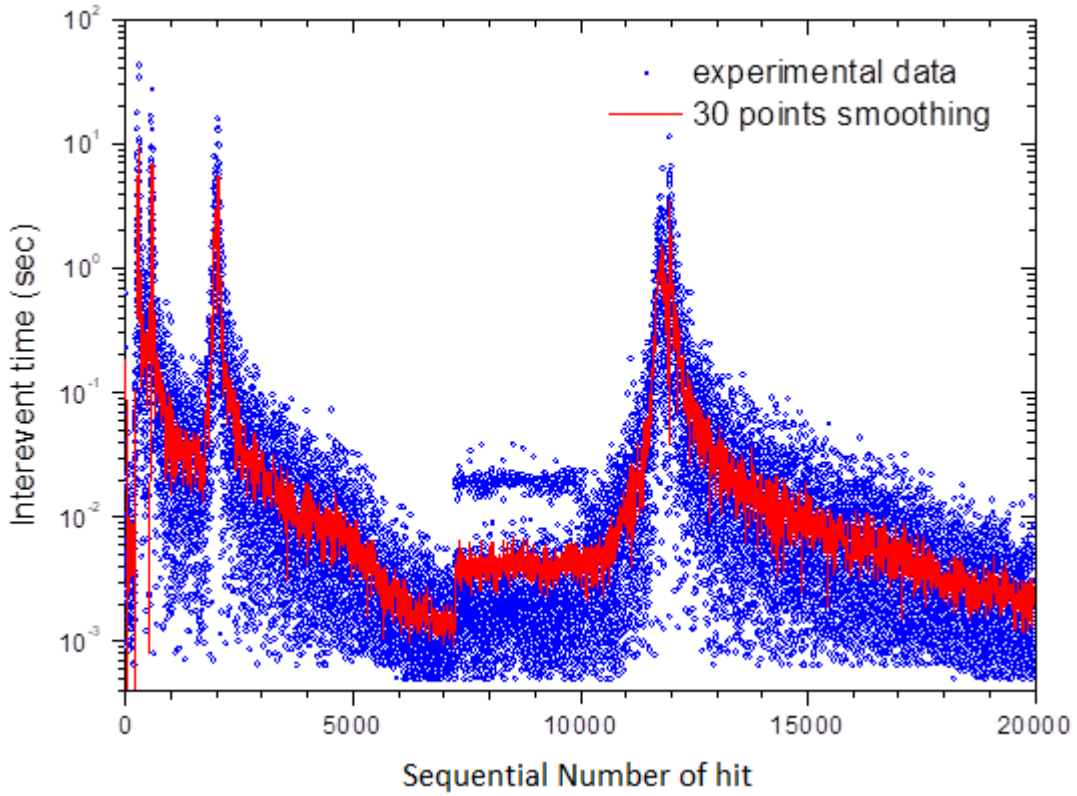

Figure 6.21: Inter-event times of recorded hits in channel 4 of the sandstone specimen C3.

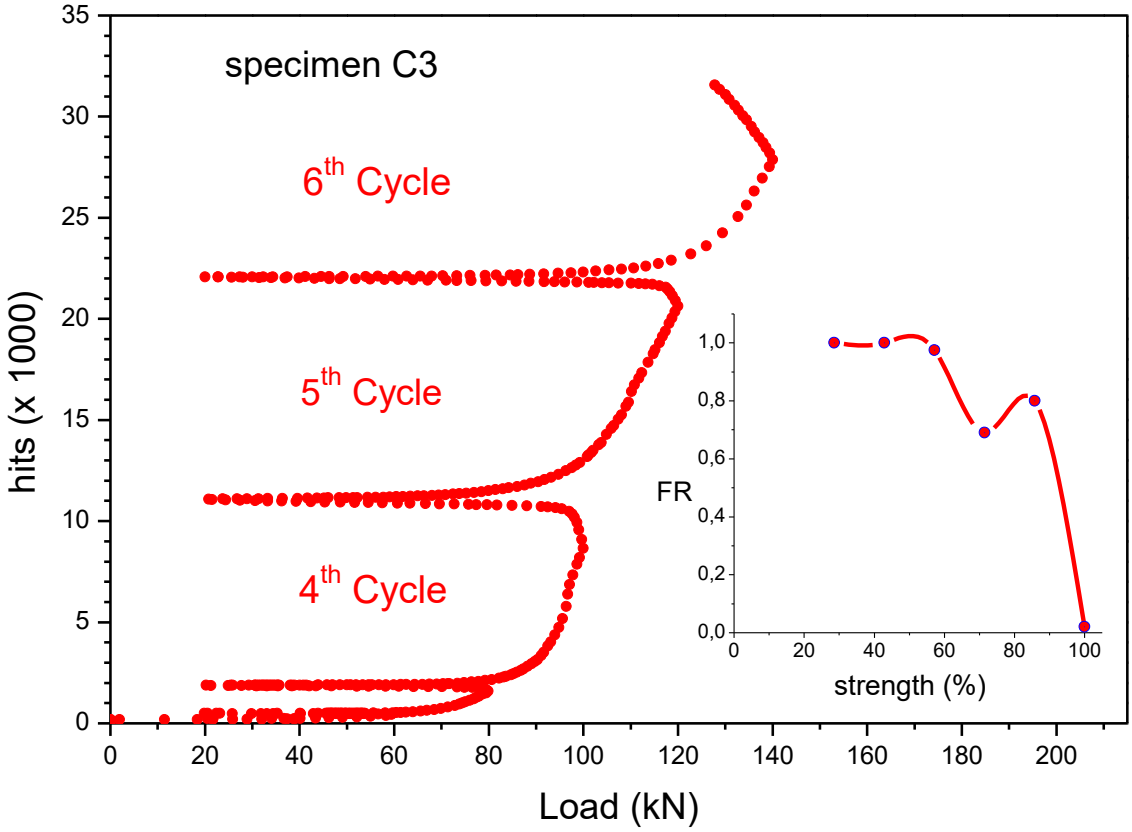

Figure 6.22: The cumulative number of hits recorded in all channels, during the cyclic (saw-tooth) loading of the sandstone specimen C3. The 1st and 2nd cycle are not clearly observed due to the small number of recorded hits. The inset shows the Felicity Ratio (FR) as a function of the percentage strength of the specimen.

At the peak stress of 100 kN and the subsequent peak of 120 kN, conductivity decreases abruptly, exhibiting intermediate fluctuations. In particular, between these successive stress peaks, conductivity decreases slightly and then rises again, following the variation of the applied stress. This behaviour of conductivity is attributed to the continued cracks generation that occurred during the gradual release of stress and the subsequent relaxation of the specimen prior to the next stress peak.

The accumulation of damage into the material can be expressed in these repetitive loading cycles of the sandstone specimen through the Felicity ratio (FR) which may be estimated from the plot of the cumulative hits as a function of the applied load (Fig. 6.22). The lower the FR, the more damage the specimen has suffered. The inset of Fig. 6.22 shows the calculated values of FR with respect to the percentage of the compressive strength of the specimen. We observe that in the 5th cycle, FR has a higher value than that in the previous one. This can be attributed to the fact that the specimen during the 4th cycle

(stress peak of 100 kN or 71 % of compressive strength) has exited from its elastic response, resulting in significant generation and propagation of micro-cracks, as it is evident from the corresponding high hit rate [refer to Fig. 6.18(b)]. Thus, in the next cycle, we may expect a similar, or even lower, degree of damage to the specimen leading to a higher FR. A similar behaviour has been recently observed by Stavrakas (2017) who investigated the Kaiser effect during repetitive loading loops in marble specimens.

The previous set of experiments under different types of loading in cylindrical specimens was repeated in water-saturated sandstones specimens, in order to investigate the influence of water to the AE parameters and its correlation with the measured ac-conductivity.

Regarding the stepped-like uniaxial loading of the water-saturated sandstone specimen (C4), the evolution of the AE parameters and the measured ac-conductivity are shown in Figs. 6.23 – 6.26. It is worth mentioning that the duration of the whole experiment was much less that the corresponding in the sandstone specimen C1. This is due both to the lower strength of the specimen C4 (100 kN) and to the low AE activity during the loading steps up to 80 kN, which allowed us to measure the conductivity spectrum almost immediately after the pressure increase at each loading step.

The low AE hit rate that observed up to 80% of the failure load could be attributed to the influence of water which acts as a lubricant in the newly formed cracks and reduces the friction between the fault planes. The latter is responsible for continuous acoustic emission activity.

The significant difference in the ac-conductivity between the specimen C4 and the specimen C1 which was saturated in ambient air (refer to Fig. 6.12) is the increase that is observed in specimen C4. Specifically, as it is shown in Fig. 6.25, except of the higher absolute values of the measured conductivity with respect to the specimen C1 (about 2.5 orders of magnitude), conductivity increases with the applied uniaxial load. This increase is rather small up to 80 kN, but afterwards it becomes larger, until failure of the specimen. Noteworthy, the ac-conductivity in all the measured frequencies (1 Hz, 10 kHz and 200 kHz) exhibit the same behaviour with respect to the load.

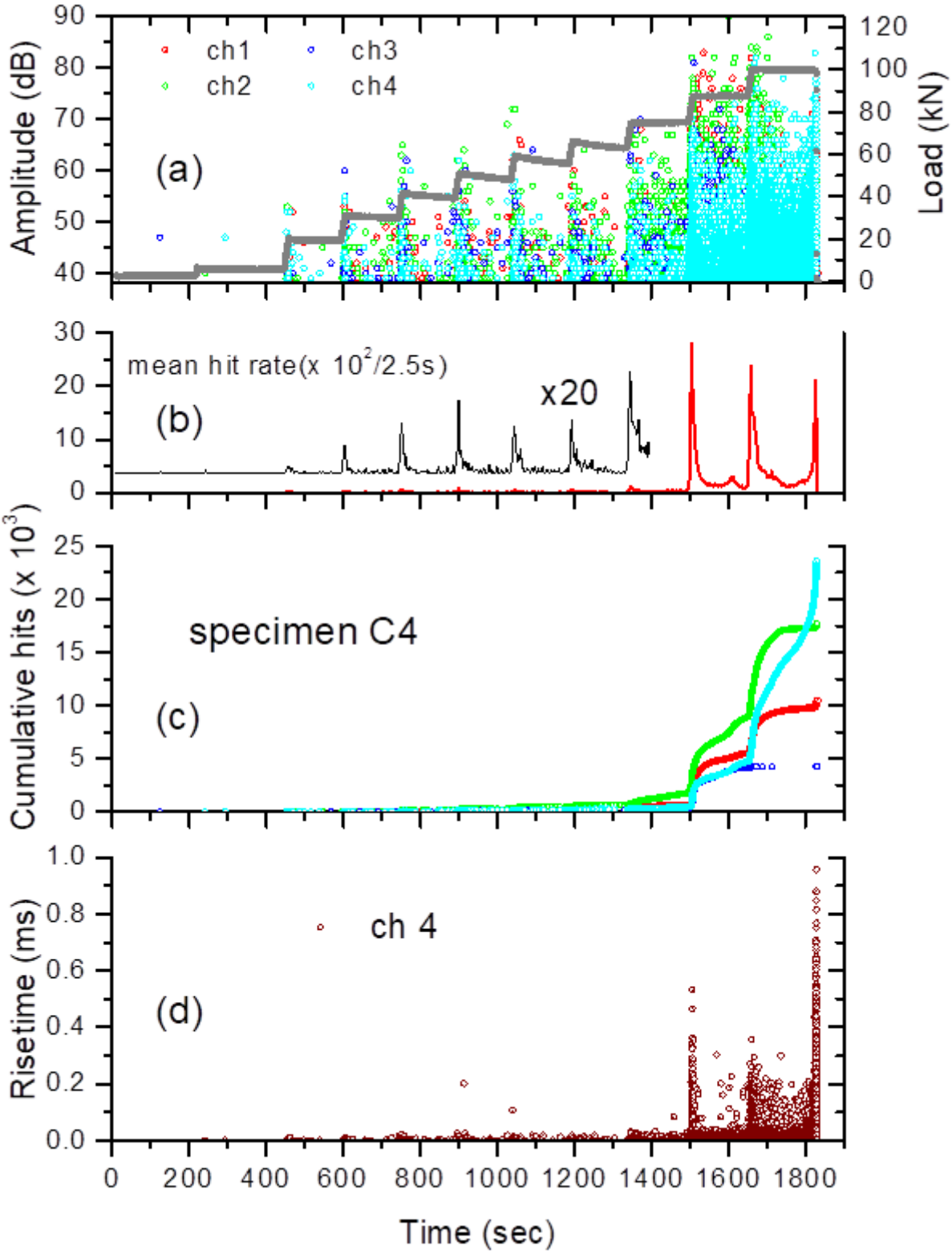

Figure 6.23: Time evolution of AE parameters during the uniaxial compression of the sandstone sample C4. (a) The amplitudes of all channels (1, 2, 3 and 4) and the applied load, (b) the mean hit rate of all channels, (c) the cumulative hits of all channels and (d) the risetime of channel 4. The final rupture of the specimen occurs at t=1820 s, as indicated from the corresponding drop of the load.

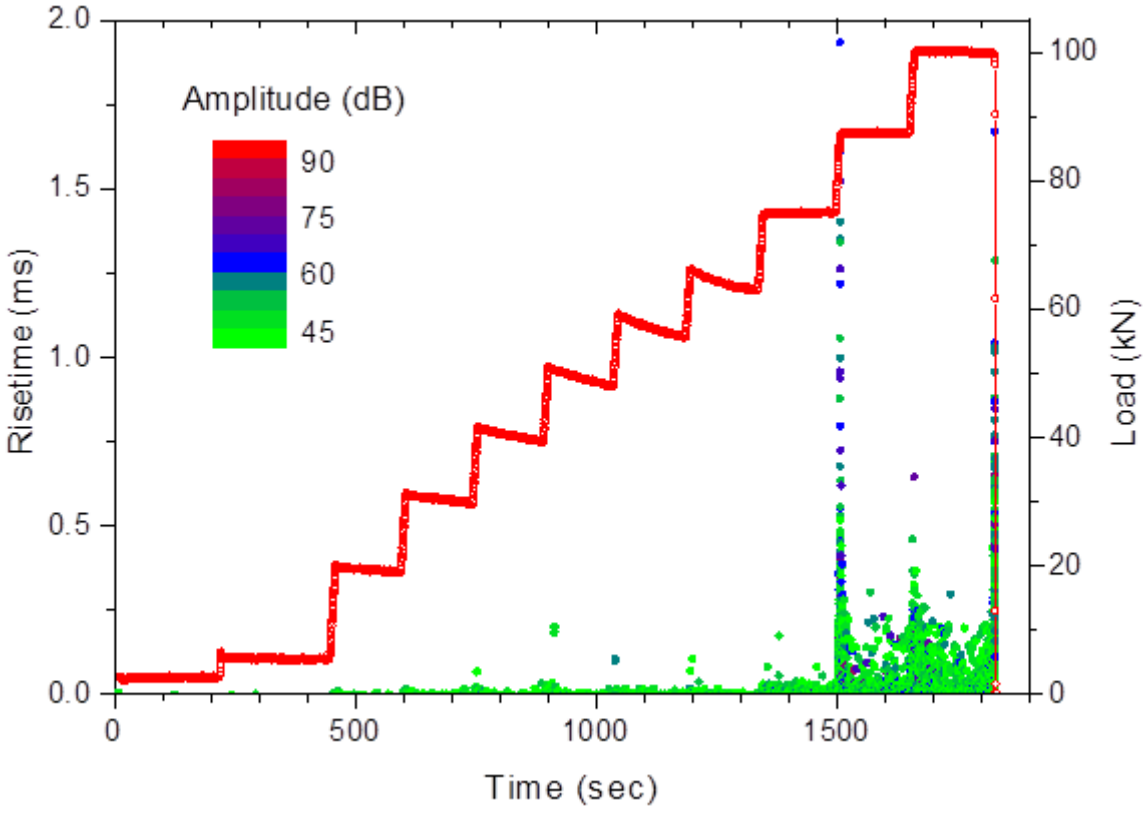

Figure 6.24: Time-series of risetime of recorded hits during the uniaxial compression of the sandstone specimen C4. The applied stepped-like load is also shown.

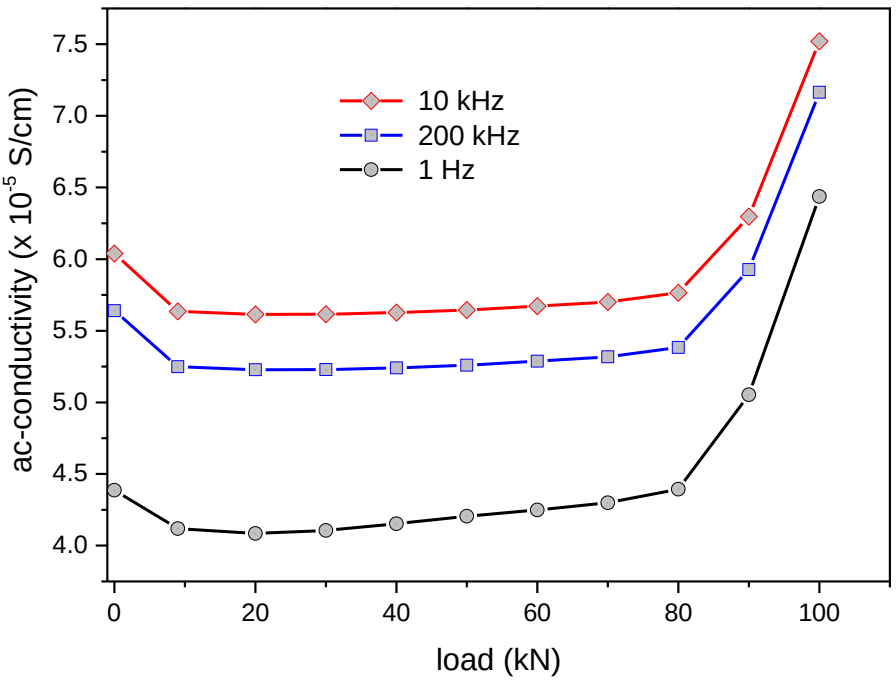

Figure 6.25: Ac-conductivity at 3 measured frequencies (1 Hz, 10 kHz and 200 kHz) as a function of the applied load during the stepped uniaxial compression of the sandstone sample C4.

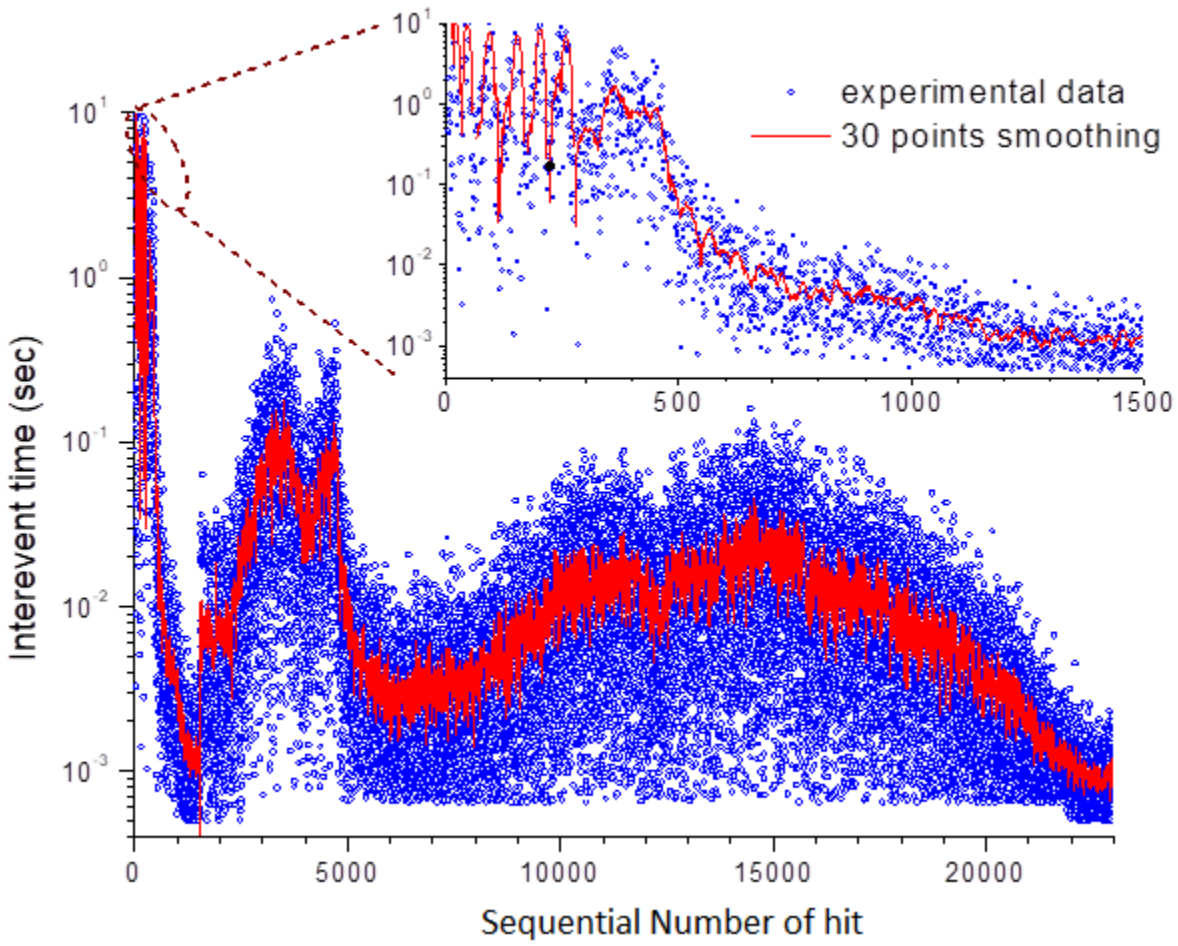

Figure 6.26: Inter-event times of recorded hits in channel 4 of the sandstone specimen C4.

The inter-event times of recorded hits in channel 4 during the stepped-like loading of specimen C4 as a function of the number of successive hits are shown in Fig. 6.26. Up to 80 kN (see the inset of Fig. 6.26) inter-event times decrease, covering about 4 orders of magnitude. At higher loads up to the fracture (100 kN), inter-event times exhibit a rather complicated behaviour and no safe conclusions can be drawn.

During the linear loading of the water-saturated sandstone specimen (C5) the calculated AE parameters (amplitudes, mean hot rate, cumulative hits, risetime and inter-event times), the measured ac-conductivity at 10 and 200 kHz and their correlation plot, are shown in Figs. 6.27 – 6.30.

Considerable AE activity starts at 300 s where suddenly a strong peak in the mean hit rate is observed. This high hit rate of high recorded amplitudes should be related to the formation of a macroscopic failure of the specimen. At that time, the load corresponds to about 55% of the compression strength (18.5 MPa) of the specimen C5, considering that

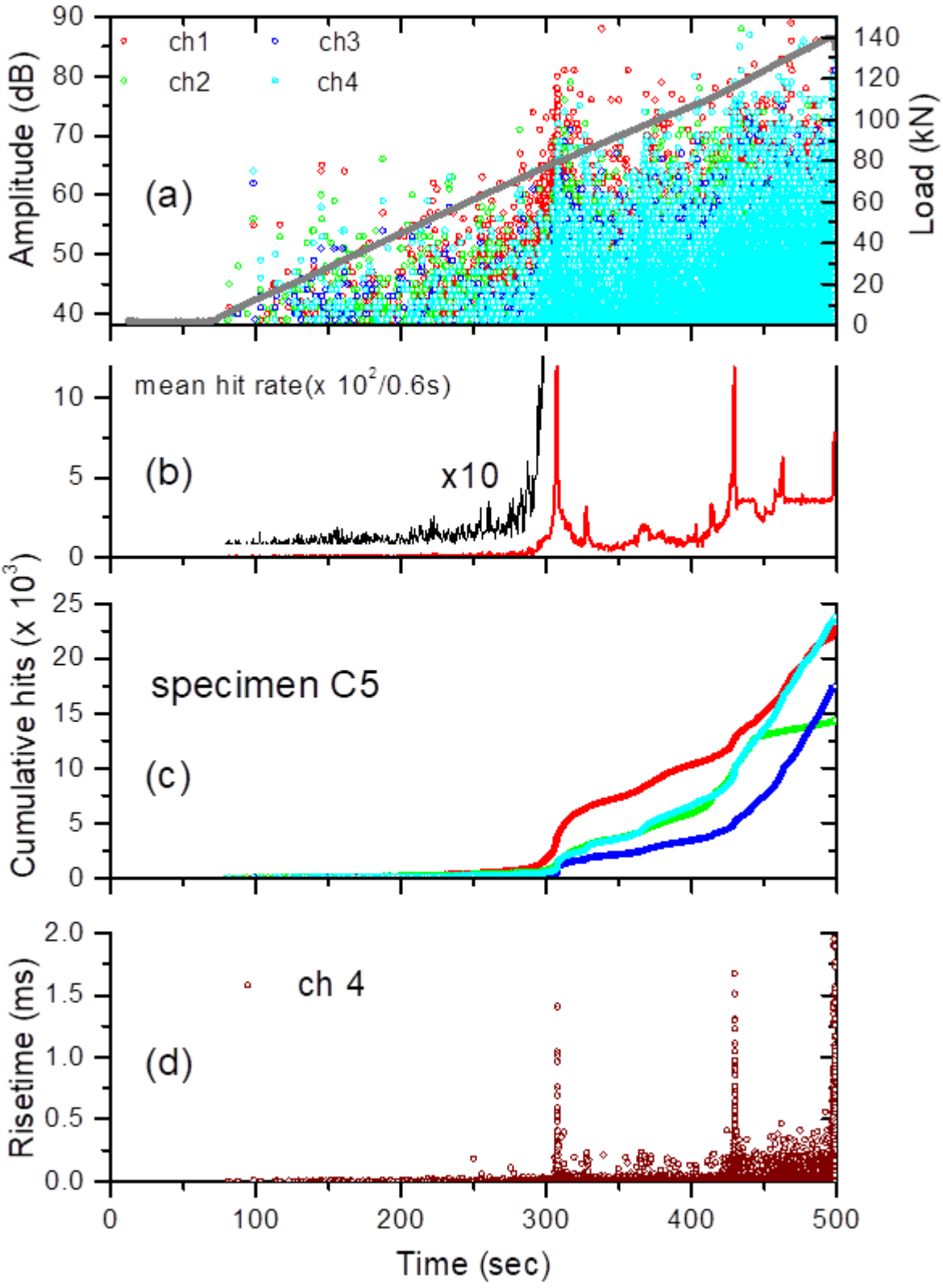

Figure 6.27: Time evolution of AE parameters during the uniaxial compression of the sandstone specimen C5. (a) The amplitudes of all channels (1, 2, 3 and 4) and the applied load, (b) the mean hit rate of all channels, (c) the cumulative hits of all channels and (d) the risetime of channel 4. The final rupture of the specimen occurs at t=490 s, as indicated from the corresponding drop of the load.

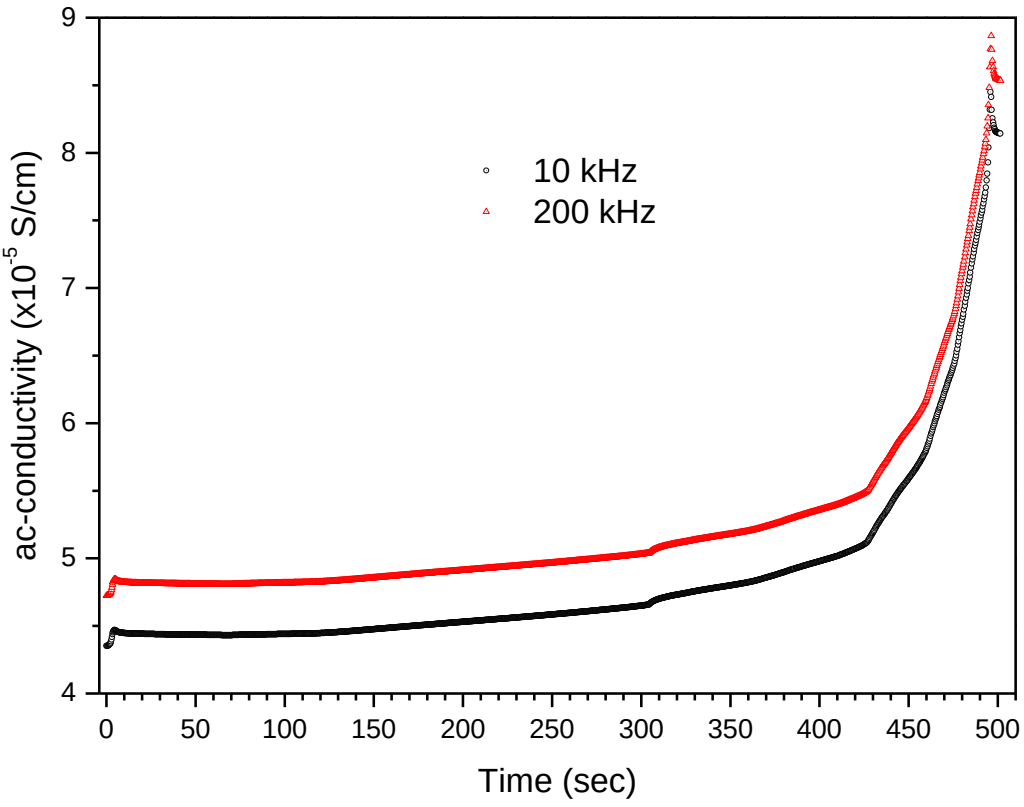

Figure 6.28: Time-series of ac-conductivity measured at 10 kHz and 200 kHz of the sandstone specimen C5.

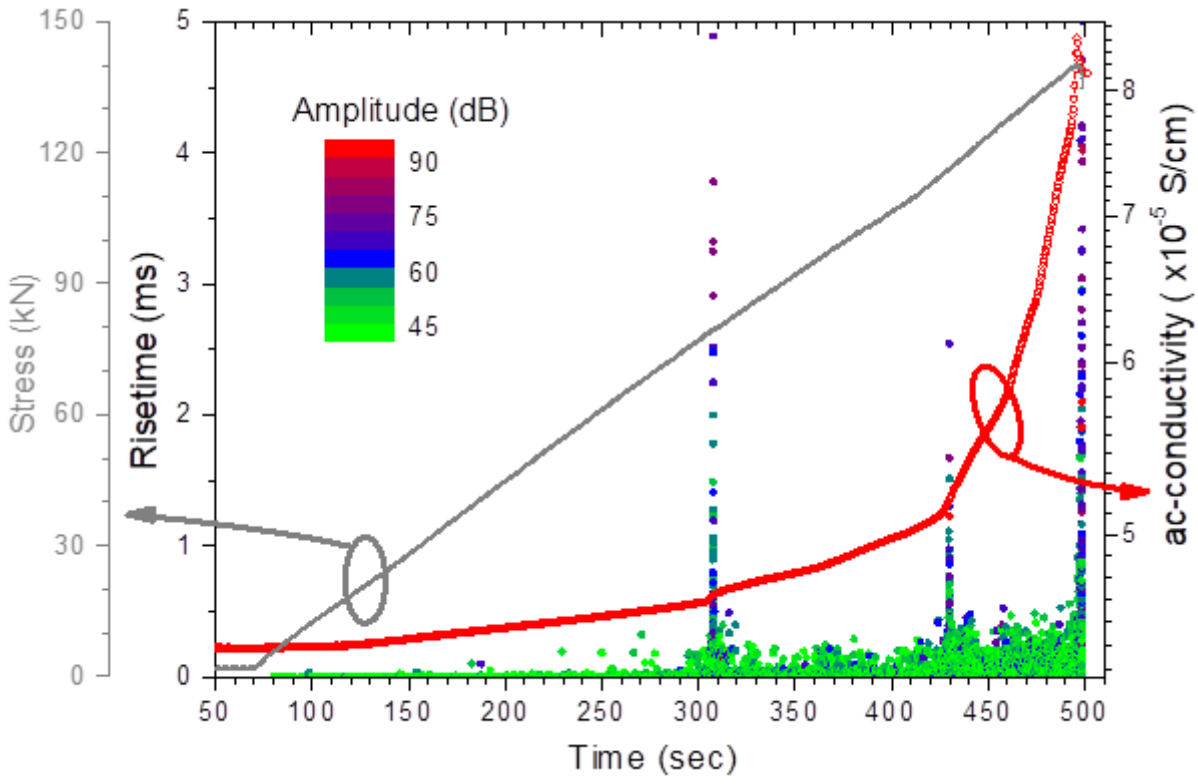

Figure 6.29: Time-series of risetime of recorded hits, applied load and ac-conductivity at 10 kHz during the uniaxial compression of the sandstone specimen C5.

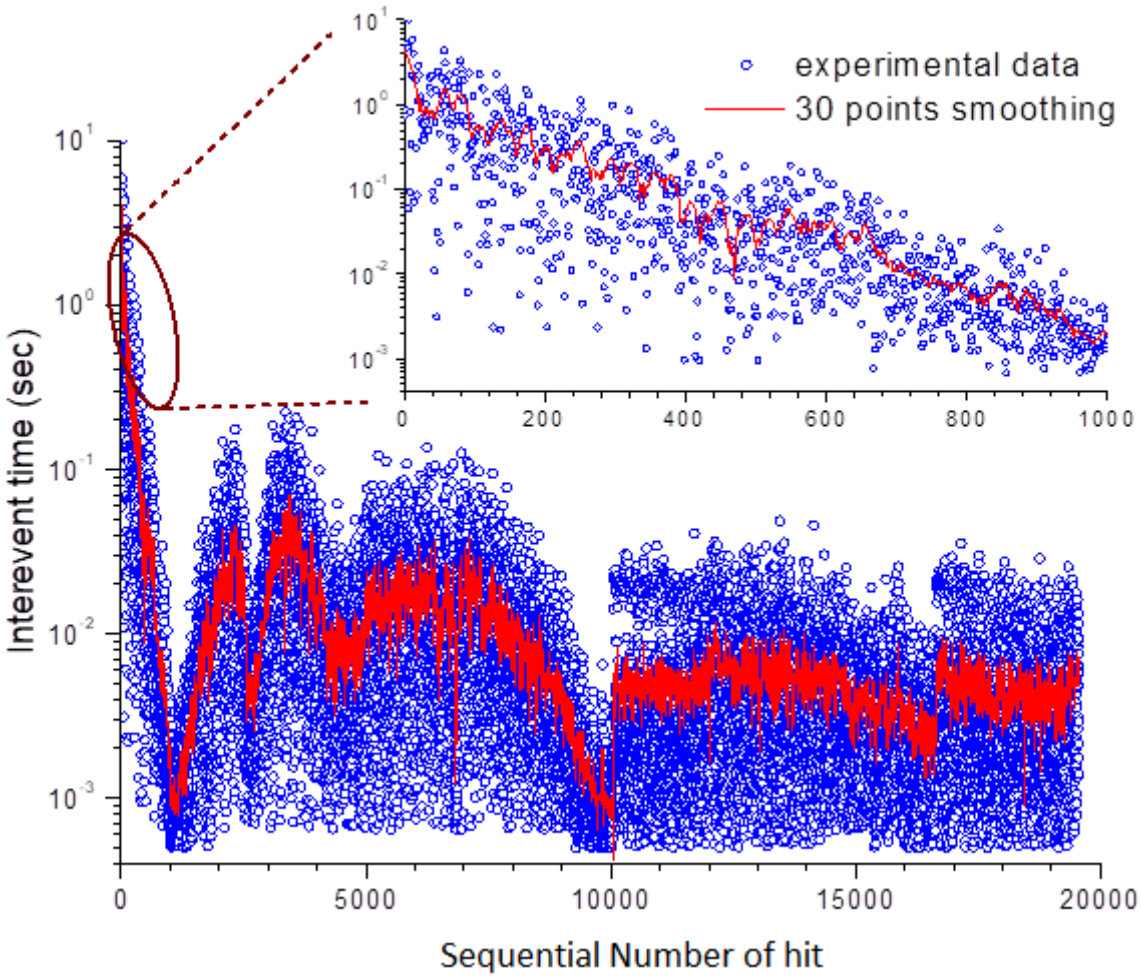

Figure 6.30: Inter-event times of recorded hits in channel 4 of the sandstone specimen C5.

complete failure of the specimen occurs at 500 s. However, by comparing the AE activity of the two specimens (C2 and C5) with different water content that were subjected to linear loading, we could also deduce that the first indication of macroscopic failure occurs at around 80 kN for both of them [refer to Fig. 6.14(a, b) and 6.27(a, b)]. As the cumulative number of hits is lower in the case of the water-saturated specimen, we may conclude that the influence of water is responsible for the lower AE activity that is recorded in the case of specimen C5. The latter is attributed to the role of water as a lubricant which reduces the friction-induced AE activity, as it was mentioned previously.

The ac-conductivity measurements at two distinct frequencies (10 and 200 kHz) exhibit the same behaviour, as it is clearly shown in Fig. 6.28. As in the case of specimen C4 which was subjected to stepped-like loading, conductivity increases smoothly with the applied load, reaching a maximum value prior to the final rupture. The correlation of the

ac-conductivity measured at 10 kHz and the risetime is illustrated in Fig. 6.29. The main failure of the sample indicated by high risetime values recorded at 308 s and 430 s is also associated with abrupt changes to the measured conductivity.

Finally, the inter-event times of the recorded hits in channel 4 with respect to the successive number of hits are shown in Fig. 6.30. A rapid decrease of more than 4 orders of magnitude is observed when the specimen reaches to its first main damage at 305 s. Afterwards, inter-event times increase again until the next failure point.

The last cylindrical water-saturated sandstone specimen (C6) was subjected to cyclic (saw-tooth) loading, up to the ultimate failure which occurred during the 6^{th} cycle, at 132 kN. The time evolution of the AE parameters and the ac-conductivity is shown in Figs. 6.31 – 6.33. Although the duration of the experiment and therefore the maximum load (132 kN) is almost the same as that of specimen C3 [refer to Fig. 6.18(a)], the AE activity expressed as the cumulative number of hits is less than half of specimen C3. This is attributed to the role of the water, as discussed previously.

A strong correlation of the pressure-induced AE activity and the ac-conductivity is clearly observed during the saw-tooth loading of specimen C6 (refer to Fig. 6.32). In each loading cycle, the variation in ac-conductivity follows a specific shape but with higher values each time, as the specimen approaches the failure. Specifically, during the 1^{st} cycle, (40 kN peak stress), conductivity increases simultaneously with the AE activity and stabilizes to a certain value when no other hits are recorded. At the beginning of the next cycle conductivity decreases slowly. The subsequent initiation of the AE activity causes the increment of conductivity with a rate that increases in each successive loading cycle.

The previous behaviour of ac-conductivity is also reflected to the Felicity effect that is observed during the sequential loading of specimen C6 and is depicted in Fig. 6.34. The Felicity ratio (FR) as a function of the percentage strength is also shown in the inset of Fig. 6.34.

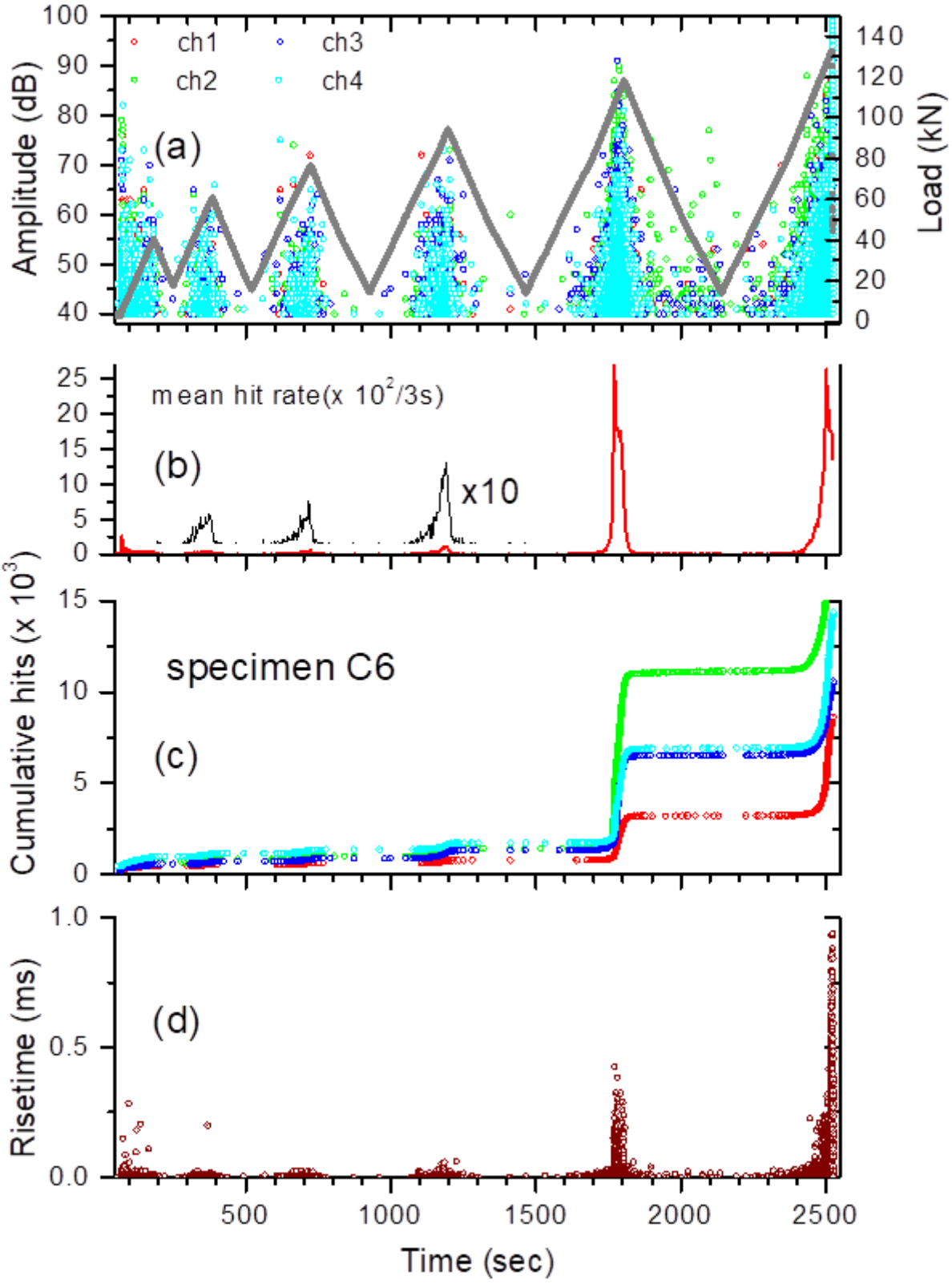

Figure 6.31: Time evolution of AE parameters during the uniaxial compression of the sandstone specimen C6. (a) The amplitudes of all channels (1, 2, 3 and 4) and the applied load, (b) the mean hit rate of all channels, (c) the cumulative hits of all channels and (d) the risetime of channel 4. The final rupture of the specimen occurs at t=2520 s, as indicated from the corresponding drop of the load.

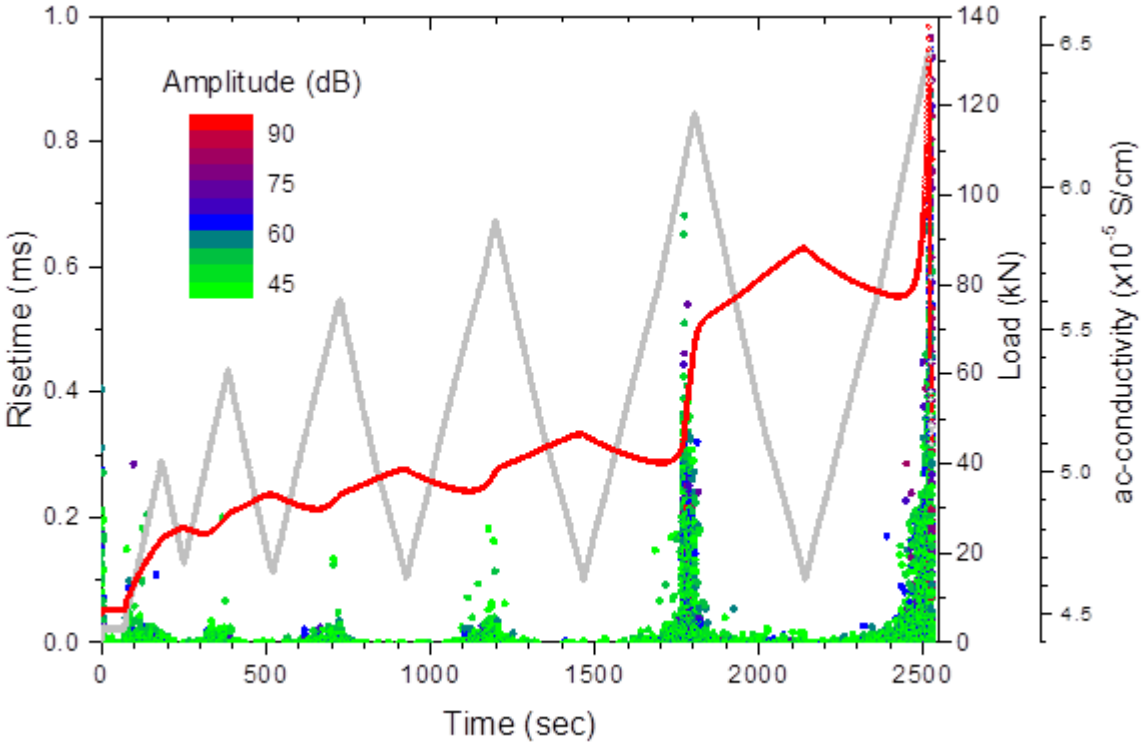

Figure 6.32: Time evolution of risetime for all channels and of ac-conductivity at 10 kHz, during the uniaxial compression of the sandstone specimen C6. The applied cyclic load is also shown.

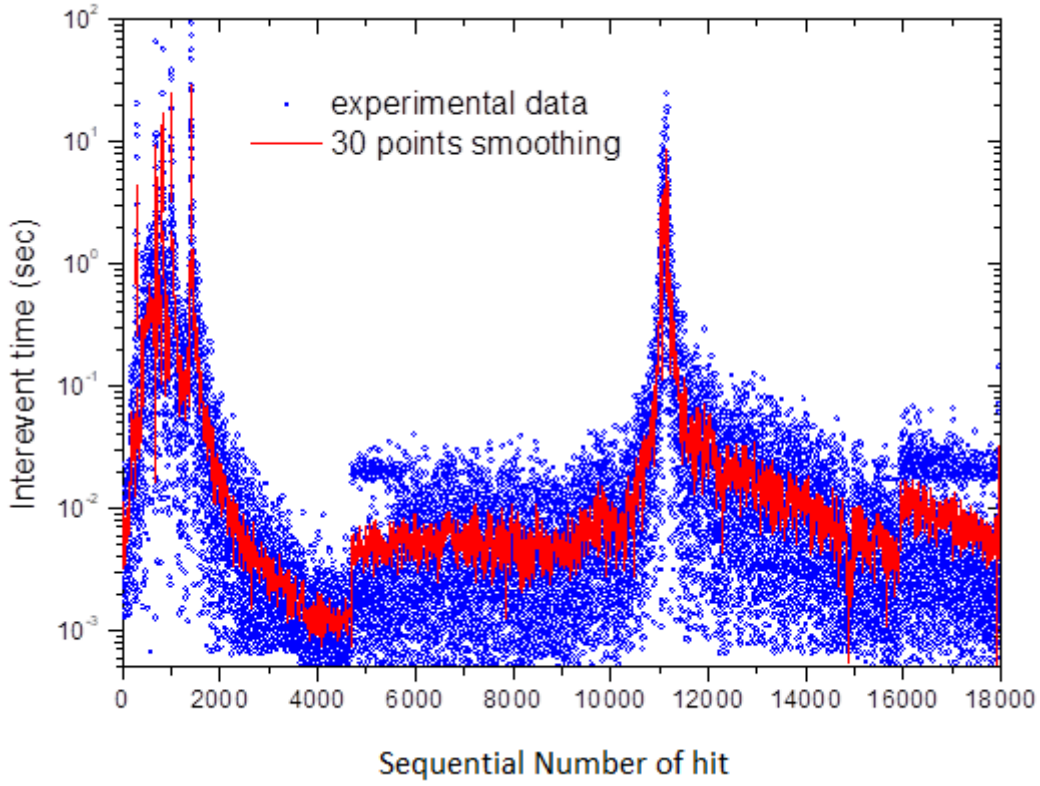

Figure 6.33: Inter-event times of recorded hits in channel 4 of the sandstone specimen C6.

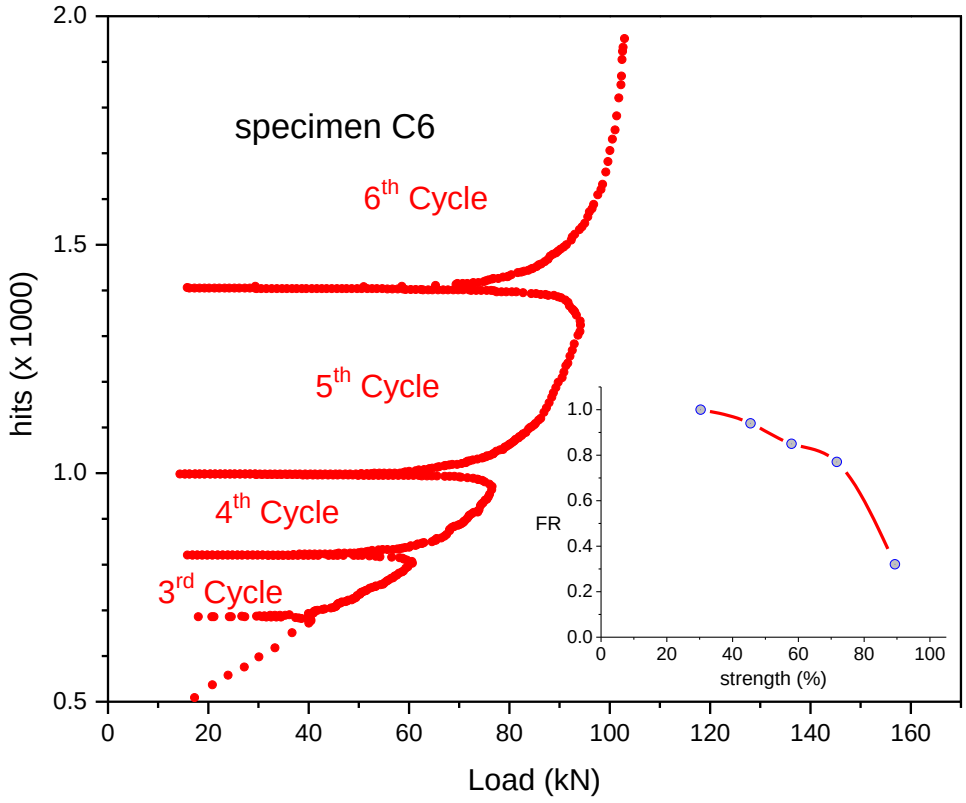

Figure 6.34: The cumulative number of hits recorded in all channels during the cyclic loading of the sandstone specimen C6. The inset shows the FR as a function of the percentage strength of the specimen. The last loading is not shown due to the high number of hits which masks the previous cycles.

6.2.2 Location of events

The location of events for specimens C1 to C6 can be accurately performed only in two dimensions. Due to the limitation of low height/diameter ratios in order to perform the conductivity measurements, the sensors were practically positioned at the same plane, that is, at the circumference of the specimens that have heights around 20 mm. The velocity of the acoustic waves in the cylindrical specimens was determined by placing 2 AE sensors at diametrically opposite positions. The estimated wave velocity was found to be (2580±10) m/s. The events that were located outside the specimens were excluded from the presentation. Furthermore, the data were filtered in order to keep only the events with high amplitudes, while hits of low amplitudes were rejected as they give inaccurate positions of events. The amplitude filters, the duration and the number of the events for each specimen are summarized in Table 6.1.

Representative top views of the specimens C1 and C6 after the uniaxial compression tests are shown in Fig. 6.35. The locations of events for all the cylindrical specimens are presented in two-dimensions in Fig. 6.36. In all cases, macro-cracks appear circumferentially on the surface of the cylindrical specimens. The central area remains almost undamaged which can be explained from the special geometry of the cylindrical specimens, i.e. the low height/diameter ratios. This could also explain the observed high AE activity before the ultimate failure of the specimen [see for example Fig. 6.27(b)].

Table 6.1: Amplitude filters, duration and number of events for cylindrical samples

Sample	Number of Events	Duration (s)	Amplitude filter (dB)
C1	8339	11386	>65
C2	1359	333	>55
C3	1695	2536	>60
C4	1507	499	>60
C5	1072	2526	>55
C6	541	1832	>55

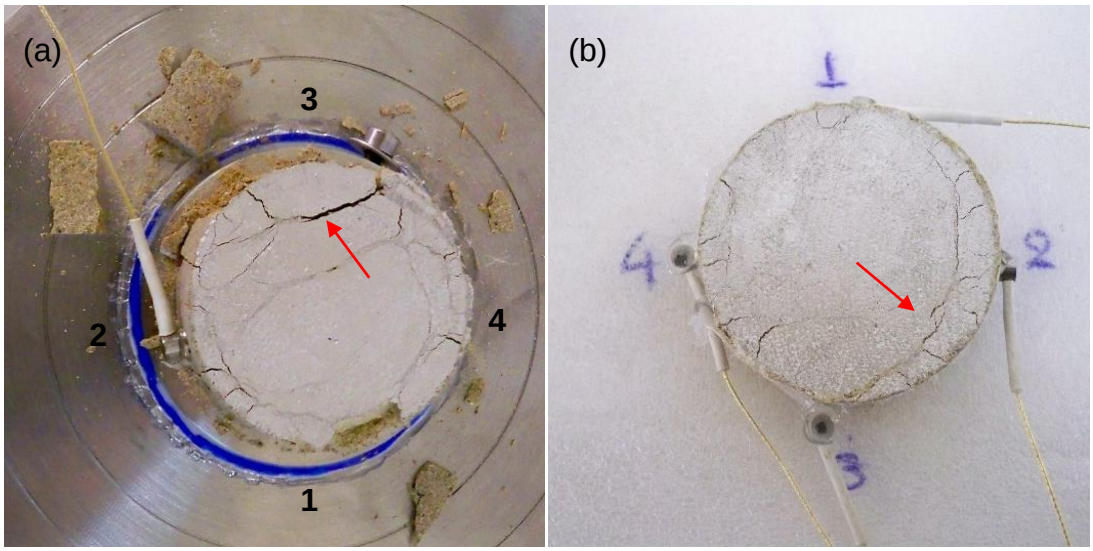

Figure 6.35: Top views of (a) specimen C1 and (b) specimen C6 after the uniaxial loading experiments.

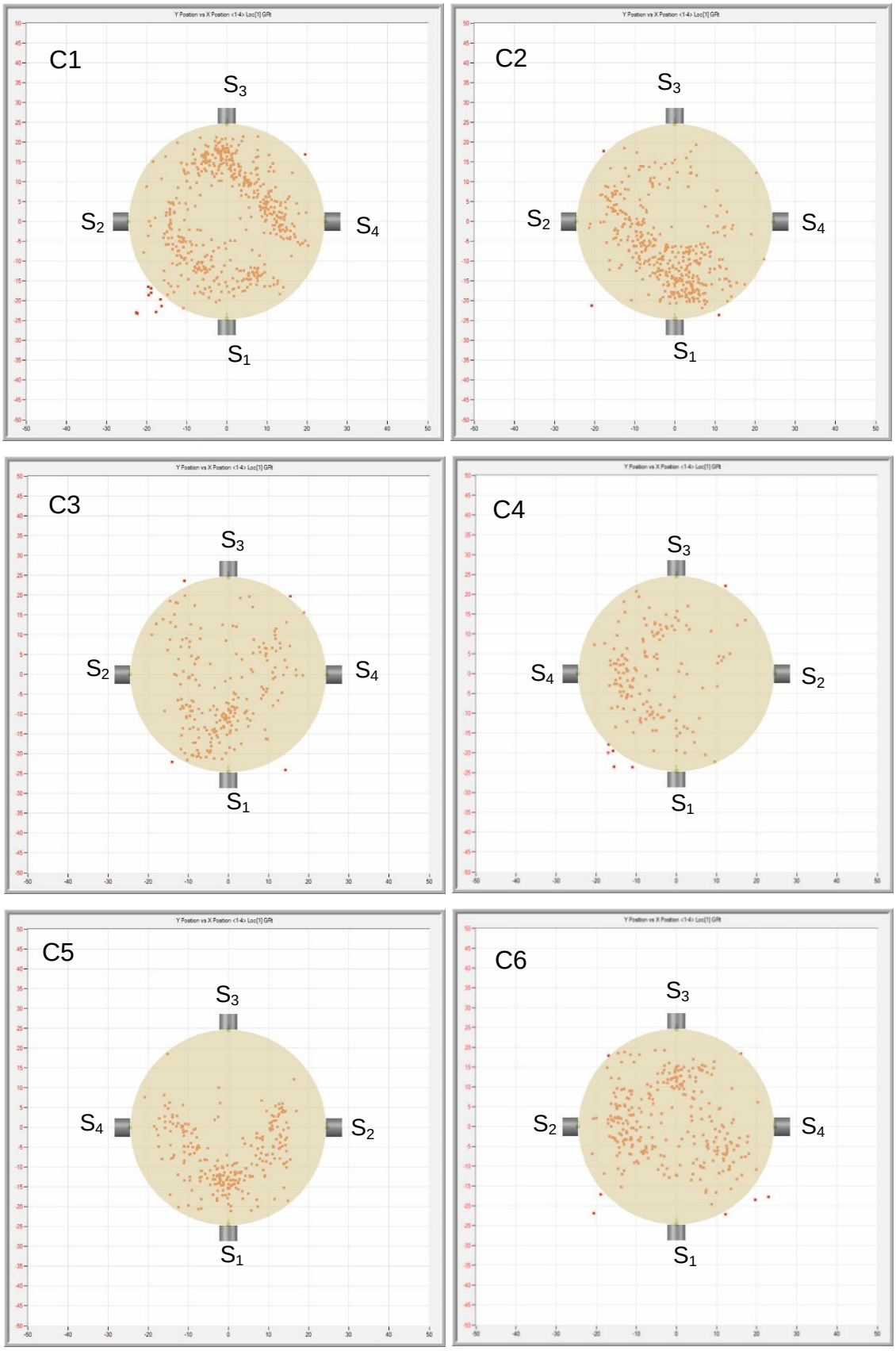

Figure 6.36: 2D location of events of specimens C1 – C6. The positions of the 4 sensors that are circumferentially placed on the specimens are also shown.

6.3 Cubic specimens

The cubic specimens were subjected to uniaxial loading at a constant rate of deformation as opposed to the other specimens where different types of loading were applied (step, linear, saw-tooth). It should be noted that no conductivity measurements could be performed during these tests but only the AE activity was measured in conjunction with the stress-strain, in order to investigate the mechanical behaviour of the porous sandstone material.

A representative stress-strain curve of a cubic sandstone specimen (specimen Cu3) is shown in Fig. 6.37. Higher values of strain are recorded with the LVDT which measures the overall deformation of the specimen, while the strain gauge shows only the deformation of the material in the region where it is positioned.

The time evolution of the AE parameters during the uniaxial loading of the water-saturated sandstone specimen Cu3 is depicted in Figs. 6.38 and 6.39. The corresponding 3D location of events is shown in Fig. 6.40. The velocity of acoustic waves for the cubic specimens that was used for the calculations was estimated to be (3300±15) m/s.

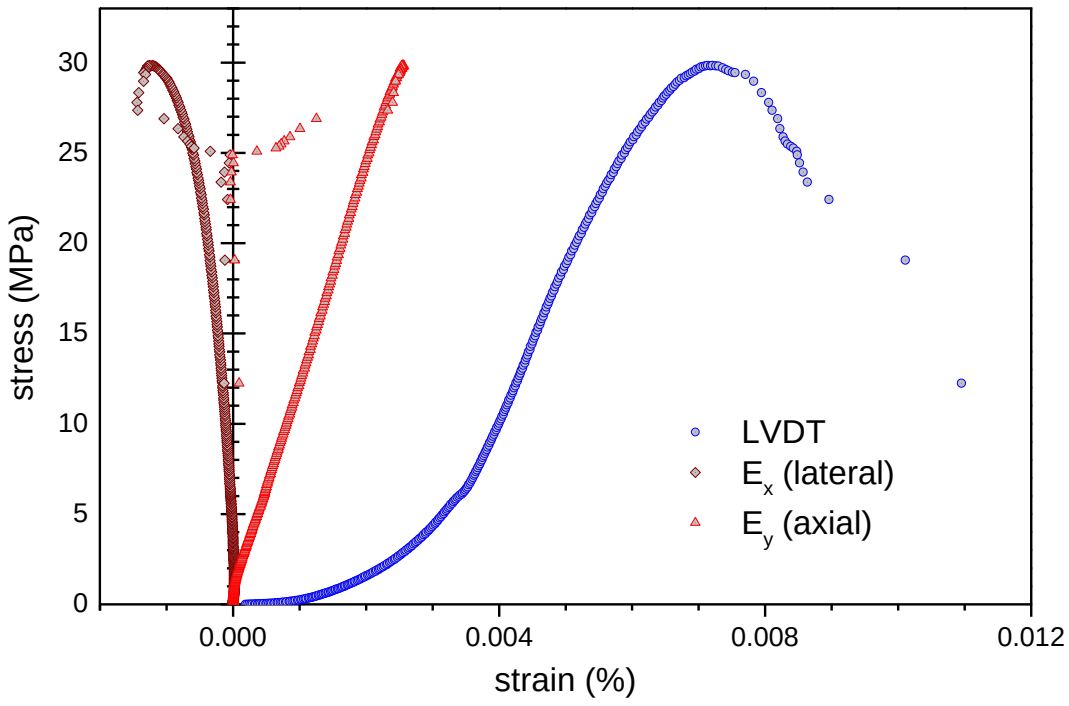

Figure 6.37: Stress-strain curve for the cubic specimen Cu3. The strain was measured in two ways, by using a LVDT and by a strain gauge attached to the surface of the specimen, at half its height.

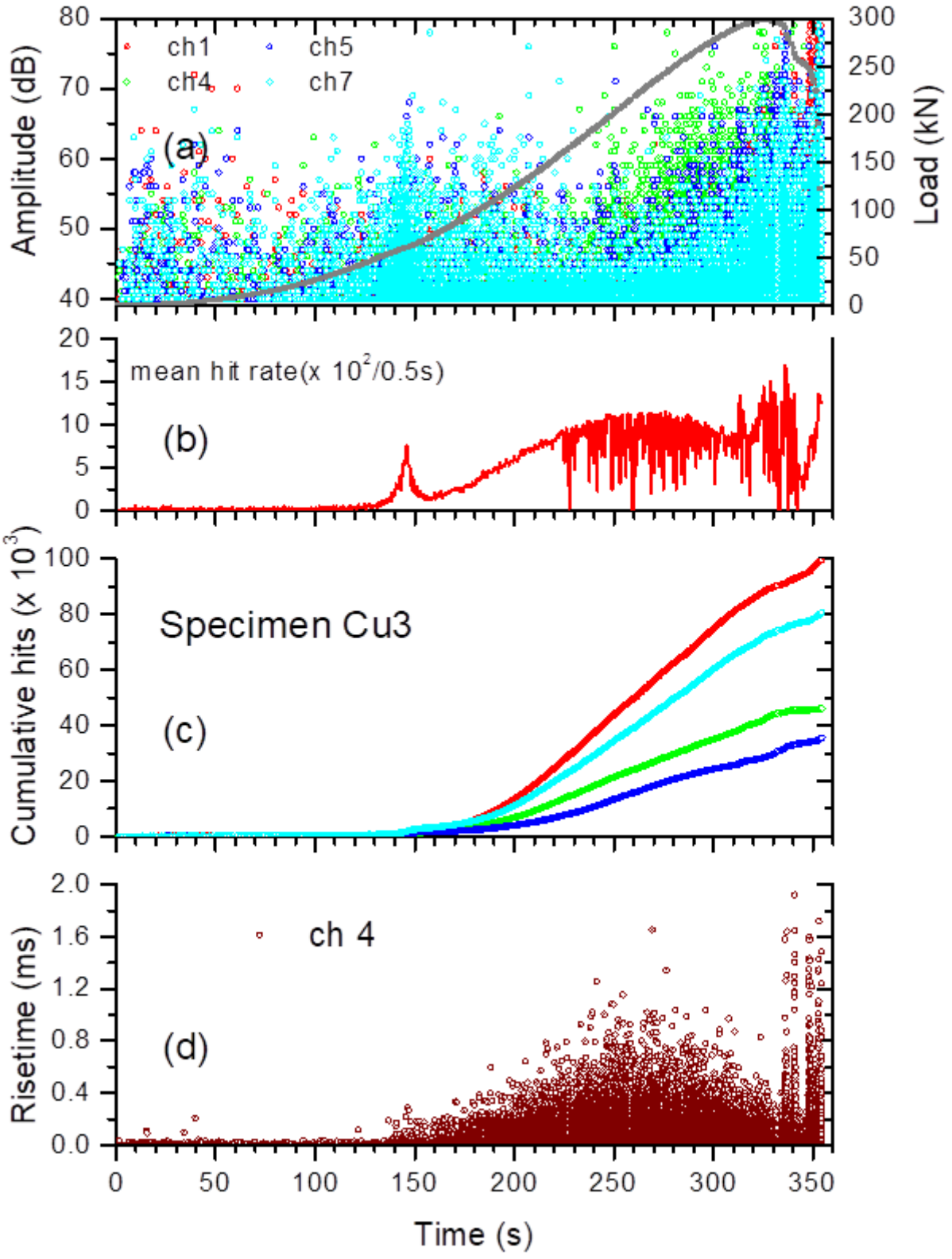

Figure 6.38: Time evolution of AE parameters during the uniaxial compression of the sandstone sample Cu3. (a) The amplitudes of selected channels (1, 4, 5 and 7) and the applied load, (b) the mean hit rate of all channels, (c) the cumulative hits of channels 1, 4, 5 and 7 and (d) the risetime of channel 4. The final rupture of the specimen occurs at t=350 s, as indicated from the corresponding drop of the load.

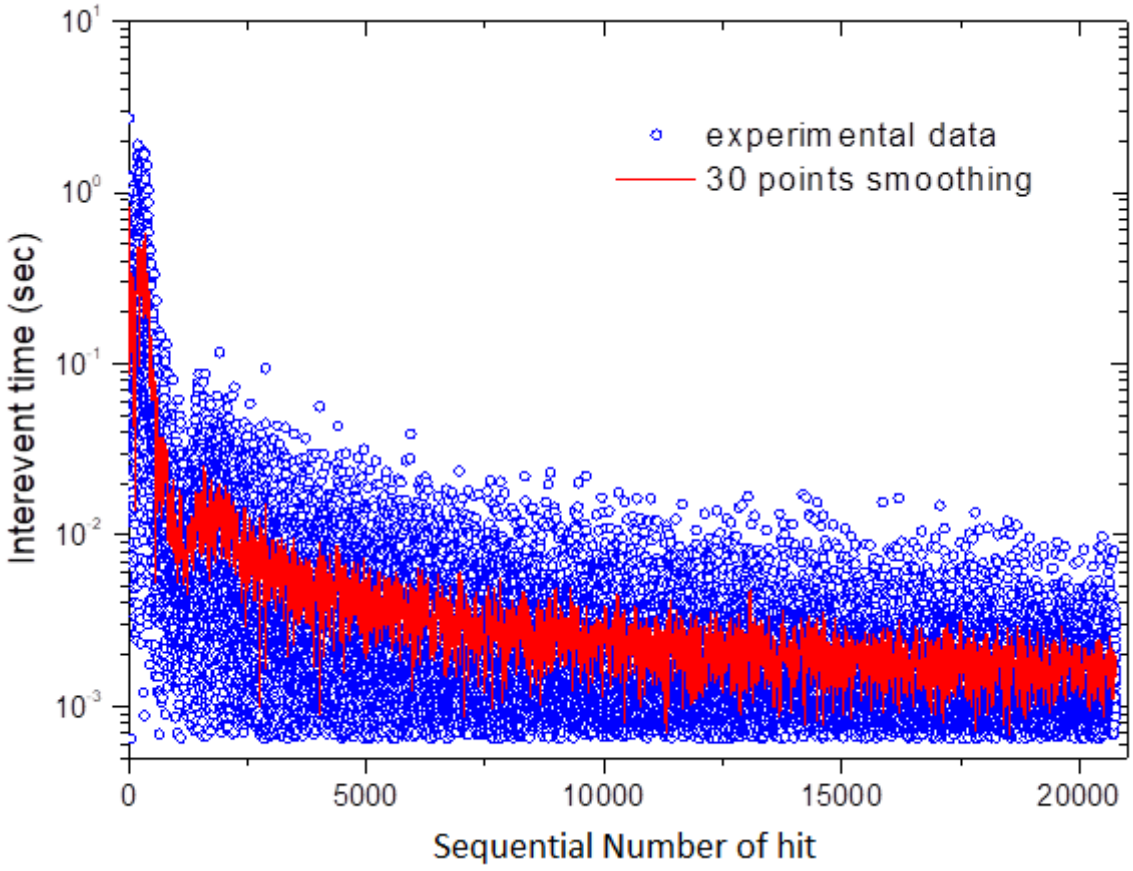

Figure 6.39: Inter-event times of recorded hits in channel 4 of the sandstone sample Cu3.

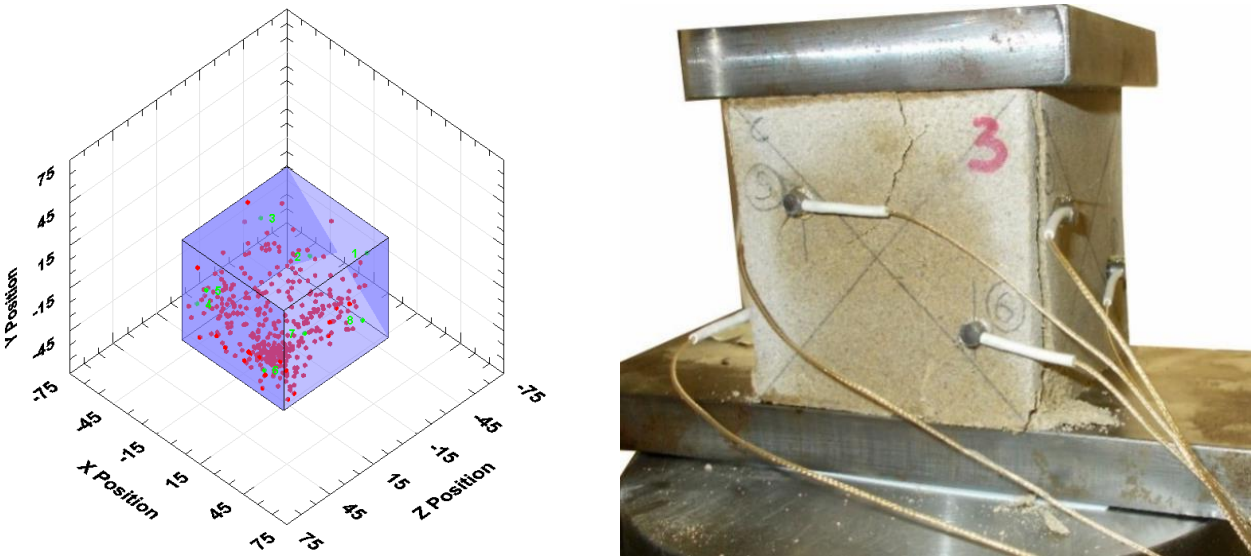

Figure 6.40: 3D location of events (left) and a photograph of the specimen Cu3 (right) after the compression loading test.

6.4 Improved b-values

Analysis of improved b-values was performed for all specimens and the results are illustrated in Figs. 6.41 – 6.44. In all cases, we observe that as the specimen approaches the failure, Ib-value decreases, taking values below unity.

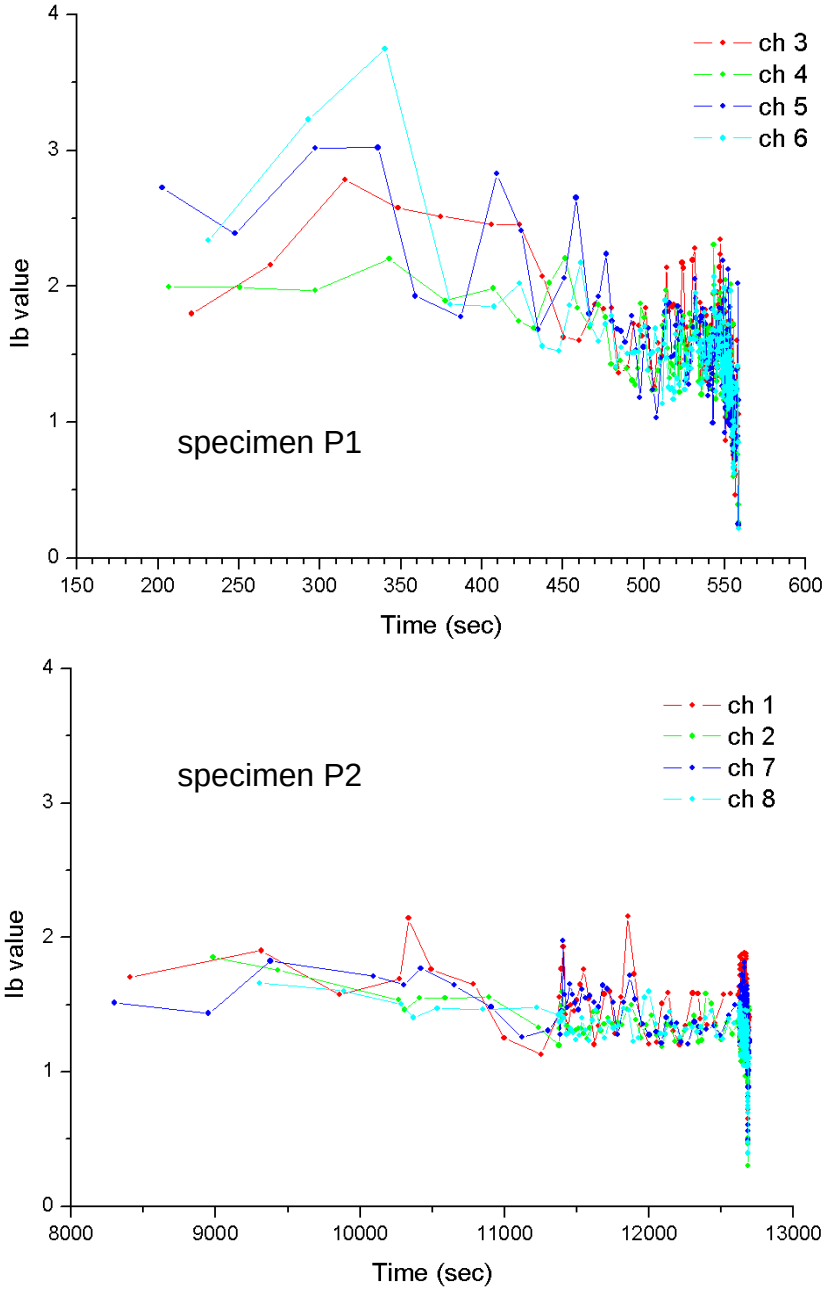

Figure 6.41: Improved b-values for specimens P1 and P2.

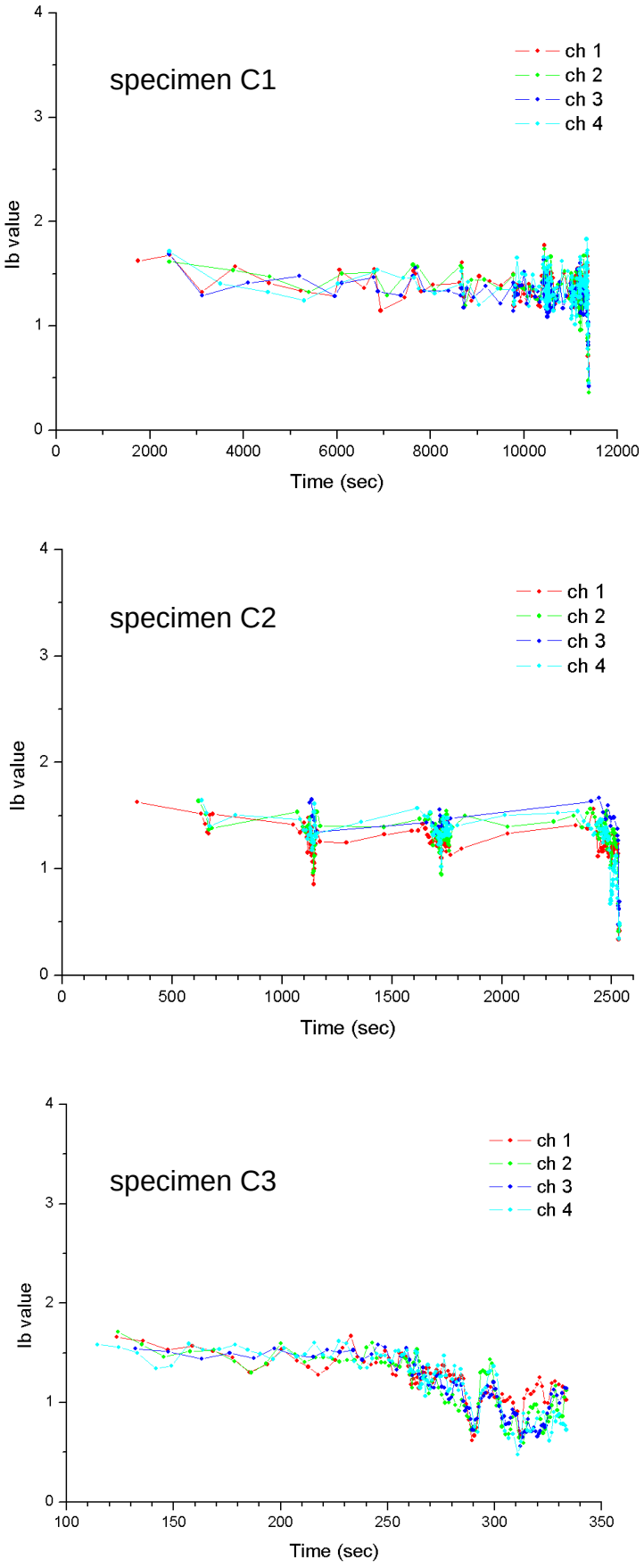

Figure 6.42: Improved b-value calculation for specimens C1, C2 and C3.

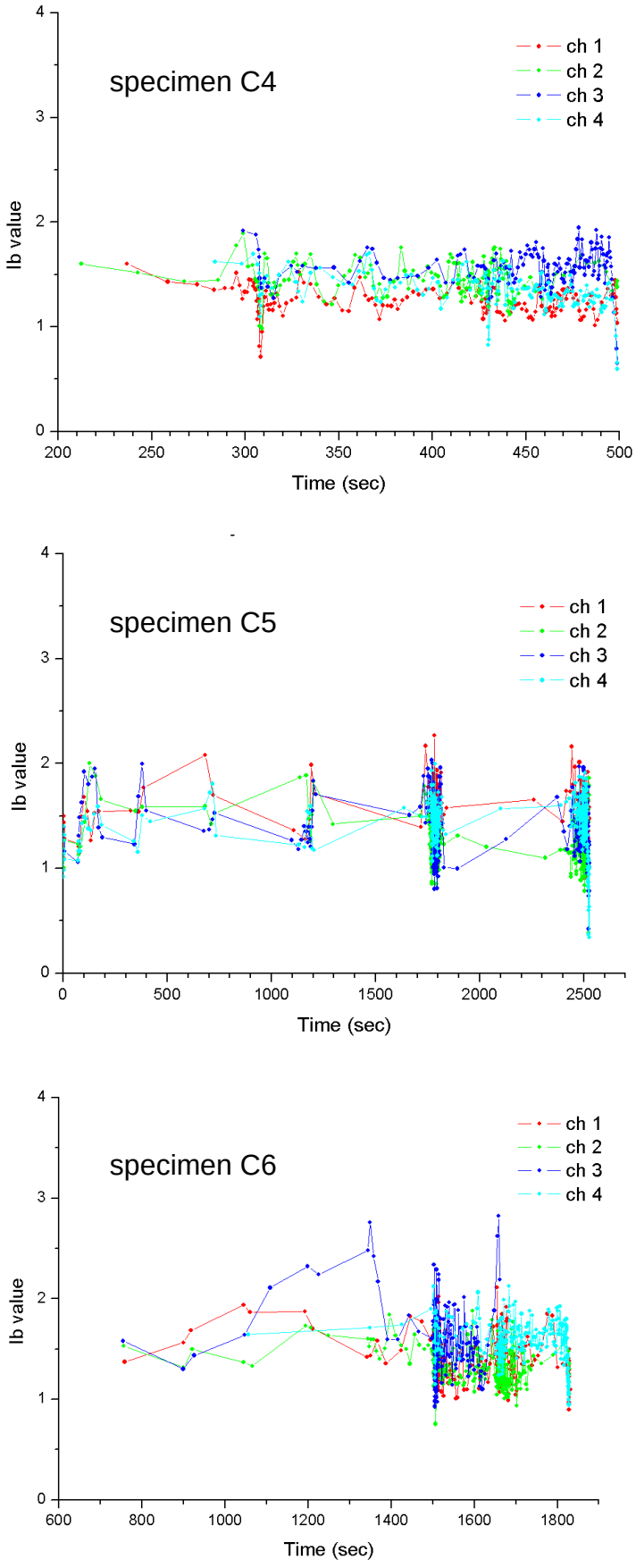

Figure 6.43: Improved b-values for specimens C4, C5 and C6.

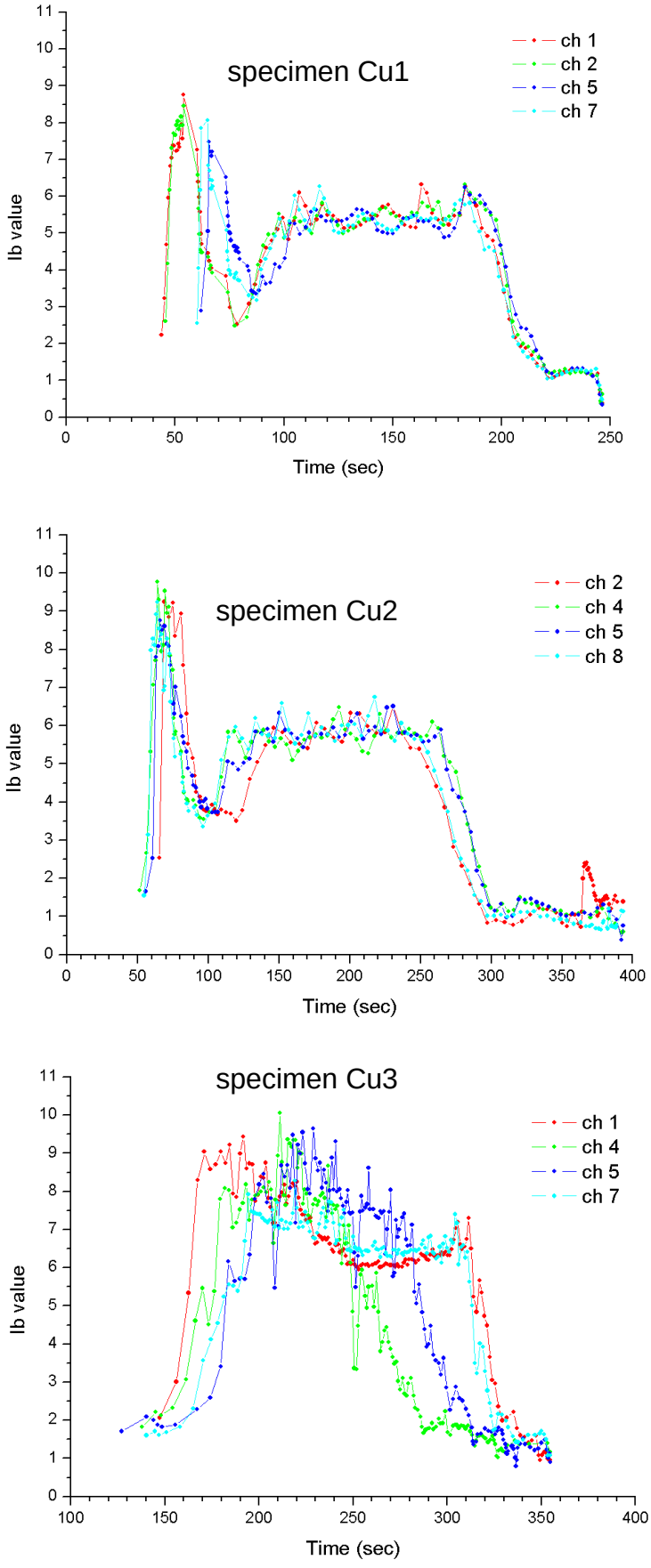

Figure 6.44: Improved b-values for specimens Cu1, Cu2 and Cu3.

Chapter 7: Conclusions and Future Research

7.1 Conclusions

In the present thesis, AE activity was monitored simultaneously with ac-conductivity measurements at selected frequencies during different types of uniaxial loading of sandstone specimens of high porosity (apparent porosity, ~7%). The influence of water content to the measured AE parameters and ac-conductivity was investigated by performing experiments in partially or fully water-saturated sandstone specimens.

Two different geometries of specimens were used, that is, prismatic and cylindrical specimens, in order to measure the ac-conductivity in two different directions. In the prismatic specimens, conductivity was measured in the direction that was perpendicular to the applied uniaxial stress, while in the cylindrical specimens, the measured conductivity was in the same direction as the applied stress.

In order to study the existence of memory phenomena (Kaizer and Felicity effects), sandstone specimens were subjected to cyclic saw-tooth loading and the Felicity ratio (FR) was calculated as a function of the applied load.

From the in-depth analysis of the experimental results, the main conclusions can be summarized as follows:

- ✓ Changes in the measured ac-conductivity are observed from the initial stage of loading up to the ultimate failure of each sandstone specimen. In specimens of low water content, that is, specimens exposed to ambient moisture, conductivity decreases with the applied load, while in water-saturated sandstone specimens, conductivity increases for all types of loading (stepped, linear and saw-tooth). For example, the aforementioned difference between the conductivities of specimens C1 and C4 (i.e. the negative or positive variation with increasing pressure) is obviously related to the different water content of the two specimens. This variation is either positive or negative, depending on the water content of the sandstone specimen.

  The water inside the pore volume may exist in bound and/or free state, depending on the amount of it. The application of the external pressure to the sandstone specimen leads to the generation, propagation and coalescence of micro-cracks. In this case, the excess of water is passed through the newly created network of cracks, forming

new conduction paths which enhance the overall electrical conductivity of the specimen. A critical water content should exist that causes the inversion of the ac-conductivity values, i.e. percolation effects should be taken into consideration.

- ✓ Changes in the measured ac-conductivity are observed in both directions, i.e. vertically and in parallel to the applied uniaxial loading in prismatic (P1, P2) and cylindrical (C1, C2) specimens exposed to ambient moisture. Notably, changes in ac-conductivity are greater in the parallel than in the vertical direction relative to the applied stress, suggesting the formation of specific shear planes inside the specimen prior to its failure. This is in agreement with the observed macroscopic failure of the corresponding specimens. Similar results are also observed in stepped and saw-tooth type of uniaxial loading. However, the generation and propagation of cracks inside the material during the uniaxial loading is not the only responsible mechanism for the conductivity variation, but the role of water in free or bound state should also be taken into consideration, as it was mentioned previously.

- ✓ Strong correlations of the measured ac-conductivity with the AE parameters, the applied load and the induced deformation are observed in all cases of different type of loading. The observed conductivity changes are imprinted in the same way across all measured frequencies (10 kHz, 200 kHz). In the cases of continuous recording of ac-conductivity, such as in the linear and saw-tooth loading experiments, the measured conductivity follows precisely the changes of the applied load which is also reflected to the recorded AE activity. Especially, in the case of the saw-tooth loading in the specimens C3 and C6 with different water content, abrupt changes in the measured conductivity occur around the peak stress, while conductivity relaxes during the release of the stress in each loading cycle. The latter suggests that conductivity is very sensitive to the application of variable mechanical load and could be used autonomously or in combination with AE activity to monitor the damage in materials subjected to mechanical stress.

- ✓ A lower AE activity is recorded in water-saturated sandstone specimens. This low AE activity could be attributed to the influence of the water which acts as a lubricant in the newly formed cracks during the applied load and reduces the friction between the fault planes.

- ✓ The inter-event time is an AE parameter that exhibit specific characteristics, depending on the type of the applied load. In this sense, it could be used as an indicator of the upcoming failure of brittle materials subjected to mechanical stress. In this case, a value of inter-event time could be determined as a safety threshold to denote the entrance of the specimen to the failure stage, in order to avoid any future damage of the specimen.

7.2 Future Research

From the experiments that were carried out in the present thesis, it is evident that a strong correlation of the ac-conductivity with the AE activity is observed during different types (linear, stepped, saw-tooth) of uniaxial compression in the porous sandstone specimens. These observations are of great importance in investigating precursory phenomena in the meso- and macro-scale, such as the mechanical failure of materials and the occurrence of pre-seismic electric signals.

Our findings suggest that variations in ac-conductivity are observed in parallel and perpendicular directions of the applied load, exhibiting sensitivity to the different types of loading. Additional changes are also observed due to the different water content of the porous sandstone specimens.

A few important issues that should be further explored are the following:

- ✓ The electrical impedance spectra that are collected during stepped-like loading experiments, will give valuable information about the conductivity mechanisms and the contributions of the grain boundaries and grains interior of the sandstone to the overall measured conductivity.

- ✓ More experimental work should be carried out to investigate the relaxation of the measured conductivity that has been observed after the release of the applied load in saw-tooth loading tests.

- ✓ Regarding the AE parameter of inter-event time, except of the qualitative characteristics that are indicative of the upcoming failure, a non-extensive statistical analysis in the frame of Tsallis entropy Tsallis, 2009; Vallianatos *et al*., 2012 may reveal additional information to distinguish the failure mechanisms.

- ✓ Experiments should be also carried out in sandstone or other porous rock specimens with different water content, in order to find the critical value that causes the inversion of the ac-conductivity from positive to negative changes. However, we have to emphasize that is not easy to achieve experimentally stable water content in porous specimens which affects considerably the measured electrical conductivity.

- ✓ The present experimental work could be further extended to other porous rock materials saturated (partially or fully) with different fluids such as brine or oil.

References - Bibliography

Aggelis D. G. (2011). Classification of cracking mode in concrete by acoustic emission parameters. Mechanics Research Communications 38, 153-157.

Aggelis D. G., Soulioti D. V., Sapouridis N., Barkoula N. M., Paipetis A. S. & Matikas, T. E. (2011). Acoustic emission characterization of the fracture process in fibre reinforced concrete. Construction and Building Materials 25(11), 4126–4131.

Aggelis D. G., Mpalaskas A. C., Matikas, T. E. (2013). Investigation of different fracture modes in cement-based materials by acoustic emission. Cement and Concrete Research 48, 1-8.

Agioutantis Z., Kaklis K., Mavrigiannakis S., Verigakis M., Vallianatos F., & Saltas V. (2016). Potential of acoustic emissions from three point bending tests as rock failure precursors. International Journal of Mining Science and Technology 26,155–160.

Asaoka A., Adachi T. and Oka F. (1997). Deformation and Progressive Failure in Geomechanics, Elsevier Science, pages 515-518.

Athy L. F. (1930). Density, Porosity, and Compaction of Sedimentary Rocks. AAPG Bulletin, 14(1), 194–200.

Boggs S. (2009). Petrology of Sedimentary Rocks 2nd Edition. Cambridge University Press, pages 21-23

Boyce G.M., McCabe G.M. & Koerner R.M. (1981). Acoustic emission signatures of various rock types in confined compression, Proc Acoustic Emissions in Geotechnical Engineering Practice, ASTM Stp 750, pp 142-154.

Byerlee J. D., & Lockner D.A. (1977). Acoustic emission during fluid injection into rock. In: Hardy HR, Leiton FW (eds) Proceedings of 1st conference on acoustic emission/microseismic activity in geological structures and materials, Trans. Tech. Publications, pp 87–98.

Colombo S., Forde M. C., Main I. G., Halliday J., & Shigeishi M. (2005). AE energy analysis on concrete bridge beams. Materials and Structures, 38(283), 851–856.

Cook N.G.W. (1965). The failure of rock. International Journal of Rock Mechanics and Mining Sciences & Geomechanics Abstracts, 2(4), 389–403.

Freund F. T., Takeuchi A., Lau B. W. S., Post R., Keefner J., Mellon J., & Al-Manaseer A. (2004). Stress-induced changes in the electrical conductivity of igneous rocks and the generation of ground currents. TAO 15, 437-467.

Glover Paul W.J. (2000). Petrophysics, Department of Geology and Petroleum Geology University of Aberdeen, UK, pages 10-20.

Goodman R. E. (1963). Subaudible noise during compression of rocks. Bulletin of the Geological Society of America, 74(4), 487–490.

Grosse C.U. & Ohtsu M. (2008). "Acoustic Emission Testing. Basic for Research-Applications in Civil Engineering," Springer-Verlag, Berlin Heidelberg.

Gutenberg B., & Richter C.F. (1956). Magnitude and energy of earthquakes, Annals of Geophysics, 9,1.

Hardy H.R. & Shen H.W. (1992). Recent Kaiser Effect studies in rock, Progress in Acoustic Emission VI, the Japanese Society for NDI, 149 - 157.

Hardy H.R. (2003). Acoustic emission / Microseismic activity, Volume 1: Principles, Techniques and geotechnical applications, A.A. Balkema.

Havskov J., & Ottemoller L. (2010). Routine Data Processing in Earthquake Seismology, Springer, pages 318-319.

Hisham A. & Elfergani (2013). Acoustic Emission Analysis of Prestressed Concrete Structures, PhD, Cardiff University, UK.

Hofmann J. R., & Hofmann P. A. (1992). Darcy's Law and Structural Explanation in Hydrology. PSA: Proceedings of the Biennial Meeting of the Philosophy of Science Association, pp. 23–35.

Hudson, J.A., Brown, E.T., Fairhurst C., & Hoek E. (1993). Comprehensive Rock Engineering, Pergamon Press Ltd, pages 45 - 51.

Jaeger J., Cook, N. G., & Zimmerman, R. (2007). Fundamentals of Rock Mechanics, 4th Edition. Journal of Chemical Information and Modeling (Vol. 53).

Kusunose K., Nishizawa O., Ito H., Ishida T., & Hasegawa I. (1982a). Source mechanism of acoustic emission in rocks under uniaxial compression, Zisin. J Seism Soc Japan 34:241–250 (in Japanese).

Kusunose K., Nishizawa O., & Onai K. (1982b). AE gap in a rock under uniaxial compression, Zisin. J Seism Soc Japan 35:91–102 (in Japanese).

Lavrov A., Vervoort A., Wevers M., & Napier J. A. L. (2002). Experimental and numerical study of the Kaiser effect in cyclic Brazilian tests with disk rotation. International Journal of Rock Mechanics and Mining Sciences, 39(3), 287–302.

Lavrov A. (2003). The Kaiser effect in rocks: principles and stress estimation techniques. International Journal of Rock Mechanics & Mining Sciences 40, 151–171.

Lavrov A. (2005). Fracture-induced physical phenomena and memory effects in rocks: A review. Strain 41, 135–149.

Lei X. (2006). Typical phases of pre-failure damage in granitic rocks under differential compression. In: Cello G, Maramud BD (eds), Fractal analysis for natural hazards, vol 261. Geological Society, Special Publication, pp 11–29.

Lei X., Tamagawa T., Tezuka K., & Takahashi M. (2011). Role of drainage conditions in deformation and fracture of porous rocks under triaxial compression in the laboratory. Geophysical Research Letters, 38(24).

Mistras, 2013, NOESIS Manual.

Mogi K. (1962). Study of elastic shocks caused by the fracture of heterogeneous materials and its relation to earthquake phenomena. Bull Earthq Res Inst 40:125–173.

Obert L. & Duvall W.I. (1942). Use of Sub audible Noises for the Prediction of Rock Bursts, Part II, RI 3654, USBM.

Physical Acoustics Corporation, User's Manual, April 2007.

Qi T. and Feng G. (2017). Resistivity and AE response characteristics in the failure process of CGB under uniaxial loading. Advances in materials Science and Engineering, DOI: 10.1155/2017/7857590.

Saltas V., Fitilis I., Vallianatos F. (2014). A combined complex electrical impedance and acoustic emission study in limestone samples under uniaxial loading. Tectonophysics 637, 198-206.

Scholz C.H. (1968a). Experimental study of the fracturing process in brittle rock. Journal of Geophysical Research 73:1447–1454.

Shiotani T., Fujii K., Aoki T. & Amou K. (1994). Evaluation of progressive failure using AE sources and improved b-value on slope model test, Progress in AE VII, pp 529-534.

Soulioti D., Barkoula N. M., Paipetis A., Matikas T. E., Shiotani T., & Aggelis D. G. (2009). Acoustic emission behavior of steel fibre reinforced concrete under bending. Construction and Building Materials, 23(12), 3532–3536.

Stavrakas I., Moutzouris K., Ninos K., Mitritsakis N., Agioutantis Z., & Triantis D. (2012). Using ac-conductivity measurements to study the influence of mechanical stress on the strength of geomaterials. Open Journal of Applied Sciences 2, 61-65.

Stavrakas I., Triantis D., Agioutantis Z., Maurigiannakis S., Saltas V., Vallianatos F. & Clarke M. (2004). Pressure stimulated currents in rocks and their correlation with mechanical properties. Natural Hazards and Earth System Science, 4(4), pp.563–567.

Stavrakas I. (2017). Acoustic emissions and pressure stimulated currents experimental techniques used to verify Kaiser effect during compression tests of Dionysos marble. Frattura ed Integrità Strutturale 40, 32-44.

Stergiopoulos C., Stavrakas I., Hloupis G., Kyriazopoulos A., Triantis D., Anastasiadis C. & Stonham J. (2012). Monitoring acoustic emissions and electrical signals during three-point bending tests performed on cement mortar specimens. In: Proceedings of 8th international conference fracture mechanics of concrete and concrete structures, FraMCoS-8, abs no. 591, Toledo, Spain, 11–14 March.

Tawhidul Islam Khan Md., Nagafuchi Sunichi, & Mehedi Hasan (2014). Structural Damage Localization by Linear Technique of Acoustic Emission, Scientific Research.

Tsallis C. (2009). Introduction to non-extensive statistical mechanics: Approaching a complex world. Berlin: Springer.

Vallianatos F., Benson P., Meredith P., & Sammonds P. (2012). Experimental evidence of a non-extensive statistical physics behaviour of fracture in triaxially deformed Etna basalt using acoustic emissions. EPL 97, 58002-6.